

Universität
Rostock



Traditio et Innovatio

A Fast Method for Mobile In-Situ Monitoring of Optical Properties in Aquatic Environments

Robert Schima

Rostock

November 14, 2018

A DISSERTATION

SUBMITTED TO THE FACULTY OF MECHANICAL ENGINEERING AND
MARINE TECHNOLOGY OF ROSTOCK UNIVERSITY

IN PARTIAL FULFILLMENT OF THE REQUIREMENTS

FOR THE DEGREE OF

DOCTOR OF ENGINEERING

Doktor-Ingenieur (Dr.-Ing.)

submitted by:

Robert Schima, born on 25. February 1988 in Dessau



Dieses Werk ist lizenziert unter einer
Creative Commons Namensnennung - Weitergabe unter gleichen Bedingungen 4.0
International Lizenz.

Date of submission: November 14, 2018

Date of defense: May 15, 2019

Reviewers: Prof. Dr.-Ing. habil. Mathias Paschen,
University of Rostock

Prof. Dr. Peter Dietrich,
University of Tübingen

Research was conducted at the University of Rostock as well as at
the Helmholtz Centre for Environmental Research GmbH - UFZ,
Leipzig.

Acknowledgments

I would like to express my sincere gratitude to my supervisor Prof. Dr.-Ing. habil. Mathias Paschen from the University of Rostock for the continuous support, his patience and the motivation since my master studies. His guidance helped me to carry out my research at the Chair of Ocean Engineering as well as to write this thesis.

My sincere thanks go to Prof. Dr. Peter Dietrich for his support, his sympathetic advice and critical remarks where necessary during my time as a researcher at the Department of Monitoring and Exploration Technologies (MET) of the Helmholtz Centre for Environmental Research (UFZ) in Leipzig and beyond.

I would like to thank my mentor Dr.-Ing. Jan Bumberger (UFZ) for getting me enthusiastic about science and for paving the way for my doctorate. I am grateful to Dr. agr. Steffen Zacharias (UFZ) for the inspiring conversations about science and art as well as the opportunity to gain experience in environmental research on a European level.

In particular, I would like to thank Prof. Dr.-Ing. Ralf Bill (University of Rostock) for having always supported me since my studies and for advising me as a mentor. For having the chance to stay as a visiting scientist at the University of California, Berkeley, I would particularly like to thank Prof. Dr. Yoram Rubin for the invitation, the intensive discussions and the fruitful cooperation.

I thank Dr. Ralf Prien (Leibniz Institute for Baltic Sea Research) for the valuable discussions about optical in-situ measurement technology and how pleasant it is when a device works as it should. My special thanks go to Thomas Mohr (Landesforschungsanstalt für Landwirtschaft und Fischerei) for his valuable support and raising awareness of the practical challenges in ocean engineering. I would like to thank Dr. Daniel Stepputtis and Dr. Andreas Hermann (Thünen Institute of Baltic Sea Fisheries) for the opportunity to take part in a sea research cruise (WH415), for the long and fruitful discussions and the chance to feel on my own what research at sea could mean.

Many thanks go to the team of the Chair of Ocean Engineering (University of Rostock) for their excellent cooperation and support during my work, especially to Christoph Otto, Dr.-Ing. Peter Menzel and Uwe Lichtenstein. I would also like to thank the team of the UFZ MET Department for their assistance. My special thanks go to Tobias Goblirsch, a better friend, colleague and motivator cannot be found. I would like to thank Tanja, Nils, Fiete and everyone else for the proofreading, the many good comments and discussions and for the nice time during my doctorate.

Not least, I thank my family for their unwavering support. My fiancée Alexandra deserves my special thanks for her support and patience during my doctorate and in everyday life.

Zusammenfassung

Der Schutz und die nachhaltige Nutzung mariner Ressourcen erfordern eine bessere Kenntnis über die Prozesse und Wechselwirkungen mariner Ökosysteme. Derzeitige Methoden, die in der angewandten Forschung zum Einsatz kommen, reichen nicht aus, um die Heterogenität und Dynamik mariner Ökosysteme in ihrer Komplexität angemessen zu erfassen. Eine große ingenieurwissenschaftliche Herausforderung besteht darin, geeignete Methoden und Messverfahren für ein ganzheitliches In-situ-Monitoring mit entsprechend erhöhter räumlicher und zeitlicher Auflösung bereitzustellen.

Innerhalb dieser Dissertation werden die grundlegenden Herausforderung bei der messtechnischen Erfassung komplexer, ökosystemarer Prozesse aufgezeigt. Auf Grundlage dieser Betrachtung wird ein Theorem zur ganzheitlichen Erfassung ökosystemarer Zustandsgrößen abgeleitet, welches mit *Object Specific Exposure* (OSE) bezeichnet wird.

Darauf aufbauend beschreibt die vorliegende Dissertation einen technologischen Ansatz zur Überwachung von Prozessen in komplexen Ökosystemen unter Verwendung eines optischen Sensorsystems für mobile Monitoringanwendungen. Dazu wurde ein Messsystem entwickelt, welches ausgehend vom Messprinzip einer optischen Transmissionsbestimmung im Durchlichtverfahren eine schnelle In-situ-Bestimmung von Wasserqualitätsparametern zulässt. Im vorliegenden Fall handelt es sich dabei um eine Messung der Transmission im UV-Bereich der elektromagnetischen Strahlung zur Abschätzung des Gehalts an *Chromophoric dissolved organic carbon* (CDOM) und einer Transmissionsmessung im IR-Bereich zur Trübungskorrektur.

Im Rahmen dieser Arbeit wurde ein grundlegendes Sensorkonzept formuliert, welches aufgrund der modularen und service-orientierten Architektur auf andere Anwendungsfälle übertragbar ist. Durch die enge Verzahnung der Sensorentwicklung mit der nachfolgenden Datenprozessierung wird zudem eine Inwertsetzung in naher Echtzeit ermöglicht.

Der Funktionsnachweis des Sensorsystems wurde anhand von Laboruntersuchungen erbracht. Anhand zweier mobiler Monitoringanwendungen entlang der Warnow bei Rostock wurde zudem gezeigt, wie der vorgestellte technologische Ansatz dazu beiträgt, den Informationsgehalt von im Feld erhobenen Sensordaten zu erhöhen und gleichzeitig den Aufwand für den Anwender auf der Grundlage des OSE-Theorems zu reduzieren.

Abstract

The protection and sustainable use of marine resources require a better understanding of oceans and marine ecosystems. Current methods used in applied research and scientific surveys are not sufficient to address the heterogeneity and dynamics of marine ecosystems appropriately. A major challenge is to provide methods for a holistic in-situ monitoring and long-term observation technologies with increased spatio-temporal resolution.

This dissertation investigates the dynamic monitoring of processes in complex ecosystems by using an optical sensor based measurement system. To address this problem, a fast method that includes the usage of data derived by mobile sensors is proposed. A sensor concept is formulated and a prototypical demonstrator is developed for the fast in-situ determination of optical properties of aquatic environments. The basic feasibility is investigated with a laboratory and field study. The field study is based on two measurement surveys using a canoe and a sailboat on the Warnow along the urban area of Rostock and proves the basic suitability of the system.

In addition to the development of an adaptive optical sensor system, this thesis introduces a holistic sampling theorem, the object specific exposure (OSE). On the basis of the OSE sampling theorem, a methodological approach for holistic environmental monitoring is postulated and the significance of contextualization for an improved understanding of spatio-temporal monitoring data is explained.

In summary, this dissertation presents a fundamental sensor development according to the OSE sampling theorem from an ocean engineering perspective. It provides a fast method based on a service-oriented optical sensor system that allows reliable statements regarding the state of aquatic (eco-) systems with feasible sensor effort during the field measurement. The technological approach presented in this thesis helps to increase the informative value of sensor data while reducing the effort for the user based on the underlying OSE sampling theorem.

Contents

Acknowledgments	iii
Zusammenfassung	iv
Abstract	v
List of Tables	x
List of Figures	xi
Acronyms	xiv
List of Symbols	xvi
I. Introduction	1
1. Motivation	2
1.1. Problem Description	3
1.2. Situation Description	3
1.3. Goal	4
1.4. Requirements	5
1.5. Expected Results	5
1.6. Target Parameters - Turbidity and the Amount of Dissolved Organic Matter	6
2. Thesis Structure	7
II. Sensing as a Service – Towards Holistic Paradigms in Environmental In-situ Monitoring	8
3. Environmental Monitoring and Observation - A Matter of Space and Time	9
3.1. Temporal Aspects of Environmental Data Acquisition	9
3.2. Spatial Aspects of Environmental Data Acquisition	10
3.3. Spatio-temporal Aspects of Environmental Data Acquisition	11

4. Towards a Comprehensive Sampling Theorem for Monitoring Applications	12
4.1. Object Specific Exposure (OSE)	12
4.2. Predictive Object Specific Exposure (POSE)	13
III. Water Quality Assessment - Potentials and Challenges of Optical In-situ Measurements	15
5. The Assessment of Water Quality	16
5.1. Potential of Optical Measurement Principles	16
5.2. Optical Characteristics of Water	17
5.3. Inherent Optical Properties	18
5.4. Beer-Lambert Law	21
5.5. Properties of Natural and Optically Complex Waters	23
5.5.1. Transmittance Spectrum of a Natural Water Sample	24
5.5.2. Extinction Spectrum of a Natural Water Sample	25
6. In-situ Determination of Optical Properties	26
6.1. In-situ Measurement of Optical Properties	27
6.2. Limitations of Optical In-situ Measurement	28
6.3. Optical In-situ Sensors for Water Quality Assessment	29
6.4. Demands for Aquatic Monitoring in Research	29
IV. System Development	30
7. Preliminary Consideration	31
7.1. Application Requirements	31
7.2. Sensing as a Service – Towards a Service-oriented System Architecture	32
7.2.1. Communication Protocols and Interfaces	33
7.2.2. Electronic Parts and Printed Circuit Boards	33
7.2.3. 3D Printed Parts for Applied Research	33
7.2.4. Pressure Tolerant Hardware Design for Underwater Systems	34
8. Development of an Adaptive Sensor Probe	35
8.1. A Sensor Probe Made of Sensors	35
8.2. Electronic Sensor Modules	36
8.2.1. Communication Unit	36
8.2.2. Emitter Unit	37
8.2.3. Detector Unit	38
8.2.4. Pressure and Temperature Unit	38

8.3. Enclosure Components and Peripherals	39
8.3.1. 3D-printed Enclosure Components	39
8.3.2. Cast	40
8.3.3. Cable and Connectors	40
8.4. Full Assembly of Optical Sensor Probe	40
9. Development of a Service-Oriented Sensor System	42
9.1. System Architecture	42
9.1.1. Top Side Unit	43
9.2. Software Development	44
9.2.1. The Program Code	44
9.2.2. Data Handling	46
V. System Assessment	48
10. Materials and Methods	49
10.1. Measuring Devices	49
10.2. Experimental Test Setups	50
11. Optoelectronic Characterization of Sensor Components	52
11.1. Electronic Characterization of the Emitter Unit	52
11.2. Spectral Characterization of the Emitter Unit	54
11.3. Current-PWM Modulation of the Sensor Probe	58
11.4. Repeatability Assessment	61
12. System Characterization Regarding the Anticipated Operating Conditions	62
12.1. Pressure Resistance	62
12.2. Temperature Compensation	63
13. Measurement Quality Assessment	65
13.1. Assessment of CDOM Approximation	65
13.2. Assessment of Turbidity Approximation	66
VI. Case Study	67
14. Mobile Turbidity and DOM Monitoring	68
14.1. Site description	68
14.2. Challenge	69
14.3. Materials and Methods	69
14.4. Results	71
14.4.1. In-situ Monitoring Using a Canoe	71

14.4.2. In-situ Monitoring Using a Sailboat	74
VII. Discussion	80
15. Discussion	81
15.1. Sensing as a Service – The OSE Sampling Theorem	81
15.2. Sensor and System Development for an Advanced Monitoring	81
15.3. Case Study as Proof of Concept Analysis	88
VIII. Conclusion and Outlook	90
16. Conclusion	91
17. Outlook	92
17.1. Predictive Monitoring - Towards Data-Driven Research in Environmental Sciences	92
17.2. A Fast Data Evaluation for Decision Making	93
17.3. Future Work	94
Bibliography	96
IX. Appendix	104
A. Appendix	105
A.1. Commercially Available Sensor Review	105
A.2. Circuit Schematics of the PCB Modules	106
A.3. Resin Characteristics	110
A.4. Cable Characteristics	111
A.5. Connector Characteristics	112
A.6. 3D Printer Raise 3D N2 Plus Specifications	113
A.7. Software Development	113
A.8. Multimeter Specifications	128
A.9. Photometer Specification	128
A.10. Spectrometer Specification	129
Declaration	130
Scientific Curriculum Vitae	131

List of Tables

6.1. Literature review on wavelengths used for CDOM and turbidity determination.	27
9.1. Software commands, settings and ranges.	46
11.1. Results of the statistical evaluation of the system stability test.	61
A.1. Brief review of commercially available transmissometer (attenuometer) systems used in applied research or industrial applications.	105
A.2. Resin characteristics	110
A.3. Cable LifyDY characteristics	111
A.4. Connector characteristics	112
A.5. 3D Printer Raise 3D N2 Plus Dual specification.	113
A.6. Multimeter specifications	128
A.7. Photometer specifications	128
A.8. UV-VIS spectrometer specifications	129
A.9. VIS-NIR spectrometer specifications	129

List of Figures

1.1.	A ship crosses an algae storm in the Baltic Sea (satellite image).	2
1.2.	Monitoring of Baltic swirls by remote sensing and in-situ sensors.	4
3.1.	Time series – Exemplary sampling data of temporal varying concentration.	9
3.2.	Spatial aspects in collecting environmental data and their impact on data interpretation.	10
3.3.	Spatio-temporal aspect of environmental data acquisition.	11
4.1.	The object specific exposure (OSE).	13
4.2.	Modeling scheme of a predictive monitoring approach.	13
4.3.	The predictive object specific exposure (POSE).	14
5.1.	The electromagnetic spectrum.	17
5.2.	The UV-VIS-IR spectrum of the electromagnetic spectrum.	18
5.3.	Geometry used to define inherent optical properties.	19
5.4.	Illustration of the Beer-Lambert Law.	21
5.5.	Differences in attenuation behavior of four different water samples.	23
5.6.	Transmittance spectrum of a water sample.	24
5.7.	Absorption spectrum of a water sample.	25
6.1.	Absorption spectrum of a given water sample.	26
6.2.	Principle of an in-situ transmission sensor probe (attenuometer).	28
7.1.	Schematic drawing of the I ² C bus.	33
8.1.	Abstracted modeling scheme of the sensor probe.	35
8.2.	Assembled communication unit (PCB).	36
8.3.	Assembled emitter unit (PCB).	37
8.4.	Assembled detector unit (PCB).	38
8.5.	Assembled pressure and temperature unit (PCB).	38
8.6.	Fully assembled sensor probe (3D printed) and inside view of the stacked electronic units.	41
8.7.	Sensor probe installed at the artificial reef of Nienhagen, Baltic Sea, Germany.	41
9.1.	Schematic drawing of the hardware architecture of the sensor system. . . .	42
9.2.	Image of the top side unit plugged into the microcontroller.	43

10.1.	LED driver test circuit.	50
10.2.	LED spectral test circuit.	50
10.3.	Schematic drawing of pressure dependence test setup.	51
10.4.	Schematic drawing of the temperature dependence test setup.	51
11.1.	Comparison of forward voltage U_{LED} measured by LED driver IC and digital multimeter (DMM).	52
11.2.	Comparison of forward current measured by LED driver IC and digital multimeter (DMM).	53
11.3.	Current-voltage characteristic of the IR LED	54
11.4.	Current-voltage characteristic of the UV LED	54
11.5.	Overview of the wavelength ranges relevant for the experimental setup for determining turbidity and CDOM content.	55
11.6.	Relative spectral emission of the UV LED	56
11.7.	Relative spectral emission of the IR LED	56
11.8.	Relative spectral emission of the UV LED due to changing PWM.	57
11.9.	Relative spectral emission of the IR LED due to changing PWM.	57
11.10.	Current-PWM modulation of the UV channel.	59
11.11.	Current-PWM modulation of the IR channel.	59
11.12.	Current-PWM modulation of the UV channel for selected forward currents.	60
11.13.	Current-PWM modulation of the IR channel for selected forward currents.	60
11.14.	Investigation of the system stability of the sensor system in submerged state.	61
12.1.	Pressure dependency test of the sensor probe (UV channel).	62
12.2.	Pressure dependency test of the sensor probe (IR channel).	63
12.3.	Temperature compensation test (UV channel).	64
12.4.	Temperature compensation test (IR channel).	64
13.1.	Comparison of CDOM approximations derived by the optical sensor system and a laboratory photometer.	65
13.2.	Comparison of turbidity approximations derived by the optical sensor system and a laboratory photometer.	66
14.1.	Map of the Baltic Sea region and the study area, the Unterwarnow along the city of Rostock.	68
14.2.	Sensor installation on a canoe for mobile monitoring.	70
14.3.	Sensor installation on a sailboat for mobile monitoring.	70
14.4.	Spatial plot of the temperature measurements of the monitoring campaign by canoe (2018-08-04).	71
14.5.	Spatial plot of the UV transmission measurements of the monitoring campaign by canoe (2018-08-04).	72

14.6.	Spatial plot of the IR transmission measurements of the monitoring campaign by canoe (2018-08-04).	73
14.7.	Time series of the monitoring results of the measurement campaign by canoe.	74
14.8.	Spatial plot of the temperature measurements of the monitoring campaign using a sailboat (2018-09-02).	75
14.9.	Spatial plot of the UV transmission measurements measurements of the monitoring campaign using a sailboat (2018-09-02).	76
14.10.	Spatial plot of the IR transmission measurements measurements of the monitoring campaign using a sailboat (2018-09-02).	77
14.11.	Time series of the monitoring results of the measurement campaign using a sailboat.	78
14.12.	Comparison of the transmission measurements of both optical channels during the field campaign.	79
17.1.	Predictive analytics - The informative value of data.	92
17.2.	Lambda architecture for data acquisition and data evaluation.	93
A.1.	Circuit schematic of communication unit.	106
A.2.	Circuit schematic of emitter unit.	107
A.3.	Circuit schematic of detector unit	108
A.4.	Circuit schematic of pressure and temperature unit	109
A.5.	LifYDY cable wire assignment.	111
A.6.	Schematic drawing of the connector pin out.	112

Acronyms

AOP	Apparent optical properties
CDOM	Chromophoric dissolved organic matter
CPTS	Casted pressure tolerant systems
DIN	German Institute for Standardization, <i>German:</i> Deutsches Institut für Normung e.V.
DOM	Dissolved organic matter
FAU	Formazine attenuation units
FFF	Fused filament fabrication
FPTS	Fluid compensated pressure tolerant systems
GPS	Global positioning system
I ² C	Inter-integrated circuit, serial computer bus
IC	Integrated circuit
IOP	Inherent optical properties
IP	IP Code, International Protection Marking, ac- cording to standard 60529 by the International Electrotechnical Commission (IEC)
IR	Infrared radiation
JSON	JavaScript Object Notation
LED	Light emitting diode
NIR	Near-infrared radiation
OSE	Object specific exposure
PCB	Printed circuit board
PETG	Polyethylene terephthalate glycol
POSE	Predictive object specific exposure
PTS	Pressure tolerant systems
PU	Polyurethane
PWM	Pulse width modulation
S-PVC	Polyvinyl chloride from suspension polymerization
USB	Universal serial bus
UV	Ultraviolet radiation

- VDE Association of Electrical Engineering, Electronics and Information Technology, *German: Verband der Elektrotechnik, Elektronik und Informationstechnik e.V.*
- VIS Visible light

List of Symbols

$a(\lambda)$	Spectral absorption coefficient	m^{-1}
$\alpha_{\lambda,\text{mol}}$	Molar absorption coefficient	$\text{m}^2 \text{mol}^{-1}$
$b(\lambda)$	Spectral scattering coefficient	m^{-1}
C	Concentration of absorbing material	mol l^{-1} or kmol m^{-3}
$c(\lambda)$	Spectral beam attenuation coefficient	m^{-1}
C_{DOM}	Concentration of dissolved organic matter	mol l^{-1} or kmol m^{-3}
d	Path length	m
$D(\lambda)$	Spectral absorbance	1
E	Photon energy	J
E_{λ}	Extinction	
$\epsilon_{\lambda,\text{mol}}$	Decadic molar extinction coefficient	$\text{m}^2 \text{mol}^{-1}$
e	Euler's number	
h	Planck constant	J s
I_{LED}	LED Forward Current	A
λ	Wavelength	nm
c	Light speed (vacuum)	m s^{-1}
ν	Photon frequency	Hz
Φ	Radiant power	W
$\Phi(\lambda)$	Spectral radiant power	W nm^{-1}
$\Phi_{\text{a}}(\lambda)$	Absorbed spectral radiant power	W nm^{-1}
$\Phi_{\text{i}}(\lambda)$	Incident spectral radiant power	W nm^{-1}
$\Phi_{\text{s}}(\psi_i, \lambda)$	Scattered spectral radiant power	W nm^{-1}
$\Phi_{\text{t}}(\lambda)$	Transmitted spectral radiant power	W nm^{-1}
p	Pressure	bar
ψ_i	Angle of scattered light beam	$^{\circ}$
$A(\lambda)$	Spectral absorptance	1
$C(\lambda)$	Spectral attenuation	1
$B(\lambda)$	Spectral scatterance	1
$T(\lambda)$	Spectral transmittance	1
ϑ	Temperature	$^{\circ}\text{C}$

t	Time	s
t_I	Integration time	s
U_{LED}	LED Forward Voltage	V
V	Volume	m^3
x	x dimension	
y	y dimension	
z	z dimension	

Part I.

Introduction

1. Motivation

Around 70 % of the Earth's surface is covered by water. Despite ongoing technological progress in monitoring and exploration technologies, large parts, especially marine and coastal waters, are scarcely researched or surveyed by an appropriate monitoring so far (Isoyama et al., 2017; Chapman, 1996). Since the impact of global change or the intensive use of natural resources show different effects on different scales, the demand for a better understanding of aquatic ecosystems and marine resources is considerably high. The main challenge is that there is still a lack of sufficient data. The provision of a methodological tool for a more data-driven development of monitoring strategies and goal-oriented modeling is therefore the essential objective of this work.

The appearance of annual algae blooms in the Baltic Sea is a recent example of how difficult it is to understand heterogeneous environmental systems and their dynamics. An adequate monitoring of such phenomena represents an engineering scientific challenge. The question is not only how such phenomena arise, but also how they can be measured in terms of their large spatial extent and temporal variance (see Figure 1.1).

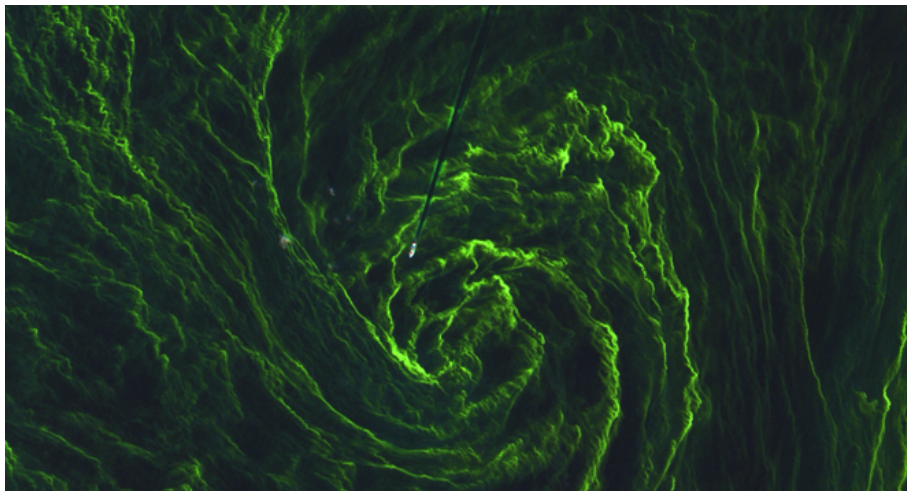


Figure 1.1.: Satellite image of a ship crossing an algae storm in the Baltic Sea. Copernicus Sentinel data (2015)/ESA, CC BY-SA 3.0 IGO.

Since the 1960s there have been regular measuring programs for hydrographic data collection, e.g. for the Baltic Sea, which are carried out by scientific and state institutions. Regarding the given example, the annually collected data allow a description of the situation of the central Baltic Sea basins at the time of the survey. In terms of temporal and spatial coverage, the data is insufficient, which is often the case particularly in highly

dynamic areas such as river estuaries or close to the access to the North Sea. Therefore, the data collected so far by scientific surveys, measuring buoys or measuring stations are not sufficient to adequately reflect the situation over a larger area.

1.1. Problem Description

To this day, data collection in the sea is very complex – and correspondingly expensive, because fast deployable measurement systems and adaptive methods are missing. Moreover, commercially available systems offer only limited possibilities for modification and adaptation. The availability of spatially and temporally high-resolved data is low. In most cases, monitoring data is limited to a few points, which are usually scientific measuring stations. While the Earth’s surface can be surveyed by remote sensing approaches (e.g. satellites for environmental observation, Copernicus program of the ESA), the corresponding data are missing in water layers below the optical penetration depth (von Schuckmann et al., 2016). In addition, satellite overflights only take place at intervals of several days and optical sensors used on satellites only provide usable results on cloudless days. A consistent monitoring of dynamic processes is not possible in this way. In particular, this applies to the adequate coverage of spatio-temporal scales, e.g. monitoring from local to regional scales.

With regard to the example of the Baltic Sea, it should also be noted that the largest environmental impacts on marine ecosystem of marginal seas such as the Baltic Sea are dominated by land-based sources. For example, the sources located in the Baltic Sea catchment area, are responsible for more than 90 % of the nutrient input into the sea (HELCOM, 2018). These are mainly rivers but also diffuse sources such as the input of polluted groundwater. Even large-scaled monitoring campaigns as described above are not suitable for an adequate monitoring of the important areas such as estuaries or rivers. Remote sensing methods are also unsuitable here due to the limited temporal and spatial resolution. Therefore, technologies are needed that enable a consistent in-situ monitoring of these areas with adequate temporal and spatial resolution to bridge the data gap between local and regional scales.

1.2. Situation Description

In the field of aquatic monitoring, key indicators have been established to describe, report and monitor such changes by means of laboratory analytical methods, remote sensing as well as in-situ sensors. The collection of water samples on site in combination with subsequent laboratory analysis provides highly accurate results, however, the procedure is complex and rather cost-intensive. Another factor is that such sampling of large-scaled areas is methodologically demanding and time-consuming, which leads to delays between sampling and the final results of the analysis. As a consequence, the overall data density in

many cases is not sufficient to give an holistic representation of ecosystem characteristics neither in temporal nor spatial resolution. Here, in-situ sensors and mobile monitoring technologies are increasingly used to achieve a better resolution. Therefore, new engineering approaches are under investigation to implement efficient on-site monitoring systems that can provide sensor readings as actionable information for decision making close to real time.

It is an often recognized problem in applied research that it is currently not possible or only possible with enormous effort to capture large-scaled processes by using standard methods. One example is the Clockwork Ocean¹ project, in which an international team of scientists led by the German Helmholtz Centre Geesthacht is trying to investigate the phenomenon of ocean vortices. Within the project, ocean vortices are being measured with extensive scientific effort using research vessels as well as towed and autonomous systems as sensor platforms in combination with remote sensing by satellites, airplanes and a research zeppelin. A preliminary result is given in Figure 1.2, where colored temperature gradients along transects are highlighted. Here, the demand for in-situ data with correspondingly high resolution becomes clear since remote sensing methods are representative of the water surface but not of the water body. Today, the in-situ data density is not sufficient to appropriately capture the dynamics as well as the spatial and temporal variance.

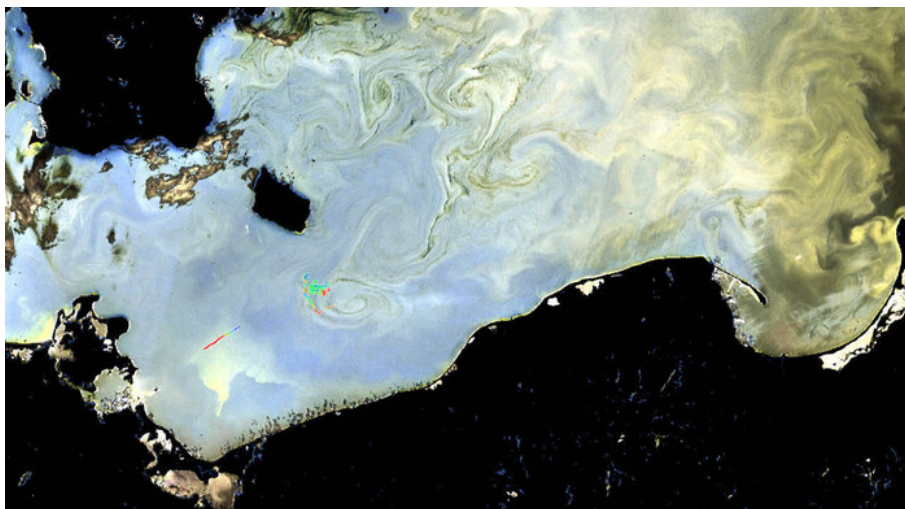


Figure 1.2.: Clockwork Ocean - Monitoring of Baltic swirls by remote sensing and in-situ sensors (contains modified Copernicus Sentinel data (2016)/HZG, CC BY-SA 3.0 IGO).

1.3. Goal

This dissertation investigates the dynamic monitoring of processes in complex ecosystems by using an optical sensor based measurement system. To address this problem, a fast method that includes the usage of data derived from mobile sensors is proposed to address

¹ www.uhrwerk-ozean.de

this problem. A sensor concept is to be formulated and a prototypical demonstrator is to be developed for the determination of optical properties of water. The basic feasibility will be shown with the help of a laboratory and a field study.

In summary, this dissertation aims to show a fundamental sensor development according to a sampling theorem from an ocean engineering perspective. The goal is to provide a system that allows reliable statements regarding the state of complex (eco-) systems with manageable sensor effort. Therefore, the aim is to increase the informative value of sensor data while reducing the effort for the user based on an underlying sampling theorem.

1.4. Requirements

In order to observe and understand complex processes as mentioned above, methods are needed that can provide reliable in-situ data for decision making in an adequate manner of time and effort. Here, sufficient sensor systems are not yet available. A decisive contribution to overcome this lack is seen in the development of an optical sensor probe, which is small in size, light-weight and field-applicable as a preliminary for local scaled in-situ data acquisition. Sensors for aquatic monitoring are exposed to high stresses and must therefore meet high demands. Consequently, an appropriate sensor probe should be pressure-tolerant to save weight and at the same time protect the electronic components from water ingress. In order to achieve a holistic sampling, the sensor probe should also have peripheral pressure and temperature sensors and should be configurable via a software interface. If these criteria are summarized, it becomes clear that the development of a sensor should be preceded by the introduction of a holistic sensor concept. In addition, integrated services such as an automated calibration routine or sensitivity adaption would significantly increase the system's field capability and the validity of the data. Moreover, an appropriate sensor concept should be modular in order to be able to change wavelength ranges in perspective, for example.

1.5. Expected Results

As a result, this dissertation will demonstrate the fundamental feasibility and the added scientific value of a holistic monitoring concept. A novel and adaptive sensor probe for fast monitoring of turbidity and dissolved organic matter is to be developed according to the method of requirements engineering to fulfill the demands for being used in ad-hoc monitoring applications. Finally, the availability of an evaluated method enables the formulation of reliable statements based on mobile and stationary measurements and provides an approach for contextualized monitoring of processes in nature. It is also intended to enable the monitoring of areas that cannot be monitored appropriately or only with difficulty using conventional methods. Another expected result is to create the technological basis to enable predictive environmental monitoring strategies in future.

1.6. Target Parameters - Turbidity and the Amount of Dissolved Organic Matter

Within this thesis, two water quality parameters are of paramount importance, chromophoric dissolved organic matter (CDOM) and turbidity. For better clearance, the meaning of these parameters in the field of environmental research as well as the characteristics will be briefly described.

Chromophoric Dissolved Organic Matter

Dissolved organic matter (DOM) is a broad classification for organic molecules of different origin and composition in aquatic systems. It is a sensitive indicator of the aquatic system health. DOM is of crucial importance for the sustainability of life functions of the high level organisms since a high increase in the DOM content can lead to eutrophication with serious consequences for ecosystem stability (Mostofa et al., 2013).

Anthropogenic influences can cause significant organic loads to enter surface waters, which can lead to intensive bacterial conversion processes, e.g. increased oxygen consumption (Kolka et al., 2008). Chromophoric Dissolved Organic Matter (CDOM) also known as yellow substances or *gelbstoffe* is an important subcategory of DOM. It is the light-absorbing fraction of the pool of dissolved organic matter and results mainly from the degradation of terrestrial and aquatic plant material. CDOM plays an important role in the global biogeochemical carbon cycle due to its production and consumption by phytoplankton and bacteria (Harvey et al., 2015). CDOM can have a significant effect on biological activity in aquatic systems since the absorption of CDOM affects the color of water and influences the underwater light field. In other words, the absorption of CDOM means that less radiation is available for photosynthesis, which has a significant effect on aquatic ecosystems (Lübben et al., 2009).

Turbidity

Turbidity represents the clearness of the water, as affected by suspended solids. The more turbid a water is, the less light there is available for photosynthesis (Bass et al., 1995). Turbidity is effecting the aquatic fauna, but also fish abundance and distribution. Moreover, turbidity is often related to nutrient richness, which is highly influencing an ecosystem (Chapman, 1996). Furthermore, knowledge of turbidity is important to enable appropriate corrective measures when working with optical measuring instruments in general (see Section 6).

2. Thesis Structure

This thesis is divided into several parts due to the complexity of the subject. The parts build on each other, hence the structure of the work is briefly explained in the following.

Part I In the *Introduction* part to this thesis, a general definition of the problem space is carried out. The motivation and also the objectives of the work are presented and the structure of the work is explained.

Part II In Part *Sensing as a Service*, a fundamental, systems-theoretical consideration of scientific environmental observation is carried out. The challenges of cross-scale monitoring are highlighted and a holistic sampling theorem, the *Object Specific Exposure* (OSE), is formulated. In addition, theoretical approaches for a predictive environmental monitoring are derived.

Part III The thesis part *Water Quality Assessment* provides a basic and comprehensive consideration of optical in-situ methods for determining water quality. Based on this consideration, the optoelectronic requirements for the sensor system are made.

Part IV The part *System Development* comprehensively describes the development of the sensor system starting from the underlying measurement conversion up to the integration into a sensor system according to the OSE sampling theorem.

Part V Within part *System Assessment*, a comprehensive system evaluation is carried out on the basis of laboratory tests to characterize the sensor and system performance.

Part VI Within the framework of the *Case Study*, the demonstration is made of how a mobile monitoring can be carried out with the help of the developed sensor system and how information can be derived in near real time according to the OSE sampling theorem.

Part VII Within the *Discussion* part of the work, a closed and thorough discussion of all aspects is carried out. A fundamental discourse is presented to the reader starting with the scientific evaluation of the OSE sampling theorem and the assessment of the developed sensor system up to the debate on the case study.

Part VIII In the last part *Conclusion and Outlook* of the dissertation a summary of the results is given. In addition, central requirements for further work are formulated and concrete approaches are named, such as the DEEP-SEA project, which emerged from this dissertation.

Part II.

Sensing as a Service – Towards Holistic Paradigms in Environmental In-situ Monitoring

3. Environmental Monitoring and Observation - A Matter of Space and Time

Besides the development of a field-capable sensor probe for the determination of optical properties of water, a major part of this work is dedicated to the conception and implementation of a new sampling strategy. Processes in nature and especially in aquatic, coastal or oceanic environments are highly variable in terms of time and space. Therefore, the measuring task of a service-oriented sensor system consists not only in the acquisition of a physical state variable, e.g. the content of dissolved organic matter, but also in the connection with spatio-temporal references. Based on this, it becomes clear that the assessment of water quality is also a function of the location, the time and the surrounding conditions. In practice, this is leading to major logistical challenges regarding the monitoring of such processes and places enormous demands on the research infrastructure.

3.1. Temporal Aspects of Environmental Data Acquisition

A basic method in the field of environmental monitoring is the collection of data as a time series at a defined location and with a fixed sampling rate T with $t_1 = T$, $t_2 = 2T$ and $t_3 = 3T$ as illustrated in Figure 3.1.

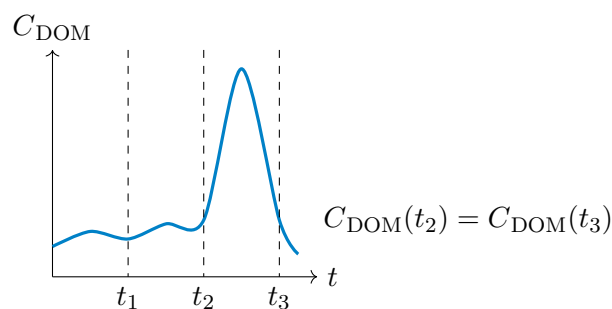


Figure 3.1.: Time series – Exemplary sampling data of temporal varying concentration.

In order to record environmental processes and their temporal change, the sampling rate must be selected according to the rate of change of the phenomenon as it can be described by the Shannon sampling theorem (Jerri, 1977). In relation to the specific case, this means that to accurately monitor the variable, it must be sampled at a rate greater than twice the highest frequency component of the variable. The illustrated case in Figure 3.1 reveals that the selected sampling rate T is prone to misinterpretation since the sudden

increase of the measured variable, here the concentration of dissolved organic matter, was not recorded between t_2 and t_3 . Processes in nature can have a periodic dynamic, e.g. day-night-cycle or tides. However, in most cases the dynamic is not known, too complex to predict or simply non-periodic. Therefore, it should be noted that a major challenge in environmental monitoring is the appropriate recording of non-periodic or chaotic events.

3.2. Spatial Aspects of Environmental Data Acquisition

Besides the temporal aspect, it is above all the spatial reference that is important during the collection and analysis of environmental data. In addition to the spatial reference that corresponds to a geo-coordinate system, environmental observation can also be interpreted according to other assignments, e.g. along a coastal line or river courses. Figure 3.2 shows how the spatial distribution of sampling points can lead to different interpretations of environmental data.

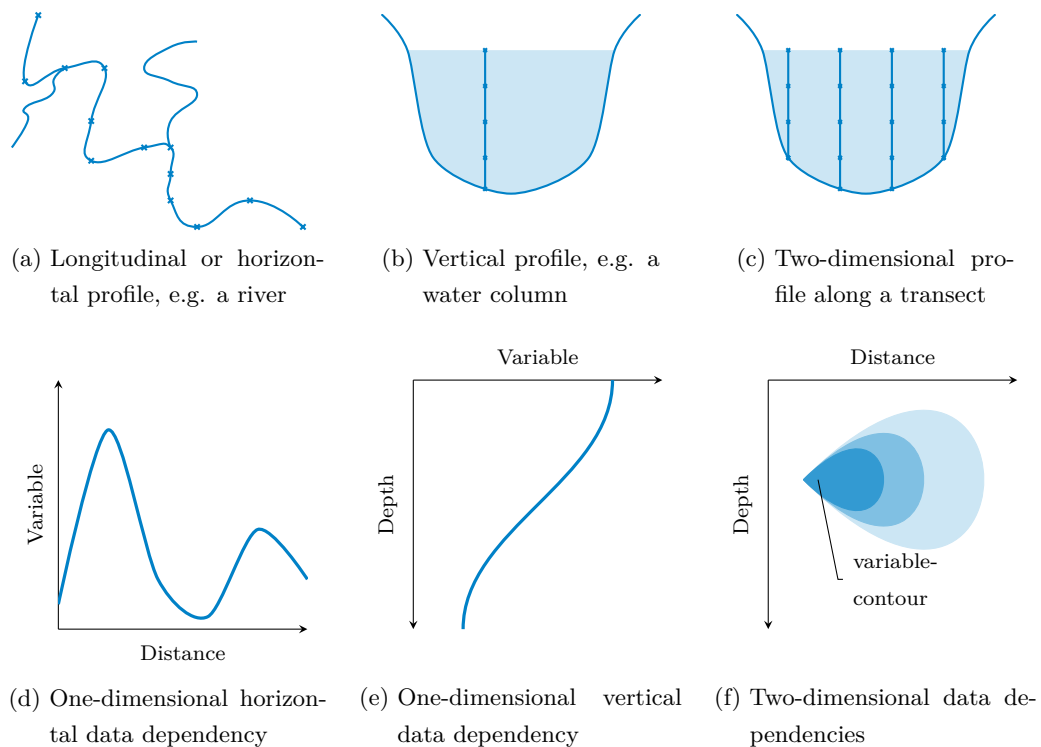


Figure 3.2.: Spatial aspects in collecting environmental data and their impact on data interpretation (adapted from (Chapman, 1996)).

For example, if water samples are taken along a river course (see Figure 3.2a), the data obtained should be interpreted as a function of the distance or river sections (see Figure 3.2d). A similar dependency arises when water samples are taken from different depths of a water body (3.2b). The data obtained are interpreted as vertical profiles and thus as a function of the water depth (3.2e). If these two approaches are combined with each

other and, for example, several profiled water samples are taken along a transect (3.2c), a two-dimensional dependency on both water depth and distance arises (3.2f).

3.3. Spatio-temporal Aspects of Environmental Data Acquisition

Since the collection of environmental data is time-discrete and space-discrete, problems arise when recording spatially distributed and temporally variable processes using different sampling strategies as shown below in Figure 3.3.

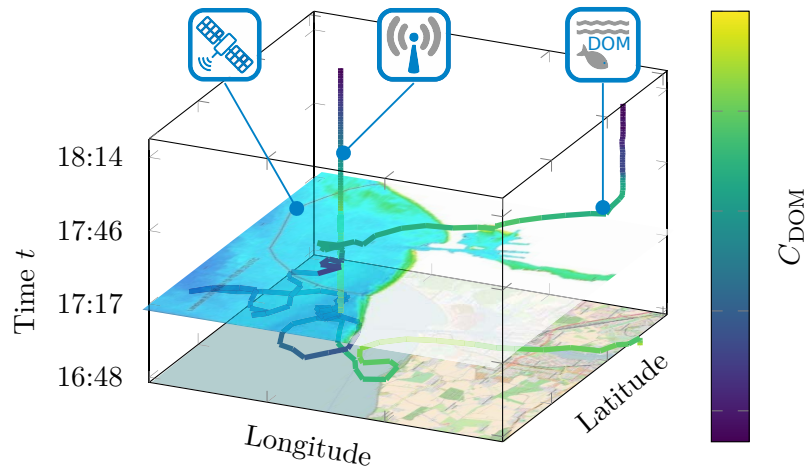


Figure 3.3.: Spatio-temporal aspect of environmental data acquisition, where multi-scalar data sources have to be taken into account. The illustration contains exemplary data and is adapted from Schima et al. (2017).

Due to the fact that processes in nature are linked to each other, an adequate monitoring must be adapted to these circumstances. From an engineering perspective, this is a problem of multi-scale data sources. A stationary sensor has two variable scales, the time t and the corresponding measured variable, e.g. the content of dissolved organic matter (DOM) represented by the concentration C_{DOM} . At the same time, remote sensing data, e.g. from satellites, can be seen as spatial data that represent a varying measured value at a given time, e.g. ocean color in relation to longitude and latitude. In case of mobile sensor data collection, the measuring system must both record the change in the measured variable over time and guarantee the spatial referencing of the measurement. What is not shown in Figure 3.3, is the requirement that especially aquatic monitoring must also take into account the corresponding sampling water depth. Here, it should be emphasized that optical methods of remote sensing are limited to the optical penetration depth into the water body, which depends on a variety of different conditions. These interrelationships are a major reason why a cross-scale environmental monitoring is still the subject of ongoing research.

4. Towards a Comprehensive Sampling Theorem for Monitoring Applications

On the basis of the mentioned spatio-temporal aspects it is possible to assign phenomena observed in the environment to spatially and temporally changing state variables, e.g. DOM concentration C_{DOM} , and to render them in a mathematically describable way. For this purpose, the effect of a state variable is abstracted and referred to as *Exposure*. This is important for the development of adaptive sensor systems as presented in this thesis.

4.1. Object Specific Exposure (OSE)

Assuming the case of a stationary measurement of DOM concentration C_{DOM} over a defined period of time $\Delta t = t_i - t_0$, the following basic assumption about the *temporal Exposure* results in

$$\text{temporal Exposure} = \int_{t_0}^{t_i} C_{\text{DOM}}(t) dt. \quad (4.1)$$

If a mobile data collection of the DOM concentration C_{DOM} is now assumed, the expression expands with the number of the variable scales as the spatial references $\Delta x = x_i - x_0$, $\Delta y = y_i - y_0$ and $\Delta z = z_i - z_0$ also change due to the movement.

$$\text{spatio-temporal Exposure} = \int_{x_0}^{x_i} \int_{y_0}^{y_i} \int_{z_0}^{z_i} \int_{t_0}^{t_i} C_{\text{DOM}}(t, x, y, z) dt dx dy dz \quad (4.2)$$

It becomes clear that this leads to a description of a highly specific *spatio-temporal Exposure*, e.g. for an object that is assigned and contextualized to the particular sampling.

In addition, if the assignment to a context is made (e.g. to known industrial activities), the measured variables can be better compared and therefore generalized. This is an important requirement for transferring observation data to models and moreover, for providing actionable information for decision making (Schima et al., 2017). This assignment also applies to the usage or deployment of a mobile sensor, which leads to a fundamental sampling theorem creating the basis of this thesis, the Object Specific Exposure (OSE) as shown in Figure 4.1.

When applied to a sensor system, compliance with the OSE theorem means that measured values are always collected in the correct space and time reference, similar to a measurement protocol. This allows to compare a measurement with a-priori information and moreover, to interpret it in a holistic way. For the development of a monitoring strategy, this also means that the sensor system must be able to determine such relations and references autonomously or at least provide functions to handle user input.

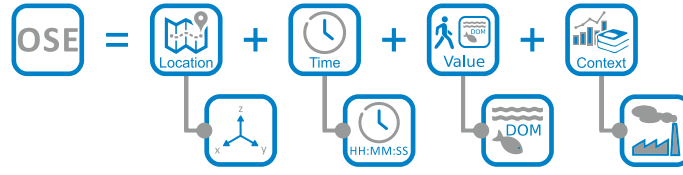
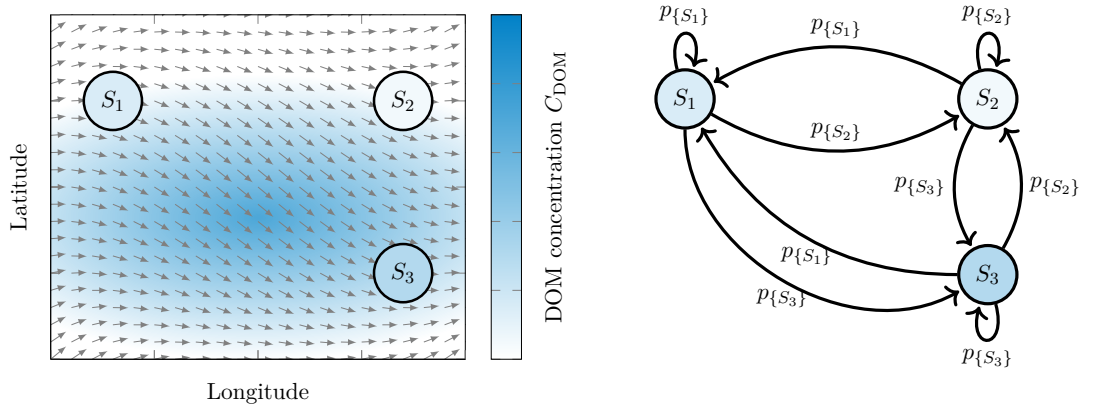


Figure 4.1.: The object specific exposure (OSE) is the change of a state variable within a certain time and space assigned to a given context (Schima et al., 2017).

4.2. Predictive Object Specific Exposure (POSE)

Regarding the given example of the contextualized recording of the DOM concentration, the sampling theorem introduced above can be extended by a predictive component. This can be achieved by using a sufficient amount of observations as a knowledge basis derived by e.g. long-term monitoring. This could be the case, for example, if a river section has been instrumented with the corresponding sensors to determine the DOM concentration C_{DOM} but in addition, the flow information, e.g. in form of a flow pattern, is given as shown in Figure 4.2a. The flow pattern is illustrated by grey arrows indicating the direction of flow.



(a) Exemplary case of a river segment with known flow pattern where the DOM concentration C_{DOM} could be approximated (predicted) based on measured sensor values (S_1 , S_2 , S_3) used as input parameters. The blue color gradient describes a DOM plume.

(b) An abstract modeling scheme as topological structure to ensure predictive monitoring based on a Markov chain. $p_{\{S_i\}}$ describes the probability whether a change of state occurs in the next time step.

Figure 4.2.: Modeling scheme of a predictive monitoring approach by using a-priori information such as a flow pattern and time series for state estimation.

By knowing the flow pattern of the river segment, forecasts can be made to approximate the *Exposure*. The illustration in Figure 4.2a shows three sensor nodes that record the DOM concentration C_{DOM} over time at different sampling locations based on the OSE theorem. According to the flow pattern, it is quite clear that sensor node S_2 will be

exposed to less stress than sensor node S_3 . Moreover, if the flow velocity is constant, even a quantitative prediction based on a model calculation (e.g. Gaussian Plume) can be made where the readings of sensor node S_1 are used as input or starting condition of the calculation (prediction).

For predictive monitoring, an appropriate topological structure can be defined that maps the relationship between the individual nodes or sampling locations. Here, a structure similar to a Bayesian network or Markov chain is reasonable, which also permits probability considerations (see Fig. 4.2b). $p_{\{S_i\}}$ describes the probability whether a change of state occurs in the next time step for a specific node or for an adjacent sensor node.

For the implementation of the hardware, it is important to define an abstract scheme for providing a reasonable framework. Within this framework the sensor nodes can be identified and structured according to location, time, exposure, context or to previously observed events. The topological structure can also be extended to a construct similar to a Markov chain. In the case of environmental monitoring, time-synchronous data acquisition must be guaranteed for all sensor stations or considered sensor nodes. In case of an event, the change in the state variable of a single sensor can be used to predict the state of a sensor node next to it or the upcoming state of the particular node. Thus it can be determined that by knowing the context and peripheral process variables, the OSE can be better interpreted. However, also predictive statements can be derived leading to a further theorem, the Predictive Object Specific Exposure (POSE). Here again, the exposure will be contextualized in relation to the time and location. As described in the example above, the POSE theorem also recognizes a-priori information about processes and dynamics as shown in Figure 4.3.

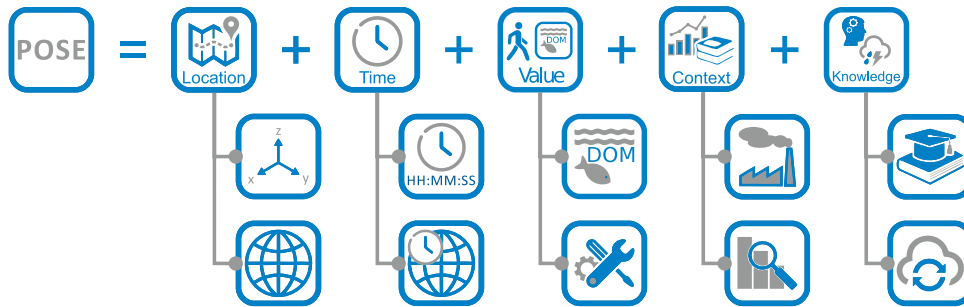


Figure 4.3.: The predictive object specific exposure (POSE) determines the influence of a state variable within a certain time and space assigned to a given context and derives predictions based on the assessment of peripheral processes and a-priori information (adapted from Schima et al. (2017)).

Part III.

Water Quality Assessment - Potentials and Challenges of Optical In-situ Measurements

5. The Assessment of Water Quality

Before the technological challenges and engineering findings of this work will be described, a more general discussion of the assessment of water quality and the related scientific-physical fundamentals is given. They form the underlying measurement principle of the sensor system.

It is undisputed that water is one of the most important prerequisites for life. Sea and coastal waters in particular are subject to competing forms of use and interests such as transportation and logistics, fishing and aquaculture, marine mining, energy production, tourism or recreation (OECD, 2016). In parallel, the growth of the world's population combined with an increasing urbanization are leading to major social, economic and ecological challenges (World Economic Forum, 2016). For these reasons there are numerous approaches and methods to assess the water quality.

In dependence of the survey or monitoring purpose, methods and measurement techniques which are used to determine water quality are varying (Chapman, 1996). In other words, different parameters and a-priori information are taken into account for the monitoring and assessment of aquatic ecosystems. These can be satellites for global observation of the sea surface as well as modern research vessels, autonomous operating platforms or equipment carriers on the surface of the sea, in water bodies or on the seabed (Kreuzer and Solowjow, 2018; Zerr et al., 2016; von Schuckmann et al., 2016; Moore et al., 2009).

5.1. Potential of Optical Measurement Principles

Sensors and sensor systems that allow in-situ measurements are of particular interest, as they provide direct information about the status of the aquatic body. In addition, optical in-situ sensors represent a fast and simple to use technology for the determination of water quality. In dependence on the wavelength as well as the experimental setup, a large number of parameters can be determined. Even though sensor systems are commercially available, that can perform stationary as well as mobile measurements, their functionality is limited in terms of data handling and user interactions (Venkatesan et al., 2018). Most commercially available systems require extensive user knowledge. One of the reasons for this is that in most cases solely sensor probes and not sensor systems, e.g. in combination with loggers or addition processing units, are offered by the manufacturers. The sensors are usually closed systems and it is rarely possible to make adjustments or to implement an adaptive sensor behavior. How such a sensor behavior could be achieved will be explained in the next section on the basis of the underlying optical measurement principles.

5.2. Optical Characteristics of Water

Since natural waters are a composition of pure water and a varying mixture of dissolved substances and particulate matter, different optical and electro-chemical properties, depending on the composition of dilutes and particles, can be observed (Moore et al., 2009). Based on this phenomena, different analytical methods can be found which are used in laboratory and field applications for water quality assessment (Moore et al., 2009; Chapman, 1996). Especially optical measuring principles are often used since solutes and particulates in water lead to changes in the optical characteristics and appearance of water. But, the optical properties of natural waters show a high dynamic due to spatio-temporal variations. This is also the reason why the qualitative and quantitative estimation of water remains to be a challenging task, especially under field conditions (Bass et al., 1995).

To differentiate the optical properties of water, it is advisable to initially consider the electromagnetic wave spectrum and the different interactions with water, that can be observed. As Figure 5.1 illustrates, the electromagnetic wave spectrum can be divided into different areas according to the wavelength, whereas wavelength ranges with similar properties are grouped into categories.

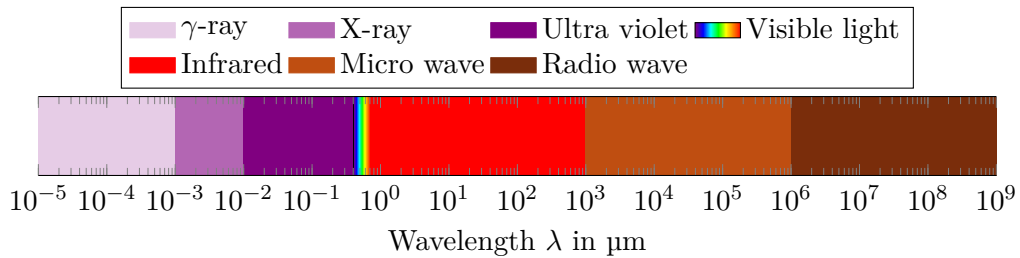


Figure 5.1.: The electromagnetic spectrum as a representation of the wavelength range λ of the electromagnetic radiation.

The energy E of a photon with the frequency ν is defined as shown in equation 5.1, whereas h is Planck's constant, c the speed of light in vacuum and λ the wavelength.

$$E = h \cdot \nu = \frac{h \cdot c}{\lambda} \quad (5.1)$$

Ordered according to decreasing frequency ν and thus increasing wavelength λ , the short-wave and thus high-energy gamma rays are located at the beginning of the spectrum. The different bands of the spectrum show different characteristics and interact differently with matter. The frequency and therefore the energy of the photon defines how molecules are excited and which molecules can be excited at all (Bass et al., 1995). This is due to the phenomena that if a photon with the frequency ν and the energy E hits a molecule, the molecule can be changed from a stable ground state to an excited state (photon excitation). This applies to water molecules as well as to dissolved compounds and particular matter in the water column (Mobley, 1995). Since the electrons of an atom

cannot reach arbitrary energy levels, discrete energy levels can be observed due to photon excitation. The discrete energy amount required to reach these levels differs from element to element and is therefore a characteristic of different substances. For these substances, the internal molecular energy is the sum of electronic energy, vibration energy and rotational energy. This means when energy is irradiated onto a molecule, different changes in state can occur depending on the amount of energy in the radiation. This effect can be used, e.g. to identify substances and their amount in a given water sample. In the context of the present work, the ultraviolet (UV), visible (VIS) and infrared (IR) ranges of the electromagnetic spectrum are of primary interest. The proportion of light visible to the human eye is between $\lambda = 380$ nm and $\lambda = 780$ nm. As shown in Figure 5.2, it is common to assign the range between $\lambda = 400$ nm and $\lambda = 700$ nm to the visible range (VIS). Light of a longer wavelength is assigned to infrared radiation (IR) up to $\lambda = 1$ mm. Whereas UV radiation is assigned to the range between $\lambda = 190$ nm and $\lambda = 400$ nm (Preisendorfer, 1976).

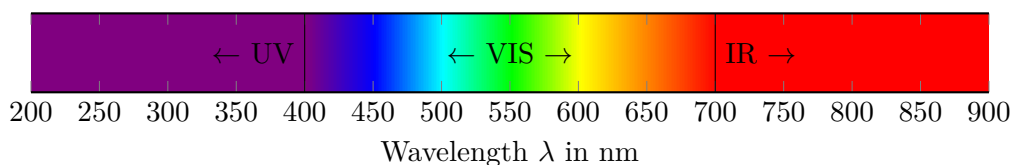


Figure 5.2.: The UV-VIS-IR spectrum of the electromagnetic spectrum.

For the analysis of aqueous samples, a variety of techniques and methods for determination and quantification can be found in different wavelength ranges, but the underlying principles are quite similar. As described above, electrons can be stimulated by light to reach higher energy states, which is mostly the case within the UV range. Also the proportion of molecular vibration can be increased (IR range) as well as the molecular rotation, which is true for IR radiation with high wavelengths and microwaves. In the UV range of light, the proportion of induced vibration and rotational energy is lower than the electronic proportion (Bass et al., 1995). Regarding the contribution to energy transmission due to the photon excitation, several close located energy levels are usually excited. This leads to an attenuation in the spectral lines of the absorbed light quanta. Normally, an absorption band is formed consisting of a number of closely located lines in the spectrum. If light is passing through a liquid medium, these lines overlap due to the free structure of the molecules, creating a continuous absorption spectrum as a characteristic of each element (Ozaki and Kawata, 2015).

5.3. Inherent Optical Properties

Based on these considerations, some fundamental observations regarding the optical properties of water can be made. In dependence on the wavelength and the system arrangement,

different optical appearance of water can be observed. This is in particular due to the fact that light, when passing through the medium, can either be absorbed, scattered (deflected) or transmitted without being disturbed at all. Therefore, a basic differentiation regarding the optical characteristic can be made between apparent optical properties (AOP) and inherent optical properties (IOP), such as attenuation, absorption or scattering and back scattering (Preisendorfer, 1976). In the context of this work, only the inherent properties of water are to be considered, from which the apparent properties can be determined, e.g. by knowing the incident radiation field. In order to describe the different phenomena in detail, a simplified illustration is given in Figure 5.3. In the given example, the beam paths of incident light through a defined volume of clear water are to be examined.

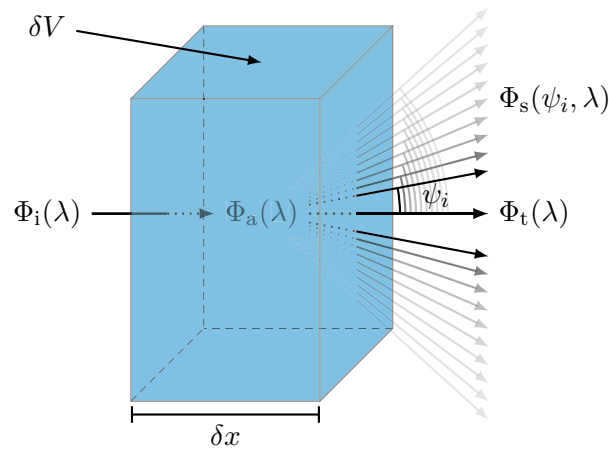


Figure 5.3.: Simplified geometry of a defined volume of water to define inherent optical properties and path ways of light (adapted from Bass et al. (1995)).

To describe the light field in the water shown in Figure 5.3, it is necessary to introduce some definitions first. In this context, the spectral radiant power Φ is the power that can be either emitted, transmitted or absorbed in the form of radiation. The unit of the radiant power Φ is W. The radiant power Φ can also be related to the wavelength λ , which leads to the spectral power $\Phi(\lambda)$ or spectral flux with the unit W nm^{-1} (Bass et al., 1995). Based on this assumption, different beam paths of a monochromatic collimated light beam $\Phi_i(\lambda)$ through an aqueous medium with the volume dV and the thickness dx can be considered as shown in Figure 5.3. Assuming the simplified case that the incident light passes through the aqueous medium unhindered leads to the assumption that the amount of incident radiant power $\Phi_i(\lambda)$ is equal to the amount of transmitted radiant power $\Phi_t(\lambda)$. In the case of 100 % transmission, the formal correlation is as follows:

$$\Phi_i(\lambda) = \Phi_t(\lambda) \quad (5.2)$$

Another aspect that should be taken into account is the scattering of light. Light scattering changes the direction of photon transport by angles of ψ_i and disperses it when penetrating a sample as shown in Figure 5.3. However, the wavelength of the light does not change.

Taking into account the scattered light $\Phi_s(\psi_i, \lambda)$ and the transmission $\Phi_t(\lambda)$, the following formal relationship results in

$$\Phi_i(\lambda) = \Phi_s(\psi_i, \lambda) + \Phi_t(\lambda). \quad (5.3)$$

In addition, there is the possibility that light is being absorbed ($\Phi_a(\lambda)$) and the radiant energy is converted into light of different wavelength or chemical energy. This leads to the following relation.

$$\Phi_i(\lambda) = \Phi_a(\lambda) + \Phi_s(\psi_i, \lambda) + \Phi_t(\lambda) \quad (5.4)$$

Based on this assumption it is now possible to quantify the absorptance, scattering and therefore, the transmission of a given water sample. The spectral absorptance $A(\lambda)$ is the fraction of incident spectral power $\Phi_i(\lambda)$ that is absorbed within the volume dV .

$$A(\lambda) = \frac{\Phi_a(\lambda)}{\Phi_i(\lambda)} \quad (5.5)$$

Similarly, the spectral scatterance $B(\lambda)$ is the fractional part of the incident spectral power $\Phi_i(\lambda)$ that is scattered out of the beam.

$$B(\lambda) = \frac{\Phi_s(\psi_i, \lambda)}{\Phi_i(\lambda)} \quad (5.6)$$

The same applies to the spectral transmittance $T(\lambda)$, which is the fractional part of the incident spectral power $\Phi_i(\lambda)$ that is neither scattered nor absorbed.

$$T(\lambda) = \frac{\Phi_t(\lambda)}{\Phi_i(\lambda)} = \frac{\Phi_i(\lambda) - \Phi_a(\lambda) - \Phi_s(\psi_i, \lambda)}{\Phi_i(\lambda)} \quad (5.7)$$

According to equation 5.4, all fractional parts of the incident spectral power $\Phi_i(\lambda)$ can be summarized.

$$A(\lambda) + B(\lambda) + T(\lambda) = 1 \quad (5.8)$$

The attenuation $C(\lambda)$ can be expressed as a quotient of the difference between the incident spectral power $\Phi_i(\lambda)$ and the portion of the spectral power $\Phi_t(\lambda)$ that passes through the water volume dV to the incident spectral power $\Phi_i(\lambda)$ (Prien, 1999).

$$C(\lambda) = \frac{\Phi_i(\lambda) - \Phi_t(\lambda)}{\Phi_i(\lambda)} = 1 - \frac{\Phi_t(\lambda)}{\Phi_i(\lambda)} \quad (5.9)$$

Common inherent optical properties in hydrological optics are the spectral absorption coefficient $a(\lambda)$ and the scattering coefficient $b(\lambda)$, which express the spectral absorption $A(\lambda)$ and the scattering $B(\lambda)$ per distance unit δx in the medium. For the spectral absorption coefficient the following expression can be found.

$$a(\lambda) = \lim_{\delta x \rightarrow 0} \frac{A(\lambda)}{\delta x} \quad (5.10)$$

Similarly, the following relationship results for the scatter coefficient $b(\lambda)$.

$$b(\lambda) = \lim_{\delta x \rightarrow 0} \frac{B(\lambda)}{\delta x} \quad (5.11)$$

Finally, this consideration leads to the following expression for the attenuation coefficient.

$$c(\lambda) = \lim_{\delta x \rightarrow 0} \frac{C(\lambda)}{\delta x} = a(\lambda) + b(\lambda) \quad (5.12)$$

In terms of the technical application of the above described phenomena another consideration should be taken into account. As mentioned by Bass et al. (1995) and Mobley (1995) it should be noted that there is a difference between the quantity absorptance $\Phi_a(\lambda)$ and the optical density $D(\lambda)$, which is also called absorbance or attenuation (see eq. 5.22).

$$D(\lambda) = \log_{10} \frac{\Phi_i(\lambda)}{\Phi_s(\psi_i, \lambda) + \Phi_t(\lambda)} = -\log_{10} [1 - A(\lambda)] \quad (5.13)$$

Regarding the present work $D(\lambda)$ is also the measurable quantity that can be estimated using a laboratory photometer or spectrophotometer (Bass et al., 1995).

In all these considerations, it should be noted that these processes are wavelength-specific. This means that light of different wavelengths can be absorbed, scattered or transmitted differently. Moreover, these processes can be influenced by temperature, pressure and the mixture of different constituents in the water sample (Bass et al., 1995).

5.4. Beer-Lambert Law

The Beer-Lambert-Bouguer Law is fundamental for working with UV/VIS absorption spectroscopy. The law states that radiation $\Phi_i(\lambda)$ that passes through a given isotropic medium at a specified path length δx loses intensity due to the absorbing properties of the medium with a given concentration C (see Figure 5.4).

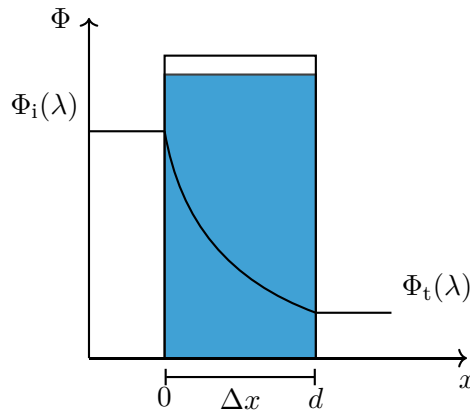


Figure 5.4.: Radiation when passing through an aquatic medium with the concentration C and the thickness Δx loses intensity due to the absorbing properties of the medium (simplified illustration of the Beer-Lambert Law).

The absorbed part of the incident light $\Phi_i(\lambda)$ is proportional to the thickness of the irradiated medium d or to the path length dx (Bass et al., 1995).

Based on this consideration, the following proportionality can be formulated.

$$d\Phi \propto -\Phi(x) C dx \quad (5.14)$$

The negative sign takes into account that Φ decreases. Now, a proportionality constant, the extinction coefficient $\alpha_{\lambda, \text{mol}}$, is introduced and the result is as follows.

$$d\Phi = -\alpha_{\lambda, \text{mol}} \Phi C dx \quad (5.15)$$

By rearranging equation 5.15 to Φ the following expression results.

$$-\frac{d\Phi}{\Phi} = \alpha_{\lambda, \text{mol}} C dx \quad (5.16)$$

Integrating both sides and solving for Φ for a material of thickness d gives

$$-\int_{\Phi_i(\lambda)}^{\Phi_t(\lambda)} \frac{1}{\Phi} d\Phi = \alpha_{\lambda, \text{mol}} C \int_0^d dx \quad (5.17)$$

and finally

$$-[\ln(\Phi_t(\lambda)) - \ln(\Phi_i(\lambda))] = \alpha_{\lambda, \text{mol}} C d \quad (5.18)$$

$$-\ln\left(\frac{\Phi_t(\lambda)}{\Phi_i(\lambda)}\right) = \alpha_{\lambda, \text{mol}} C d \quad (5.19)$$

The extinction is defined by the decadic logarithm. Therefore, the extinction coefficient $\epsilon_{\lambda, \text{mol}}$ is introduced.

$$\epsilon_{\lambda, \text{mol}} = \log_{10}(e)\alpha_{\lambda, \text{mol}} \approx 0.434 \alpha_{\lambda, \text{mol}} \quad (5.20)$$

Since the extinction coefficient $\epsilon_{\lambda, \text{mol}}$ is a measure for the conversion of radiant energy into heat and chemical energy, it can be numerically regarded equal to the proportion of energy absorbed by a light beam per unit distance in an absorbing medium. With $\epsilon_{\lambda, \text{mol}}$ integrated into equation 5.19 the following expression results.

$$-\log_{10}\left(\frac{\Phi_t(\lambda)}{\Phi_i(\lambda)}\right) = \epsilon_{\lambda, \text{mol}} C d = E_{\lambda} \quad (5.21)$$

Finally, the usual form of the Beer-Lambert Law is obtained by applying the logarithm power rule.

$$E_{\lambda} = \log_{10}\left(\frac{\Phi_i(\lambda)}{\Phi_t(\lambda)}\right) = \epsilon_{\lambda, \text{mol}} C d \quad (5.22)$$

Based on eq. 5.22 it can be deduced that the extinction coefficient $\epsilon_{\lambda, \text{mol}}$ significantly influences the measuring range. Many organic molecules have very high values for $\epsilon_{\lambda, \text{mol}}$ allowing the determination of very low concentrations, which forms the basis of spectrophotometry. The extinction coefficient $\epsilon_{\lambda, \text{mol}}$ is a wavelength-dependent substance constant but is also depending on the ambient measuring conditions. This means that the temperature ϑ , the pressure p or the pH value as well as other parameters can influence the absorption behavior. The Beer-Lambert Law only applies to absorption spectrometry in the range of Ultraviolet radiation (UV)/Visible light (VIS), Infrared radiation (IR) and atomic absorption spectroscopy. In addition, it only applies to the application of monochromatic light (peak wavelength). This means that the light absorption in the sample may be measured with electromagnetic radiation of a discrete wavelength.

5.5. Properties of Natural and Optically Complex Waters

As already mentioned, natural waters appear as a mixture of different dissolved substances and particulate matter. In nature, different processes can influence this composition and therefore, the water quality varies (Moore et al., 2009; Mobley, 1995; Preisendorfer, 1976). Regarding the optical determination of water quality this can lead to challenging phenomena since the perceptible attenuation of dissolved and particulate matter is wavelength-dependent. In case of organic loads in turbid waters, methods are needed to distinguish between the different parameters. Figure 5.5 may help to illustrate this effect based on water samples with changing concentration of chromophoric dissolved organic matter (CDOM) and different turbidity values.

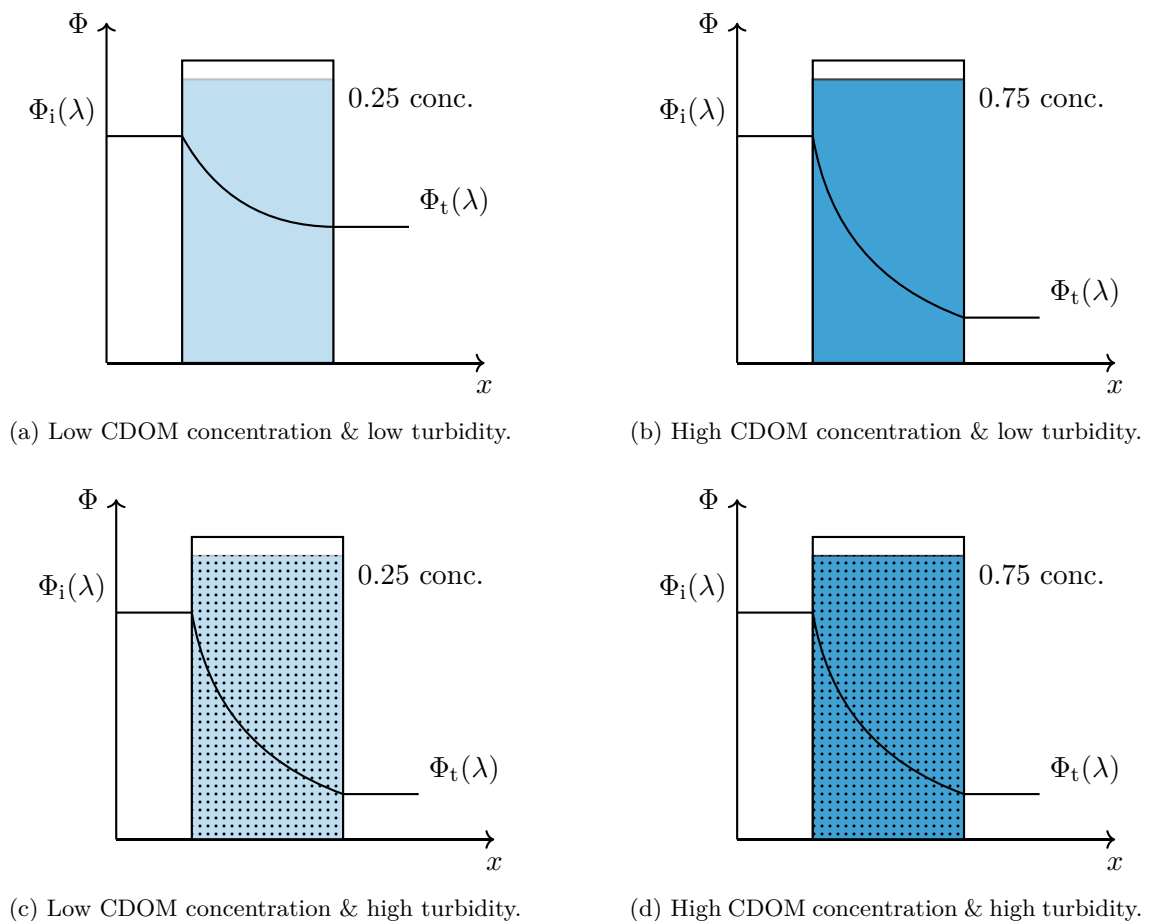


Figure 5.5.: Differences in attenuation behavior of four different water samples with changing CDOM concentration and turbidity.

Since the attenuation is a wavelength-dependent substance constant (see previous section), it can be challenging to distinguish between the measured signals (transmittance) at different wavelengths. Figure 5.5a shows that a monochromatic, collimated light beam $\Phi_i(\lambda)$ passing through a non-turbid sample of water with low CDOM concentration is

being slightly absorbed due to the processes described above. If the light beam is passing through a non-turbid water sample with a higher CDOM concentration, the amount of transmitted light $\Phi_t(\lambda)$ will decrease (see Figure 5.5b). In these cases the change in attenuation due to the CDOM concentration can clearly be distinguished using the corresponding attenuation wavelength.

Assuming that the water sample that is to be tested shows a significantly increased turbidity, the measurement leads to a misinterpretation (compare 5.5c and 5.5d). In this case, the high turbidity can result in misinterpretation for both the low and the high CDOM concentration (apparently) being assigned to the same low transmittance value for the corresponding wavelength. In laboratory analytical practice, water samples are therefore filtered before the measurement begins (see DIN 38404-3 (2005)). Related to the application of an optical in-situ sensor in the field, this is not possible. For this reason, reference measurements in other wavelength ranges, e.g. ranges where CDOM shows no attenuation, must be carried out for the interpretation of the measured values (turbidity compensation).

5.5.1. Transmittance Spectrum of a Natural Water Sample

For a better understanding, it is useful to contemplate at a transmittance spectrum for a natural water sample, as it can be determined e.g. with a laboratory photometer. Therefore, a transmittance spectrum of a water sample from $\lambda = 300$ nm to $\lambda = 900$ nm with a step width of $\Delta\lambda = 2$ nm is shown in Figure 5.6.

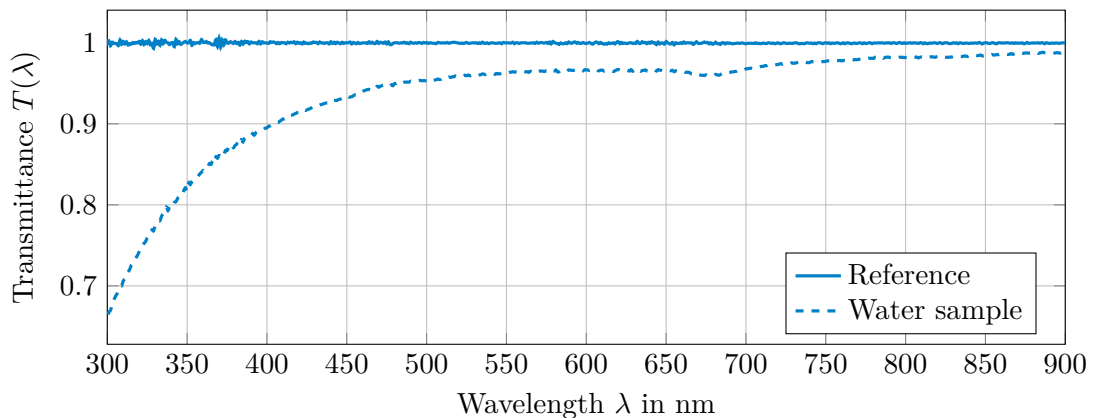


Figure 5.6.: Transmittance spectrum of a water sample.

The sample referred to as *Reference* was purified water. The water sample was taken from a boat dock in the city of Rostock and was not filtered before the measurement. Due to the wavelength-dependence of the attenuation, different values for the transmittance can be observed. The transmittance spectrum shows a strong signal reduction, especially in the UV range below $\lambda < 400$ nm, which can be related to organic loads within the water sample (Mostofa et al., 2013). Another aspect that becomes obvious is that the turbidity

of the given sample leads to a loss in intensity in the entire wavelength range. This effect can be used to derive a method for turbidity compensation.

5.5.2. Extinction Spectrum of a Natural Water Sample

Based on the measured transmittance, the attenuation (extinction) can be calculated according to equation 5.22, which leads to the attenuation spectrum for the given water sample as shown in Figure 5.7. In applied research it is common to use the attenuation as a representation of the absorption properties of a given water sample.

The extinction of a water sample at $\lambda = 860 \text{ nm}$ is considered to be a measure for turbidity, which is mainly caused by particulate material (DIN EN ISO 7027, 2000). The pigments of phytoplankton and other organic material do not absorb light of wavelengths larger than $\lambda > 700 \text{ nm}$. Therefore, they do not influence this turbidity value.

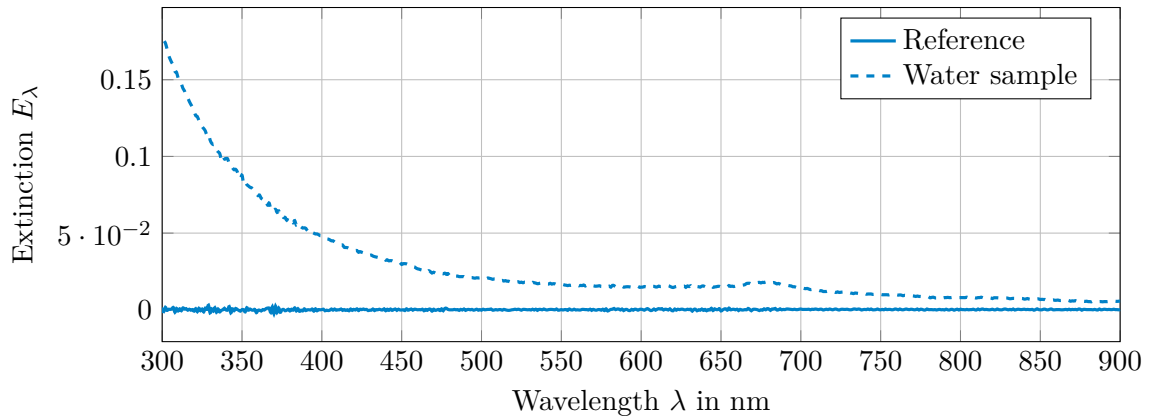


Figure 5.7.: Absorption or attenuation spectrum of a water samples.

The difference between the extinctions at e.g. $\lambda = 360 \text{ nm}$ and $\lambda = 860 \text{ nm}$ correlates with the yellow matter content, which is mainly formed by dissolved organic matter (e.g. humic substances). From a chemical perspective, in particular conjugated double bonds absorb best in ring systems with p-electrons, such as phenol groups and heterocycles (Chapman, 1996). This absorption in the near UV is therefore also called chromophoric dissolved organic matter (CDOM).

Both parameters, turbidity and chromophoric dissolved organic matter, can be measured quickly, automatically and cost-effectively. Therefore, both parameters are used as target values for the sensor system to be developed within the scope of this thesis.

6. In-situ Determination of Optical Properties

By knowing the optical characteristics of water and its dilutes and particles, optical in-situ measurements of the transmittance, respectively attenuation, at particular wavelengths can be used to derive information about water quality directly in the field. With respect to the peak wavelength being used for transmittance (absorption) determination, optical laboratory and in-situ sensor systems are based on similar analytic methods. For the determination of CDOM and turbidity, two wavelength areas are of particular interest. To this end, measurements in the UV and IR range of the electromagnetic spectrum are taken into account in particular as shown in Figure 6.1.

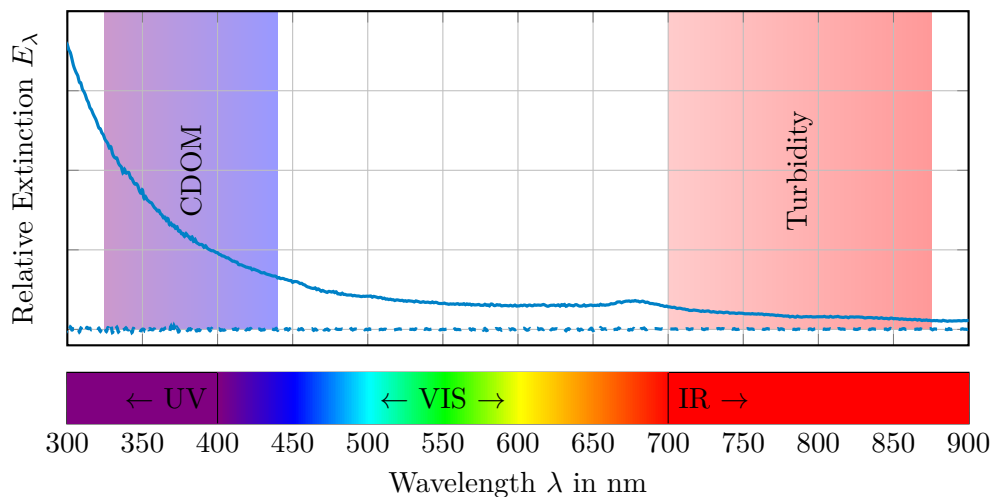


Figure 6.1.: Absorption spectrum of a given water sample and areas of interest for optical water quality assessment based on a literature review (see Table 6.1).

As can be seen in Figure 6.1, there are no narrow absorption bands within the extinction spectrum of a natural aqueous sample but larger absorption regions over an entire wavelength range. A literature review reveals that different wavelengths and wavelength ranges are used to optically determine turbidity and the content of CDOM. The colored areas in Figure 6.1 represent the wavelength being used in applied research.

Especially for CDOM, there is no uniform definition at which peak wavelength the measurement has to be carried out. One reason for this is that substances summarized as DOM or CDOM comprise a large number of molecular structures that lead to the formation of several absorption bands over a very wide spectral range, as illustrated in Figure 6.1. For this reason, a literature review reveals different information on the wavelength at which the spectral attenuation is correlated with the content of CDOM ranging from

$\lambda \approx 325 \text{ nm}$ to $\lambda \approx 440 \text{ nm}$. Table 6.1 provides an overview of the wavelength used for CDOM estimation and the corresponding references. Turbidity as a measure of the decrease in the transparency of an aqueous media due to undissolved particulate matter is measured in the near IR range. The wavelengths used for attenuation measurement due to turbidity range from $\lambda \approx 700 \text{ nm}$ to $\lambda \approx 870 \text{ nm}$. In contrast to the optical determination of CDOM, there is a specification for the measurement of turbidity, which is regulated in DIN EN ISO 7027 (2000).

Table 6.1.: Literature review on wavelengths used for in-situ CDOM and turbidity determination.

Wavelengths used for CDOM measurements (attenuation)	
λ in nm	Reference
325	D'Sa and Kim (2017)
337	Green and Blough (1994)
350	Meler et al. (2016); Nelson and Siegel (2002); Kirk (1994)
355	Green and Blough (1994)
370	Niu et al. (2014); Röttgers and Doerffer (2007)
375	Meler et al. (2016)
400	Meler et al. (2016); Miller et al. (2002)
412	Joshi et al. (2017); Johannessen et al. (2003)
442	Röttgers and Doerffer (2007)
443	D'Sa and Kim (2017); Kheireddine et al. (2018); Hoge et al. (1995)
440	Das et al. (2017)
Wavelengths used for turbidity measurements (attenuation)	
λ in nm	Reference
700	D'Sa and Kim (2017); Green and Blough (1994)
750	Green and Blough (1994)
860	DIN EN ISO 7027 (2000)
870	Hussain et al. (2016)

6.1. In-situ Measurement of Optical Properties

Compared to laboratory analytical methods, in-situ sensors offer the great advantage that they can directly measure in the medium (in-situ) and provide the measured value very fast. But there are some peculiarities to consider when using in-situ methods. First, it is important to mention that a distinction is made between scattered light and transmitted light measurement, e.g. for turbidity and CDOM estimation. For the present work,

though, only transmitted light measurement is of importance as this technique is normally used inside an attenuometer in the field or inside a laboratory photometer.

The underlying measurement setup is rather simple. An emitter generates electromagnetic radiation of a certain wavelength, which then penetrates an aqueous medium and hits a detector on the opposite side. While for laboratory applications cuvettes filled with the water sample are placed between emitter and detector, in-situ sensors have opposing optical windows. The space in between is in exchange with the surrounding water column. This optical path then forms the measuring path for determining the transmission or rather attenuation of the water and its ingredients. A schematic drawing is given in Figure 6.2.

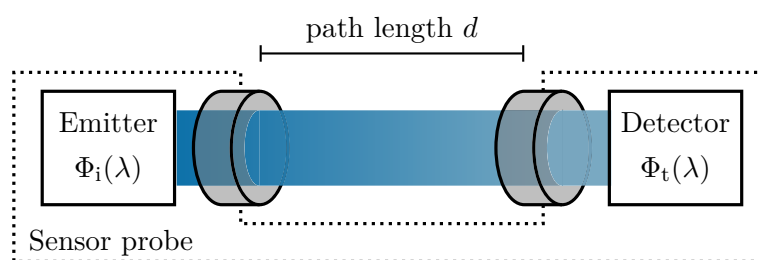


Figure 6.2.: Principle of an in-situ transmission sensor probe (attenuometer).

6.2. Limitations of Optical In-situ Measurement

In-situ sensors are exposed to harsh environmental conditions resulting in limitations for the later application. The main limiting factors are briefly explained below.

Environmental Impacts In addition to changing temperature conditions, high pressure loads and varying salinity pose major challenges for the successful use of in-situ measurement technology. When optical measurement technology is used, these changing environmental conditions have an influence on the optical density of the aqueous medium and thus on the measurement itself. Strong currents, sediment loads or varying ambient light can also influence the quality of the measurement.

Bio Fouling A significant limitation for the use of optical in-situ measurement technology is biofouling which is the undesired deposition of substances or organisms from the water phase on surfaces.

Optical Path Length According to the Beer-Lambert Law, the attenuation is directly proportional to the optical path length as shown in Section 5.4. A change in the path length will result in a change in the measured signal. Since the extinction E_λ is an exponential function, changing the path length can lead to a change in the measurement resolution.

Emitter Characteristics With regard to the measurement quality, optoelectronic properties of the emitter are also important. According to the Beer-Lambert Law, a

low incident radiant power $\Phi_i(\lambda)$ leads to a low transmitted radiant power $\Phi_t(\lambda)$ independent of how much is absorbed in the medium.

Detector Characteristics The detector is another critical unit, since the sensitivity (respectively $\Phi_t(\lambda)$) and spectral resolution (wavelengths) have a decisive influence on the quality of how the corresponding measured value can be determined.

6.3. Optical In-situ Sensors for Water Quality Assessment

Optical sensor technology for aquatic media includes a wide range of instruments and methods that are used to measure the relevant parameters for condition recording, reporting and monitoring. Besides singular components also complex systems such as in-situ sensors, surface measuring systems, underwater stations or remote-controlled underwater vehicles and drift bodies are used (Zerr et al., 2016; Moore et al., 2009). The broad perspective of this section does not allow to fully describe all sensors that are used or might be potentially useful for applications in the field of aquatic monitoring. Nevertheless, a brief review helps to identify the advantages and drawbacks of current systems and the possibilities for the future. Since most of the commercially available in-situ sensors for turbidity and dissolved organic matter detection are based on fluorescence measurements and not transmittance, only a few systems are more wide-spread in use in applied research or industrial applications. Table A.1 in the Appendix gives an overview of common sensor systems and their basic specifications.

6.4. Demands for Aquatic Monitoring in Research

Today, the monitoring of fresh water ecosystems, coastal waters and oceans is changing due to automatically operating sensor and data transmission systems that can quickly provide information about acute environmental changes. Improved hardware and software systems are now enabling advanced possibilities to control, configure and use measuring systems more wide-spread and autonomously. Unfortunately, service-oriented systems, which can be easily modified to meet case or user specific demands are only rarely available and not yet established in applied research (Zerr et al., 2016; Murphy et al., 2015b). Engineering research in this area concentrates on the development of adaptive sensor technology as well as the design, development and construction of autonomous systems capable of measuring water parameters and constituents without being limited by scale or system boundaries. Here, findings from other research areas such as electronics and informatics are playing a key role (Isoyama et al., 2017; Kang et al., 2017; Murphy et al., 2015a; Zhuiykov, 2012). Research questions and demands on future measurement systems will refer to autonomous sensors and the creation of interfaces in order to be able to transfer sensor data into service-oriented information systems for decision making and management.

Part IV.

System Development

7. Preliminary Consideration

The harsh environmental conditions expected in practical use pose major engineering challenges regarding the development of the proposed sensor probe since varying temperature and pressure loads, mechanical shocks and rough handling can have a significant influence on the measurement quality. To this end, a complex system design was established, which will be described within the following chapter.

7.1. Application Requirements

The design of an appropriate sensor for modern environmental monitoring applications should consider a rough handling during practical use as well as the need for usable interfaces and sophisticated, service-oriented hardware as a minimum standard. In most cases, monitoring tasks and applications are limited in terms of the available equipment, time and expenditures, which makes it difficult to establish a holistic monitoring approach. Another disadvantage is caused by the fact that commercial systems allow only minor adjustments by the user. This means that users have to find cumbersome workarounds in order to meet the specific measurement requirements. As mentioned in Section 1.4 of the introduction, the fundamental requirements for the proposed sensor probe can be summarized as follows:

Optical probe for CDOM and turbidity measurement A fast deployable and easy to use sensor probe is needed to derive spatio-temporal in-situ data close to real time. In order to achieve an appropriate accuracy and repeatability for the detection of turbidity and the amount of chromophoric dissolved organic matter, an optical measurement set-up must be found in the range as mentioned in Section 6 (see Figure 6.1). For this reason, the specification is made to measure the attenuation (transmittance) for CDOM approximation at peak wavelength of $\lambda_{\text{Peak}} = 370 \text{ nm}$ and turbidity at a peak wavelength of $\lambda_{\text{Peak}} = 850 \text{ nm}$ (Röttgers and Doerffer, 2007).

Modular system architecture The internal hardware of the sensor probe consist of several functional parts separated by specific tasks, e.g. a communication unit, emitter unit, detector unit and pressure/temperature unit. For this reason, an internal bus is needed for interfacing each module. For a simplified assembly, each module has the same geometric dimensions. Later, the single modules can be stacked on top of each other and integrated into the sensor housing.

Small sized, light-weight sensor probe The size of the sensor probe is a crucial aspect, as installation in the field or integration in instrument carrier systems depends on it. Moreover, a small sized and light-weight sensor probe reduces the methodological effort during field measurements and allows applications in shallow waters as well as in coastal or marine areas enabling scale-overlapping monitoring approaches.

Pressure tolerant sensor probe Pressure tolerant systems (PTS) consist of pressure-stable, electronic components or entire assemblies cast with incompressible, electrically non-conductive elastomers or other grouting. This ensures that the cast components are embedded in the grouting leading to pressure-, water- and corrosion-resistant systems of small size and low weight.

Integrated services To allow a service-oriented software customization of the hardware, only components were used which can be digitally addressed and configured. This also enables the opportunity for an assisted sensor configuration and calibration. Hence, changes in system behavior and data acquisition can be achieved by software commands leading to an adaptive sensor system.

Often mentioned limitations of existing sensors and sensor systems are the low interoperability and high purchase costs. In addition, many sensor systems have large dimensions and a high specific weight of several kilograms (see Table A.1), which can be challenging for the field application. Besides this, most commercially available systems are pre-configured by the manufacturers and do not provide sufficient services for the user to easily modify and use the sensor during field measurements in an appropriate manner (Waldmann et al., 2010). Therefore, a service-oriented sensor architecture forms the basic design rule for the development of the sensor probe. During the design phase, the system development was first focused on the hardware implementation of the underlying measurement principles and later continued with an appropriate integration into a practicable sensor probe prototype. As a consequence, the sensor prototype presented in this thesis allows a multitude of different operating modes, which can be configured by software commands.

7.2. Sensing as a Service – Towards a Service-oriented System Architecture

As mentioned before, a major goal of this work is to present a fast and service-oriented method for in-situ turbidity and CDOM monitoring. Therefore, an easy deployable and simple to use sensor probe for field application was developed. The conceptional framework of the design and development process is called *sensing as a service*. It was used as an underlying design rule leading to functional assemblies and elements that represent enclosed subsystems. The individual modules can thus be regarded as independently functioning groups according to their task or purpose. This also ensures that the functional

parts can be rearranged and changed during the assembly leading to a modular system design.

7.2.1. Communication Protocols and Interfaces

In order to ensure a service-oriented architecture, special emphasis was laid on the definition of appropriate interfaces and protocols. On the PCB and circuit level, the so called inter-integrated circuit standard I²C is being used. I²C has established in recent years as a very common communication protocol to interface peripheral devices with a micro controller. It is designed as a master-slave bus and works with a four wire connection (vcc, SDA, SCL, GND) using an address space of 7 bits, which allows up to 112 nodes such as temperature or pressure sensors on a single bus by specification (see Figure 7.1).

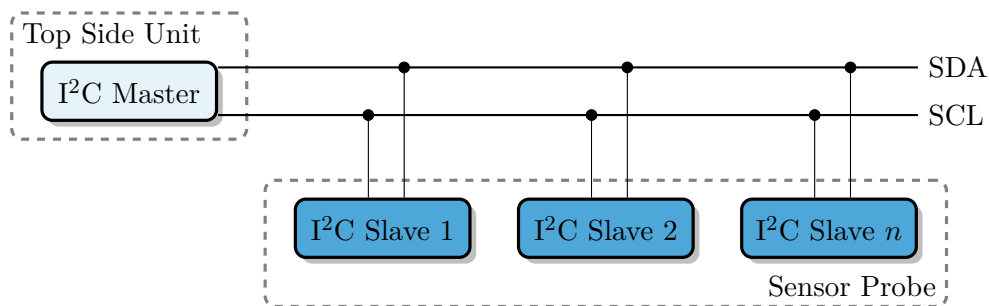


Figure 7.1.: Schematic drawing of the I²C bus.

7.2.2. Electronic Parts and Printed Circuit Boards

In addition to optical properties regarding the basic measurement principle, aspects such as component size, pressure sensitivity or software protocols and interfaces, e.g. I²C support, were important criteria for the selection of electronic components. The printed circuit boards were designed in order to accommodate the optoelectronic and electronic components in the smallest possible installation space. Moreover, separate circuit boards were designed according to each functional subgroup of the sensor probe leading to modular subsystems. The circuit boards were developed using the software Autodesk EAGLE¹. Starting from development of a schematic circuit, the final (physical) printed circuit board layouts can be designed, routed and finally produced with low expenditure of time and with a quality comparable to industrial products.

7.2.3. 3D Printed Parts for Applied Research

Rapid prototyping and additive manufacturing processes such as 3D printing have accelerated the development processes and innovation cycles of prototype system developments. For the development of the sensor probe presented in this thesis, a FFF 3D printer² was

¹ Autodesk EAGLE, version 9.0.1, Autodesk, Inc., USA

² Raise 3D N2 Plus Dual Extruder, Raise3D, Inc., USA

used for the production of the sensor housing and other parts. The printer specification is given in Table A.5 in the Appendix. By using different 3D printing filament material, a variety of component properties of the printed parts can be achieved.

7.2.4. Pressure Tolerant Hardware Design for Underwater Systems

Pressure tolerant systems (PTS) for electronic assemblies have been researched for several decades. Especially for marine and aquatic monitoring applications, various investigations and projects addressing this technological approach can be found (Christ and Wernli, 2014; Kampmann et al., 2012; McBride and Scholfield, 2007; Thiede et al., 2009; Barnes and Gennari, 1976). PTS represent an approach to accommodate electronic components in a small space, with low weight gain and low cost. PTS can be described as systems that can withstand an increased external pressure $p \geq 1$ bar without the need for pressure hulls. In the field of ocean engineering, several procedures for the production of PTS have been established. According to Kampmann et al. (2012), PTS are divided into two main groups, the fluid compensated pressure tolerant systems (FPTS) and the casted pressure tolerant systems (CPTS). Regarding FPTS, the electronic modules are installed in a housing with at least one deformable outer wall or an additional pressure compensator. The container is filled with an inert and electrically non-conductive liquid without leaving any gas inclusions. Here, the liquid should have a similar or lower compressibility than water. Substances used for FPTS are above all inert oils. Using casted pressure tolerant systems CPTS, the electronic assemblies are embedded in a solid material with the aid of a potting mold. The cast or encapsulation material completely encloses the assembly without leaving any gas inclusions. For the processing of the encapsulation, two-component plastics are particularly suitable for this purpose. The cast materials are commonly differentiated according to their Shore hardness. Epoxy resins and polyurethane (PUR) are among others most frequently used in CPTS. These potting materials can also absorb other mechanical loads and thus make the CPTS more resistant. In addition, it is possible to integrate the cast into existing structures for materials with a high Shore hardness. However, trapped gas bubbles under high external pressures destabilize the encapsulation, which can lead to cracks and ultimately to the destruction of the CPTS. Especially for plastics based on epoxy resins, strong internal stresses can arise due to shrinkage of the material while curing. These internal stresses must be counteracted with suitable precautions during the cast process in order to reduce the loads on the electronic modules.

Low Shore hardness can be achieved with silicone material, wax or related plastics. With these encapsulation materials, the ambient pressure is evenly transferred to the components. Another advantage of the soft casting materials is the reversibility and self-healing of the cast since damaged parts of the cast close automatically under renewed pressure load.

8. Development of an Adaptive Sensor Probe

In addition to the requirement to develop an adaptive and service-oriented sensor system, it is also important to accommodate the required functionalities in the smallest possible space to ensure a practicable design for the field application. Based on the considerations described above, an optical sensor probe was developed. The underlying engineering scientific considerations and findings will be described in detail in the following.

8.1. A Sensor Probe Made of Sensors

The sensor probe represents a result of multitude particular and functional electronic units (modules) equipped with integrated circuit (IC) components. This approach allows automated measurements due to software available micro services provided by the IC's. A stable and service-oriented system performance was achieved in particular by dividing the sensor into functional elements. The development of the sensor probe was based on the OSE sampling theorem as mentioned in Section 4.1. In general, the system architecture of the sensor probe can be depicted as a modeling scheme to illustrate the essential functions of the individual modules as shown in Figure 8.1.

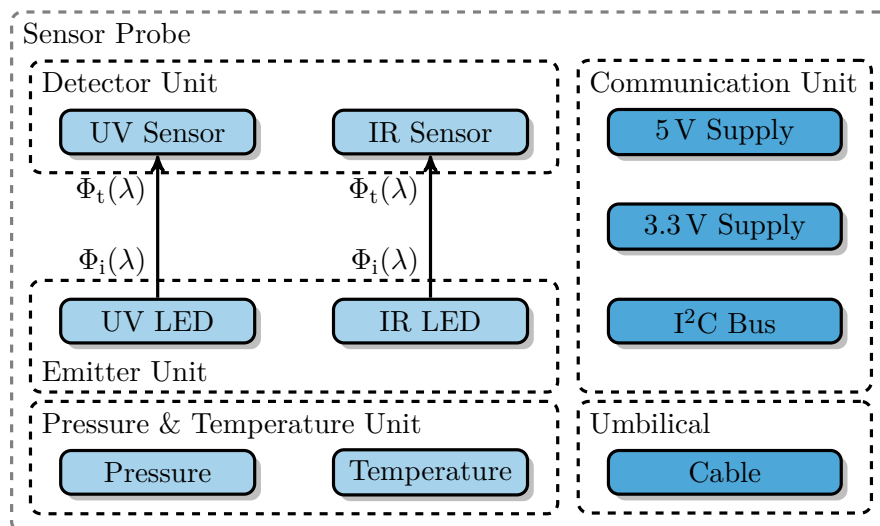


Figure 8.1.: Abstracted modeling scheme of the sensor probe.

8.2. Electronic Sensor Modules

Based on the underlying measuring principle (see Beer-Lambert Law in Section 5.4) and taking into account the requirements of the measuring task (OSE sampling theorem in Section 4.1), the development of the electronic assemblies was carried out according to a service-oriented architecture (see Figure 8.1).

8.2.1. Communication Unit

Interference-free signal transmission with low noise and signal degradation over longer cable lengths represents an engineering challenge, especially for sensor systems in the field of marine technology. The challenge is to avoid data loss and to find a communication protocol that works efficiently and without major time delays. Since the developed sensor is to be integrated into a system based on a microcontroller, the choice of an appropriate communication protocol is limited in terms of complexity and resource availability. For communication between a microcontroller and peripheral integrated circuits (IC's), the I²C protocol mentioned in Section 7.2.1 represents a fast and simple solution. But I²C is not specified for longer distance or cable communication. To overcome this limitation, an I²C buffer IC (P82B96¹) is used to create a bidirectional and logic interface between the mentioned I²C-bus and a bus configuration capable enough to allow long distance communication up to 250 m cable length. The communication board also serves to regulate the 12 V supply voltage coming from the topside unit to 3.3 V and 5 V on the sensor level. The communication unit required the largest number of electronic components and installation space (see schematic A.1 in the Appendix). For this reason, the board dimensions and footprint as shown in Figure 8.2 were adopted for the following units.

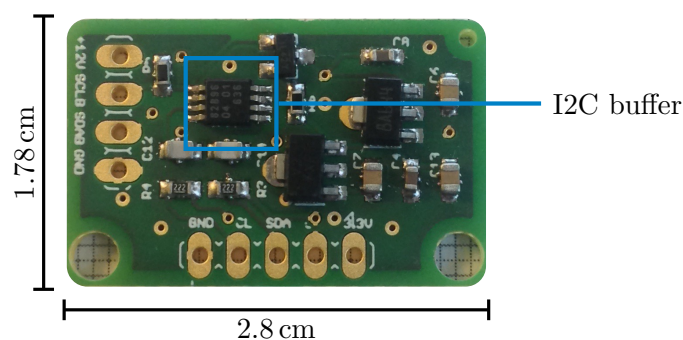


Figure 8.2.: Assembled communication unit (PCB). The contacts for the cable connection to the topside unit (12 V, SCLB, SDAB, GND) are located at the left hand side of the board, whereas the contacts for the stack assembly of the electronic sensor modules (from board to board) are located on the bottom side (GND, SCL, SDA, 5 V, 3.3 V).

¹ P82B96, Dual bidirectional bus buffer, NXP N.V., Netherlands.

8.2.2. Emitter Unit

The emitter board accommodates the light sources with the corresponding excitation wavelengths as defined earlier in Section 7.1 for turbidity measurement (IR LED² with a peak wavelength of $\lambda_{\text{Peak}} = 850 \text{ nm}$) and CDOM determination (UV LED³ with a peak wavelength of $\lambda_{\text{Peak}} = 370 \text{ nm}$). Originally, the LP55231⁴ is designed as a 9-channel LED driver for generating light effects for mobile devices. The LED driver circuit allows to change the settings for the operation of the LED's such as the adjustment of a constant forward current in the range of $I_{\text{LED}} = 0 \text{ mA} \dots 25.5 \text{ mA}$ or to do a pulse width modulation (PWM) from 0%...100% duty cycle. A highly efficient charging pump enables LED operation over a large voltage range ($\pm 0.3 \text{ V}$ to power supply voltage, here 3.3 V). It is also possible to monitor characteristic performance parameters, e.g. the voltage drop U_{LED} over an LED, during operation by software commands via I²C interface. Another advantage of the LED driver IC is the internal temperature measurement, which allows to monitor the board temperature ϑ_{PCB} as an important process variable during the measurement. The final PCB design of the electronic module is shown in Figure 8.3.

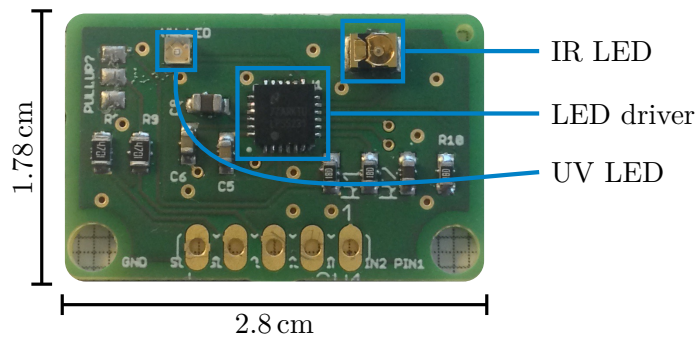


Figure 8.3.: Assembled emitter unit (PCB) with UV LED, IR LED and LED driver IC.

The associated circuit to the emitter unit is given in Figure A.2 in the Appendix. For the future sensor system, the emitting unit provides several functions at the same time. Thanks to the possibility of setting a constant forward current I_{LED} , the intensity of the emitted light can be adjusted. If the operating point is set by the constant current adjustment, pulse width modulation can be used to vary the luminous flux from 0%...100%. This enables very dynamic control of the LED's and ensures constant light emission characteristics, which is important for repeatable measurements. Thanks to the internal temperature measurement, it is also possible to identify any dependencies or to carry out an immediate temperature compensation. In Chapter 13 this issue is discussed in more detail and examined by experimental investigation as well as the evaluation of the optoelectronic properties.

² SFH 4651, high power IR LED, OSRAM Opto Semiconductors GmbH, Germany

³ VLMU1610-365-135, mid power UV LED, Vishay Intertechnology, Inc., USA

⁴ LP55231, 9-channel LED driver, Texas Instruments Inc., USA

8.2.3. Detector Unit

The detector unit consists of two light-to-digital converter elements (light sensors), which are sensitive in the UV⁵ and VIS-NIR⁶ range according to the emission spectra of the used LED's and the measurement requirement analysis (see Section 7.1). Both integrated circuits are accessible via I²C interface and provide integrated micro services. Each light sensor incorporates a photodiode, amplifiers and analog-to-digital circuits into a single chip. This allows the adjustment of the integration time of the light sensors via software commands and therefore a change in the detector intensity. An increase in the integration time has the effect that even a low transmitted light intensity can be detected. The schematic is given in Figure A.3 in the Appendix.

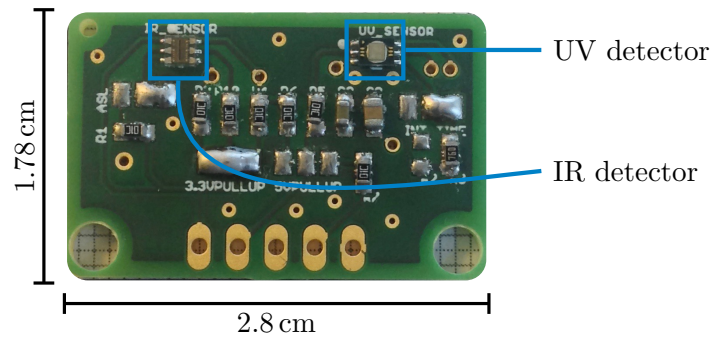


Figure 8.4.: Assembled detector unit (PCB) with UV and IR light sensor.

8.2.4. Pressure and Temperature Unit

The pressure and temperature unit is important to place the sensor readings in the correct context according to the OSE sampling theorem. For this purpose an I²C accessible pressure sensor⁷ is used to measure the ambient pressure up to 14 bar and water temperature with 24 bit resolution (± 0.2 mbar, < 0.01 °C). The assembled pressure board can be seen in Figure 8.5 below. The schematic is given in Figure A.4 in the Appendix.

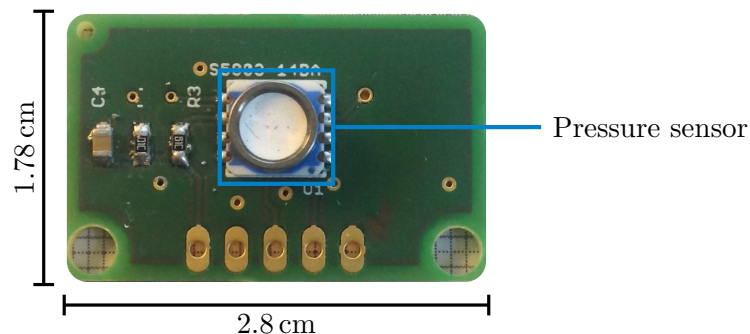


Figure 8.5.: Assembled pressure and temperature unit (PCB).

⁵ VEML6070, UV light sensor, Vishay Intertechnology, Inc., USA

⁶ TSL2561, VIS-NIR light, sensor, Texas Advanced Optoelectronic Solutions Inc., USA

⁷ MS5803-14BA, Measurement Specialties, Inc., TE Connectivity Ltd., USA

8.3. Enclosure Components and Peripherals

Basically, a suitable sensor enclosure provides mechanical protection against external influences and ensures safe installation of the electronics inside. Therefore, the design of the housing depends on the practical use. Sensor weight, size, the form factor and the possibility of a quick and easy assembly in the field are essential quality features, apart from the measurement quality of the sensor. The sensor probe presented within this thesis was developed with the aim of being as small as possible and reduced to the essentials.

8.3.1. 3D-printed Enclosure Components

The whole housing of the sensor probe is made of 3D-printed parts. The advantage of this manufacturing process can be found in the very short time span between the designing and the making of a functional prototype. Innovative filament materials also make it possible to produce mechanically resilient or optically transparent parts.

Sensor Probe Housing

The sensor housing was printed using black PETG filament⁸ (Z-PETG). The thermoplastic material is based on modified polyethylene terephthalate glycol (PETG), which makes it highly resistant to chemicals such as salts, acids, alkalis, and solvents. The filament withstands UV light and is also resistant to oils and greasy substances, which makes it a suitable material for the prototype sensor housing. Due to the precise 3D printing, the individual components could be manufactured very precisely. The component thickness of the hull is therefore only 1.2 mm.

Optical Window

Regarding optical sensor system development, one of the greatest challenges is to ensure an appropriate optical pathway that represents the measurement path (see Section 6). In a transmission measurement or attenuation measurement, this path generally consists of two opposite optical windows and the aquatic media in between. In conventional systems, optical windows are made of glass or quartz glass. Plastics cannot be used for deep UV applications below $\lambda < 320$ nm, as absorption effects by the material itself can occur. For the manufacturing of the optical window of the presented sensor probe a translucent filament⁹ is used (Z-Glass). The material is resistant to scratches, UV light and chemicals and guarantees accurate 3D printed models with low shrinkage. The optical windows are very thin, so that the layer thickness of the printed material is only 0.4 mm.

⁸ Z-PETG Filament, Zortrax S.A., Poland

⁹ Z-Glass, Zortrax S.A., Olsztyn, Poland

8.3.2. Cast

In order to obtain a pressure tolerant system, the electronic components were encapsulated as described in Section 7.2.4. The particular challenge is to find a cast material that bonds well with the circuit boards, electronic components and the cable insulation material. In addition, the cast material must be resistant to seawater and optically clear to not interfere with the measurement. To this end, transparent polyurethane resin¹⁰ is a recommended and suitable material for casting optical components. The resin has a water white transparency, which makes it ideal for the intended application. Moreover, it is resistant to UV radiation, acids and alkalis as well as water and organic growth.

8.3.3. Cable and Connectors

For power supply and data transmission, a shielded cable¹¹ is used. The cable specification can be found in Table A.3 in the Appendix. When encapsulating the electronics, it must be ensured that there is a permanent and tight connection between the cable insulation material and the casting material. The cable jacket material is S-PVC, so the hardener of the PU based cast material can establish a stable and permanent bond. In addition to the choice of a cable, a connector to the topside unit is particularly important for an efficient field application and comfortable handling. It is necessary to not only ensure that signals are transmitted without loss, but also to provide sufficient protection against weather conditions and moisture penetration. The used connector¹² is IP67 rated and therefore classified to be dust tight and protected against contact. It is also ensured that no water will penetrate unless the connector is not submerged deeper than 1 m and longer than 30 min.

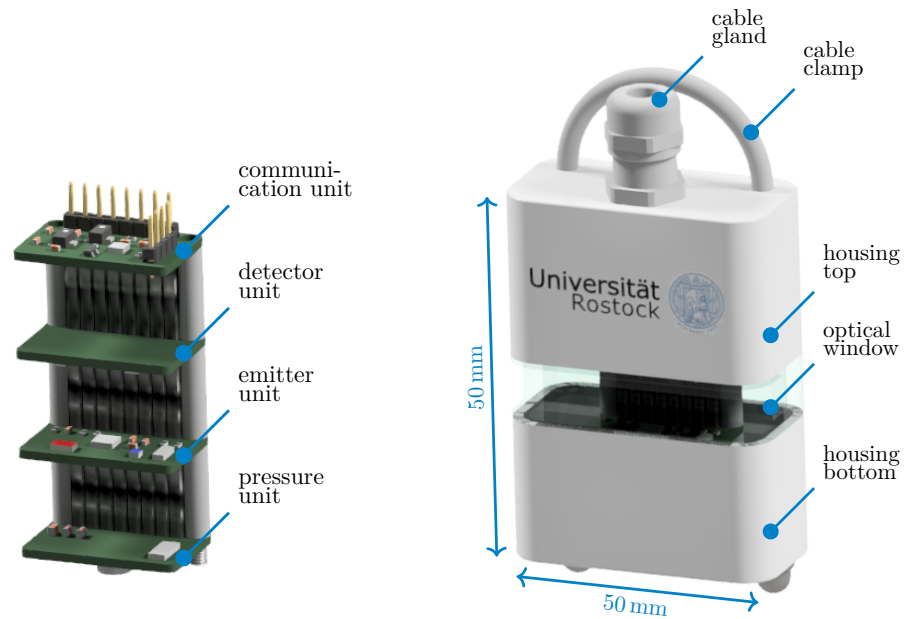
8.4. Full Assembly of Optical Sensor Probe

Based on the modular system architecture and the task-oriented development of the sub-modules, all components can be assembled into an interlocking overall sensor probe design. The result is a miniaturized, modularized and thus standardized sensor probe, which also provides an interface via the selected I²C protocol. This allows later adaptations and configurations of the sensing properties and system behavior by software commands without the need to make physical changes on the sensor level. Figure 8.6 shows both the stacked electronic submodules and the fully assembled sensor probe. For assembly the electronic modules are interconnected, cable connections soldered to the contacts and the resulting electronic skeleton is installed in the sensor housing before the interior is cast with translucent PU. The assembled sensor probe has dimensions of $50 \times 50 \times 35$ mm and a mass of about 120 g (without cable).

¹⁰ UR5634, Polyurethane Resin, Electrolube

¹¹ LifYDY, 4×0.1 mm², Miniature control cable, Kabeltronik Arthur Volland GmbH, Germany

¹² SAL8 RSC4, SAL M8x1, CONEC GmbH, Germany



(a) Stacked electronic circuit boards, which are casted in transparent PU inside the probe. (b) Fully assembled sensor probe with printed enclosure and printed optical window.

Figure 8.6.: Fully assembled sensor probe (3D printed) and inside view of the stacked electronic units.

Figure 8.7 shows the sensor probe installed at the artificial reef of Nienhagen in the Baltic Sea (Rostock, Germany) at a water depth of 11 m during a field test in 2018. Due to the cable clamps integrated into the sensor housing, installation in the field is easy and fast. The strain relief and cable gland avoid excessive tensile forces acting on the cable.



Figure 8.7.: Sensor probe installed in a water depth of 11 m during a measurement at the artificial reef of Nienhagen, Baltic Sea, Germany (54.174790, 11.943515).

9. Development of a Service-Oriented Sensor System

In addition to the development of a sensor probe, the process and system integration as well as the provision of a user environment represent an essential component in the implementation of a holistic monitoring method. In this context, the OSE sampling theorem as mentioned in Section 4.1 once again forms the basis of the development. Therefore, the service-oriented architecture of the sensor system will be described in the following.

9.1. System Architecture

As shown in Figure 9.1, the system architecture follows the requirements formulated in Section 7.1 with regard to the choice of components. One of the most important components is the microcontroller. It provides the interfaces connecting the sensor system to the peripherals. These include the GPS for position determination, the SD card unit for data storage as well as the communication unit for data transfer via Bluetooth or WiFi. In addition, a stable voltage supply is guaranteed by appropriate voltage regulators. This offers the possibility to operate the system either via a 5 V standard USB interface or via a voltage source between 12 V ... 35 V direct current.

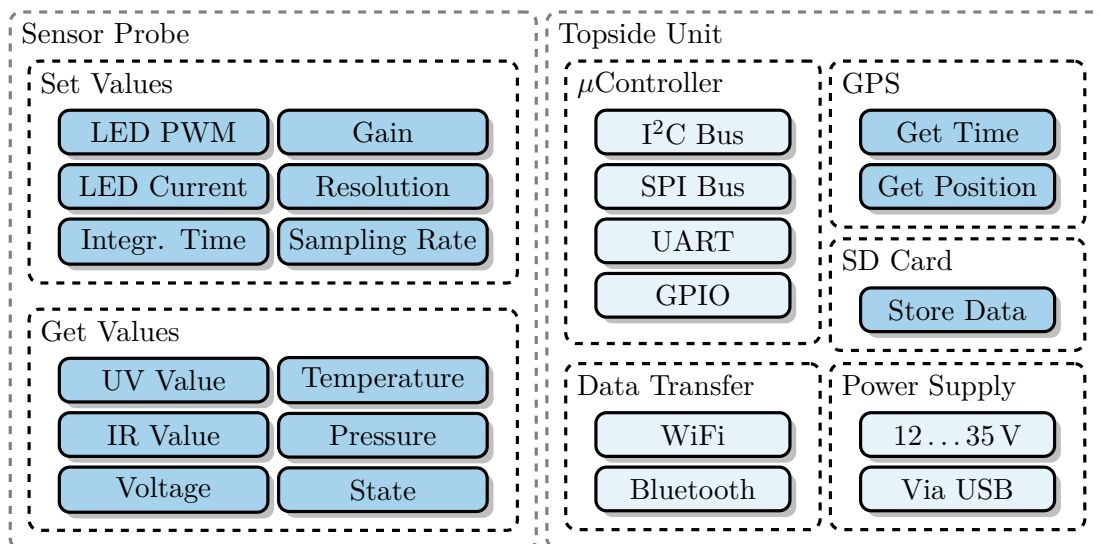


Figure 9.1.: Schematic drawing of the hardware architecture of the sensor system consisting of the Sensor Probe and the Topside Unit.

9.1.1. Top Side Unit

The components used in the topside unit and their significance for the overall functionality of the sensor system are briefly explained below.

Microcontroller

The microcontroller¹ is the central part of the measuring system. All peripherals are connected to the microcontroller via interfaces (I²C, UART, SPI). The entire program sequence, all routines and protocols are controlled and organized by the firmware running on the microcontroller. All sensor data are retrieved, bundled and processed with the help of the microcontroller and finally provided via a UART interface.

Controlling Unit

To ensure stable communication between the topside unit and the sensor probe and to provide a service-oriented power supply for the system, a circuit board was developed that can be simply plugged into the microcontroller as shown in Figure 9.2.

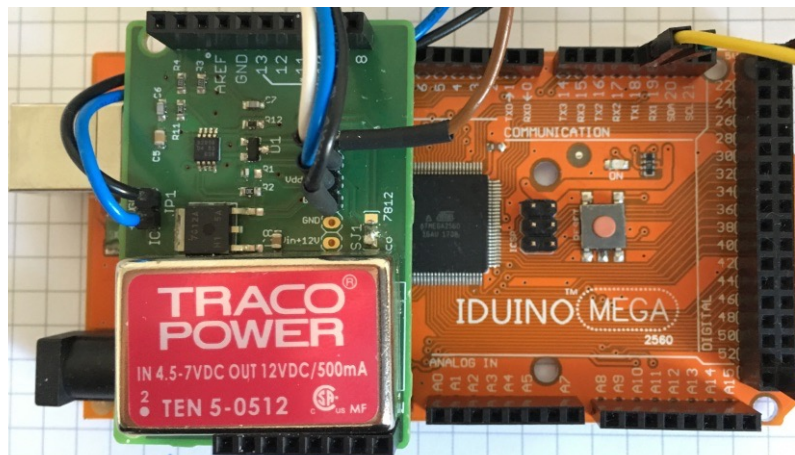


Figure 9.2.: Image of the top side unit plugged into the microcontroller.

The controlling unit is the counterpart to the communication unit of the sensor probe. Here the transmission signal is also modified in order to be able to use longer cable lengths via the I²C protocol without suffering signal loss (see Section 8.2.1).

GPS Module

With the GPS module² a geolocalization is carried out and also the system time synchronization is accomplished over the time system of the navigation satellites (GPS time). For the underlying OSE sampling theorem, the conditions of time and geolocalization are fulfilled.

¹ Mega2560 Board(ST1026), 4016139159881, Iduino

² NEO-6, u-blox 6 GPS Module, u-blox AG, Switzerland

Micro SD Card Memory Shield Module

For data storage a micro SD card module is used, which allows reading and writing data to micro SD cards via an SPI interface and corresponding file system drivers from the microcontroller system. The module is based on a chip³, which contains high speed CMOS logic hex non-inverting buffers.

WiFi and Bluetooth Communication

Data transmission and communication can take place via a Bluetooth or WiFi connection. The WiFi variant was preferred for the experiments, so that the sensor data could be sent directly to a server via a gateway for further processing, visualization and storage.

Housing

For the housing, a ready made enclosure⁴ was used. The enclosure is classified to be dust tight and provides a complete protection against contact. It is also ensured that no water penetrates the housing as long as the enclosure is not immersed deeper than 1 m and for more than 30 min (IP67 standard).

Connectors and Switches

For easy and safe use in the field, the topside unit has two connectors for power supply⁵ and data transmission⁶ to the sensor as well as a waterproof button⁷ to turn the system on and off. The switch-on button has an illuminated LED ring that lights up briefly as soon as a measurement is completed for user feedback.

9.2. Software Development

Within the software development, a program code (firmware) was evolved based on the used hardware. It can access the various services of the individual modules and integrated circuits and integrate them into a comprehensive sensor system providing a service-oriented, modular and therefore adaptive system functionality.

9.2.1. The Program Code

All system functions are called via the program code running on the microcontroller. The code is developed within the Arduino IDE programming environment and is based on a

³ CD74HC4050, Texas Instruments Inc., USA

⁴ TG ABS Enclosure, IP 67, 202 × 122 × 75 mm, 10100801, Spelsberg, Germany

⁵ SAL8 FK30, SAL M8x1, CONEC GmbH, Germany

⁶ SAL8 FK40, SAL M8x1, CONEC GmbH, Germany

⁷ Metal On/Off Switch, 482, Adafruit Industries, LLC, USA

sketch. Programming is done in the Arduino programming language which is similar to C or C++.

The complete source code is given in Listing A.1 in the Appendix. The source code contains more than 550 lines, therefore only aspects of essential importance will be explained here. The program code can be separated into two parts, an initialization part and a loop. Before initialization libraries are loaded which provide special functions by simple to use system calls, e.g. GPS queries. The respective authors are named in the source code. In this connection, the `I2C.h` library is of particular importance. The standard library implemented by default via the Arduino IDE has the disadvantage that in case of a defective I²C slave, the entire program stops working due to an endless loop. This is because no runtime check is implemented by default. The library used and referenced in the source code solves this problem, which is beneficial to system stability. Another important library is the `ArduinoJson.h` library. It allows to create a complete JSON string, which will be explained in detail in Section 9.2.2.

During initialization all interfaces and system constants are configured. Afterwards, the system enters the program routine (loop).

With each program cycle, a GPS query is made via a function call. In case a valid GPS signal is received, it is used to perform the geolocalization as well as to synchronize the system time with the GPS time. Regarding the OSE sampling theorem, the requirement for a location and time reference is therefore partially fulfilled. The requirement of the time synchronization of data acquisition is achieved by the fact that measurements are only carried out at certain, recurring times. In the present program example, this is the case every full minute and 30 seconds afterwards for every single sensor system, e.g. 12:05:00 and 12:05:30 UTC time. Finally, a closed measurement series is recorded via a single call as shown in Listing 9.1. All parameters that influence both the configuration of the emitters and the detectors are passed during the function call.

Listing 9.1: Function call to gather a closed measurement series

```
//createJSON(int I_IR, int I_UV, int PWM_IR, int PWM_UV, int LOG_EN_IR, int LOG_EN_UV, int GAIN_IR, int ITIME_IR, int ITIME_UV) {  
createJSON(255, 255, 255, 255, 0, 0, 0, 1, 2);
```

This function call leads to a collection of commands which configure the respective measurement conversions according to the passed parameters and finally read the results from the registers (see Listing A.1, lines 176 – 230). This allows a variety of settings to be made in order to adjust the measurement range or the resolution of each measurement. To illustrate how flexible the user is in the choice of parameters for measurement conversion, Table 9.1 contains all the variables, their options and the corresponding results due to the emitter and detector behavior for the UV and IR channel. This may be comfortable for software users, but the key advantage is that the system can be easily automated. With

a single function call, the entire system behavior can be adjusted and finally modulated. The emitter intensities can be automatically set and the integration time of the detectors can be gradually adapted.

Table 9.1.: Software commands, settings and ranges.

Variable	Setting	Result	Description
I_IR	0...255	$I_{LED} = 0 \text{ mA} \dots 25.5 \text{ mA}$	set forward current IR LED
I_UV	0...255	$I_{LED} = 0 \text{ mA} \dots 25.5 \text{ mA}$	set forward current UV LED
PWM_IR	0...255	$\Phi_i(\lambda) = 0\% \dots 100\%$	set intensity IR LED
PWM_UV	0...255	$\Phi_i(\lambda) = 0\% \dots 100\%$	set intensity UV LED
LOG_EN_IR	0...1	-	set logarithmic or linear dimming
LOG_EN_UV	0...1	-	set logarithmic or linear dimming
GAIN_IR	0, 1	gain: $1\times, 16\times$	set gain IR light sensor
ITIME_IR	0, 1, 2	13 ms, 101 ms, 402 ms	set integration time IR light sensor
ITIME_UV	0, 1, 2, 3	125 ms, 250 ms, 500 ms, 1000 ms	set integration time UV light sensor

9.2.2. Data Handling

A central component of every sensor and monitoring system besides the data acquisition is the data handling. For many commercially available systems, the manufacturer is defining the protocol that provides the sensor data and measurement results via a certain interface. This often results in a time-consuming and complex subsequent post-processing. Hence, a sufficient data format would be advantageous, which is easy for the user to understand and machine-readable for fast post-processing of the data.

For the development of web-based applications and the Internet of Things, a data format called JavaScript Object Notation (JSON) has become strongly established in recent years, which is suitable for becoming a future standard in environmental monitoring applications. JSON is a compact data format in an easily readable text form for exchanging data between applications. It is used to transfer and store structured data and serves as a data format for serialization. Especially for web applications and mobile apps it is often used in conjunction with JavaScript, Ajax or WebSockets to transfer data between the client and the server.

Disadvantages compared to the binary format can be found in the larger amount of data and the fact that a string has to be processed.

In Listing 9.2 an exemplary JSON string message is given to show the basic structure of the output as a result of a single measurement acquired by the sensor system. Since the data can be nested as required, an array of arbitrary objects is possible. An object is a set of "name":value pairs. Each "name" is followed by a colon followed by the value. Single "name":value pairs are separated by a comma.

Therefore, each measurement corresponds to a JSON object. The individual fields can also be used for an unique assignment. This refers both to the individual sensor system ("id") and to the time ("timeStamp"), the geolocalization ("latitude" and "longitude") or as in this case, the water depth via the attribute "pressure".

Since this applies to all sensor systems, the simultaneous use of several systems is possible. This enables the post-process to be easily implemented and scaled. As a result, this fulfills an essential requirement for the monitoring to be developed according to the OSE sampling theorem (see Section 4.1). The meta information contained in the JSON object is important for tracking the reliability of the measurement results and the system status of the measurement system.

Listing 9.2: JSON String format for data transmission of a single measurement.

```

{
  "id": "DOC0001",           //Sensor ID
  "timeStamp": "2018-04-05T06:13:10", //Time UTC format
  "latitude": 53.842163, //GPS position
  "longitude": 7.496899, //...
  "satellites": 6,         //n. of satellites
  "fixAge": 13552,        //age of GPS fix
  "gpsValid": true,       //gps available?
  "IR_VAL_CH0": 13337,    //VIS detector value
  "IR_VAL_CH1": 9176,     //IR detector value
  "IR_I_TIME": 1,         //Integration time setting (IR detector)
  "IR_GAIN": 0,           //Gain IR light sensor (IR detector)
  "IR_I": 125,            //forward current (IR LED)
  "IR_PWM": 125,          //set PWM value (IR LED)
  "IR_U": 70,             //forward voltage (IR LED)
  "UV_VAL": 163.00,       //UV detector value
  "UV_I_TIME": 3,         //Integration time setting (UV detector)
  "UV_I": 125,            //forward current (UV LED)
  "UV_PWM": 125,          //set PWM value (UV LED)
  "UV_U": 112,            //forward voltage (UV LED)
  "pressure": 10033,       //pressure=10033/10=1003.3 mbar
  "temperature": 1741,     //temperature =1741/100=17.41 degC
  "VDD_U": 158,           //e.g. Vdd=158x0.03-1.478=3.262V
  "Vout_U": 199,          //voltage of charging pump
  "PCB_temperature": 16  //temperature on PCB
},

```

Part V.

System Assessment

10. Materials and Methods

In preparation for the system evaluation, the tools and measuring instruments used are explained below. Subsequently, the test setups and experiments with which the later laboratory tests were carried out are described.

10.1. Measuring Devices

Digital Multimeter A digital multimeter¹ was used for voltage, current, resistance and electrical continuity measurements. Via the serial interface of the multimeter it is possible to carry out computer-aided automated measurements. Table A.6 in the Appendix lists the specifications, resolution and accuracy of the different measurement modes of the multimeter.

Spectrometer Two spectrometers for the UV/VIS range² and the VIS/NIR range³ were used to evaluate the spectral characteristics of the LED's installed in the sensor system. A collimator lens⁴, a curved optical lens, was used to paralyze the light that enters the spectrometer via an optical fiber patch cord⁵. See Table A.8 and A.9 in the Appendix for further information.

Photometer A laboratory UV/VIS spectral photometer⁶ with a reference beam path and exchangeable cuvetts was used for the laboratory analytical comparison measurements of the sensor system. Measurements can be done within a wavelength range of $\lambda = 190 \text{ nm} \dots 1100 \text{ nm}$ and a step width of 1 nm. Further specifications are given in Table A.7 in the Appendix.

Measuring Computer A notebook⁷ was used for automation and data recording during the experiments. MATLAB⁸ was used to communicate with the measuring devices (multimeter, spectrometer) and the sensor system via serial interfaces, to start measurement routines as well as to record, process and store the respective data.

¹ Voltcraft VC-830 DMM, Conrad Electronic SE, Germany

² USB 2000+ UV-VIS, $\lambda_{UV/VIS} = 174.86 \text{ nm} \dots 889.95 \text{ nm}$, Ocean Optics, Inc., USA

³ USB 2000+ VIS-NIR, $\lambda_{VIS/NIR} = 369.89 \text{ nm} \dots 1053.8 \text{ nm}$, Ocean Optics, Inc., USA

⁴ Collimating Lense, Ocean Optics, Inc., USA

⁵ P100-1-UV-VIS, Ocean Optics, Inc., USA

⁶ Cadas 200, HACH LANGE GMBH, Germany

⁷ MacBook Air, macOS High Sierra, 10.13.6 (17G65), 1,6 GHz Intel Core i5, 8 GB 1600 MHz DDR3, Apple Inc., USA

⁸ MATLAB, R2017a, 64-bit (maci64), The MathWorks Inc., USA

10.2. Experimental Test Setups

In order to investigate the properties of the developed sensor system, different experimental test setups were developed, which will be briefly explained in the following.

LED and LED Driver Test Setup

In the presented sensor system, the LP55231 LED driver IC controls the forward current I_{LED} of each LED. In addition, the voltage U_{LED} dropping via the LED, the supply voltage U_{DD} or the forward current I_{LED} can be measured. In order to use these internally measured values as a status monitoring during the field application, the reliability and accuracy of the LED driver internal analog to digital conversion are experimentally investigated by using a digital multimeter. Figure 10.1 shows an exemplary drawing for the IR LED test setup. The behavior of the UV LED was examined in the same manner.

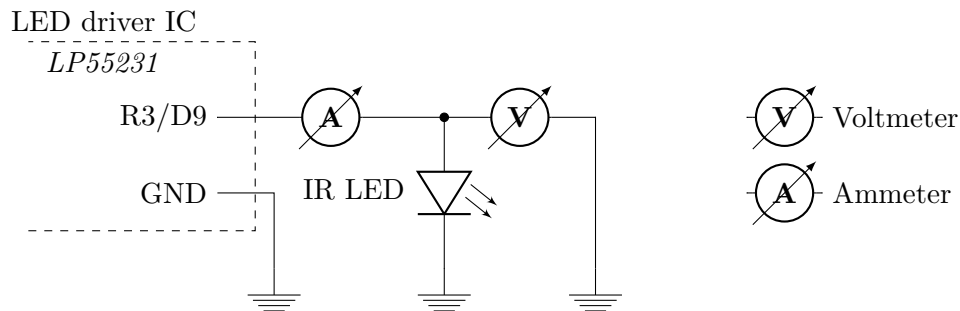


Figure 10.1.: Exemplary drawing of the LED driver (LP55231) test circuit.

LED Spectral Test Setup

For the experimental investigation of the emission spectra of the used LED's, a spectrometer was integrated into the test setup. Both the measurement system and the spectrometer were connected to a computer via a serial interface. With the help of a MATLAB script, the operating conditions of the LED were modified and the respective spectral characteristics recorded due to a changing I_{LED} or PWM signal.

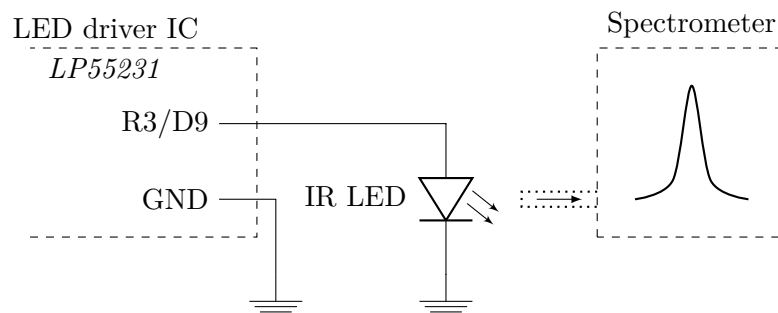


Figure 10.2.: Schematic drawing of the LED spectral test circuit using a spectrometer.

Pressure Dependence Test Setup

To examine the functionality of the sensor system under pressure load, pressure tank experiments were carried out. In this way it is to be examined whether a pressure dependence can be determined. Since the cable length for the prototype is limited to about 250 m due to the signal conditioning, pressure tests up to a pressure of about $p_{\max} \approx 40$ bar are reasonable. To conduct the pressure tank tests, it was necessary to implement a pressure-compensated connector in order to transmit the sensor signal through the tank jacket. The cover of the pressure tank is then closed, the tank is vented and manually pressurized using a manual pressure pump. The sensor probe has an internal pressure sensor. For the test, this was replaced by a sensor with a nominal pressure range up to 30 bar but can withstand pressure peaks up to 50 bar. Figure 10.3 shows a schematic drawing of the test setup.

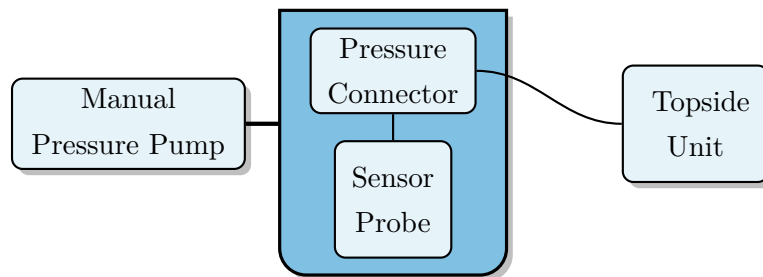


Figure 10.3.: Schematic drawing of pressure dependence test setup.

Temperature Dependence Test Setup

In order to investigate the temperature dependence of the sensor system, an experimental setup with a temperature-controlled water tank was realized in which the sensor probe was inserted. In this way, the temperature characteristics of the overall system were determined in a temperature range of about $8^{\circ}\text{C} \dots 25^{\circ}\text{C}$.

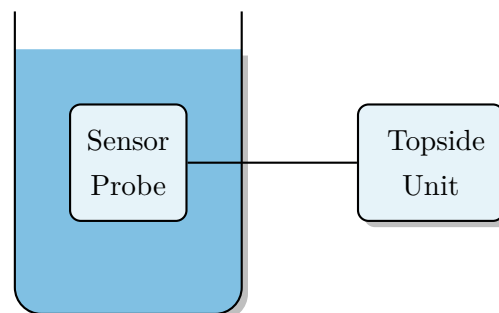


Figure 10.4.: Schematic drawing of the temperature dependence test setup.

11. Optoelectronic Characterization of Sensor Components

As the Beer-Lambert-Bouguer Law stated, the quality of the measurement is significantly influenced by the spectral properties of the emitter and the detector.

11.1. Electronic Characterization of the Emitter Unit

Before examining the spectral properties of the UV and IR LED, the stability and setting accuracy of the LED driver IC were examined. Since the LP55231 controls the forward current I_{LED} through the LED and also measures the voltage U_{LED} dropping via the LED, both the quality of the constant current setting and the measurement of the voltage drop were evaluated (see Figure 10.1). First, the forward voltage U_{LED} across the IR LED were measured with a digital multimeter (DMM) and compared to the values determined internally by the LP55231 LED driver IC. The outcomes of the comparison are shown below in Figure 11.1, where the multimeter measurements were plotted against the LED driver IC measurements. The linear regression analysis leads to a formal relationship of $y = 0.9277x + 0.1258$ with a determination of $R^2 = 0.9687$ and a linear correlation coefficient of $\rho_{X,Y} = 0.9842$. Considering the results, it becomes apparent that the measurement of the voltage U_{LED} using the digital multimeter is about 0.13 V larger than the internal voltage measurement.

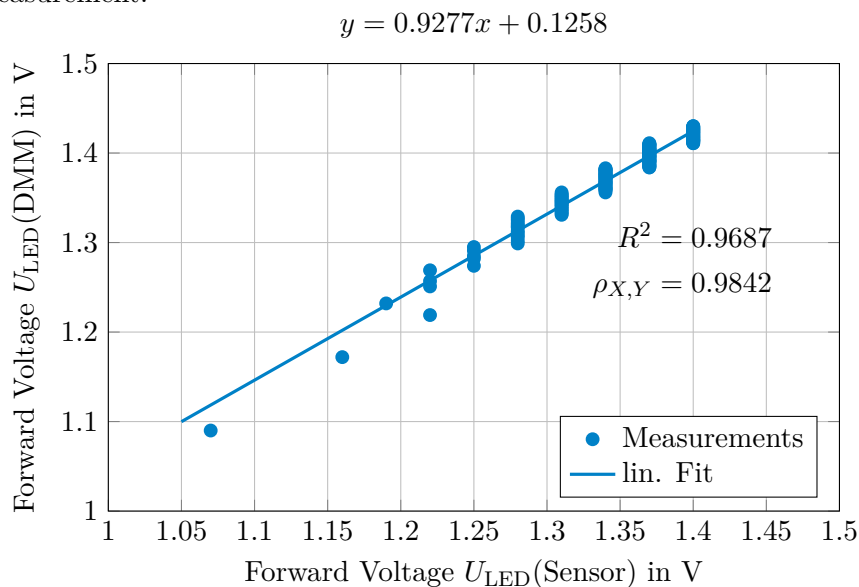


Figure 11.1.: Comparison of forward voltage U_{LED} of the IR LED measured by LED driver IC and external digital multimeter (DMM).

The quality of the internal constant current control was also investigated. Constant current control is particularly important for the operation of LED's, since the relationship between the forward current I_{LED} and forward voltage drop U_{LED} across an LED is exponential (see Figure 11.3). To this end, the forward current I_{LED} were measured using a digital multimeter and compared to the values set internally by the LP55231 LED driver IC (see circuit drawing in Figure 10.1). Figure 11.2 below contains the digital multimeter (DMM) readings of I_{LED} plotted against the LED driver IC measurements. The linear regression analysis of the data gives a formal relationship of $y = 1.001x + 0.0287$ with a determination of $R^2 = 0.9999$ and a linear correlation coefficient of $\rho_{X,Y} = 0.9999$. A comparison of the value pairs shows that there are no major deviations between the forward current set with LP55231 LED driver IC and the forward current I_{LED} measured externally (± 0.03 mA).

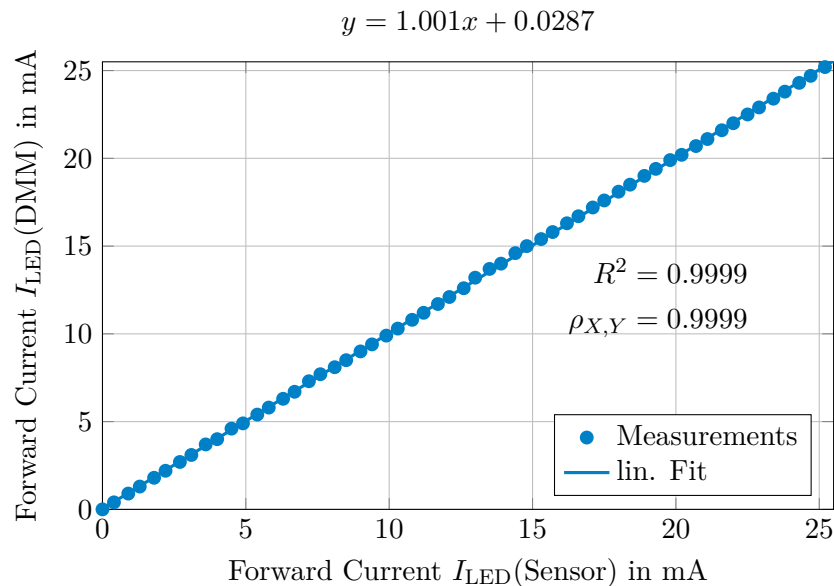


Figure 11.2.: Comparison of forward current I_{LED} measured by LED driver IC and external digital multimeter (DMM).

As mentioned above, LED's have an exponentially increasing current-voltage characteristic. The luminous flux (respectively the emitting light intensity) is almost proportional to the operating current. The forward voltage U_{LED} is set by operation under a constant current I_{LED} . The supply via a constant current source is therefore important for a defined luminous intensity and represents a basic prerequisite for the desired measuring principle.

Figure 11.3 respectively shows the current-voltage characteristic of the IR LED in steps of 0.1 mA in the range from $I_{LED} = 0$ mA ... 25.5 mA. The entire range that can be set via the constant current control of the LED driver IC is covered. In addition, the voltage drop U_{LED} was also measured externally using a multimeter (see Figure 11.3). It becomes clear that the sampling of the multimeter shows a higher resolution than the internal voltage measurement of the LP55231 LED driver IC.

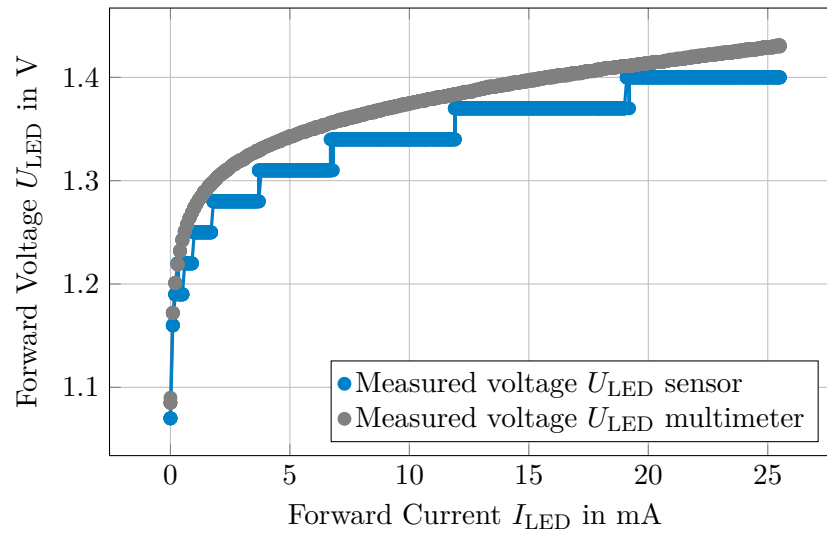


Figure 11.3.: Current-voltage characteristic of the IR LED.

Figure 11.4 shows the current-voltage characteristic of the UV LED. Again, the entire available range of constant current control from $I_{LED} = 0 \text{ mA} \dots 25.5 \text{ mA}$ is examined in steps of 0.1 mA and the resulting voltage U_{LED} is plotted against the forward current I_{LED} . The UV LED shows a lower dynamic, so that an increase of the current I_{LED} in the range $I_{LED} > 7.5 \text{ mA}$ does not result in a change of the forward voltage U_{LED} .

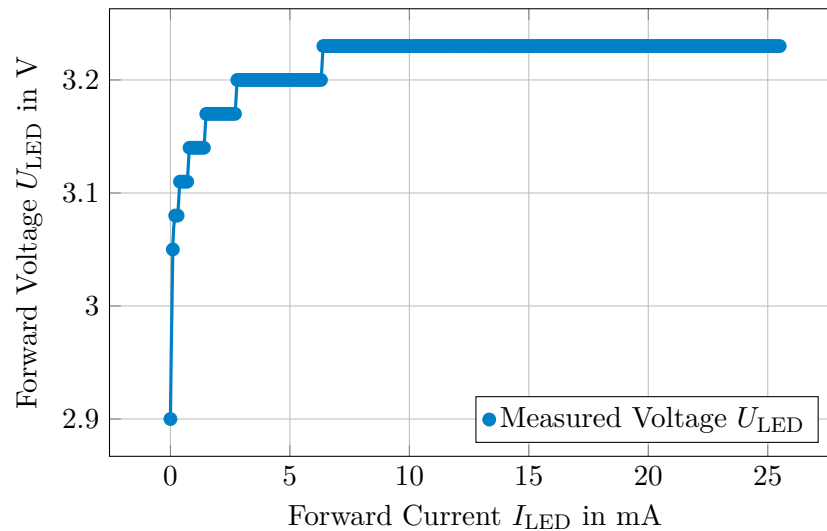


Figure 11.4.: Current-voltage characteristic of the UV LED

11.2. Spectral Characterization of the Emitter Unit

In addition to the electronic properties, the spectral characteristics of the LED's used as light sources are of particular importance for the measurement (see Beer-Lambert-Bouguer Law in Section 5.4). For this reason, a spectral analysis of the used components

is essential in order to describe, characterize and finally evaluate the measurement system in its entirety. Figure 11.5 gives an overview of the wavelength ranges that are important for the measurement system. It shows both the emission spectra of the LED's and the normalized spectral sensitivity of the light-to-digital converters (light sensors). It should be noted that the representation in Figure 11.5 is not to scale, but suitable to clarify the wavelength ranges. A key finding of this simple analysis is that the used LED's have appropriate peak wavelengths and sufficiently narrow emission spectra to match the spectral sensitivities of the light sensors and the requirements formulated in Section 7.1.

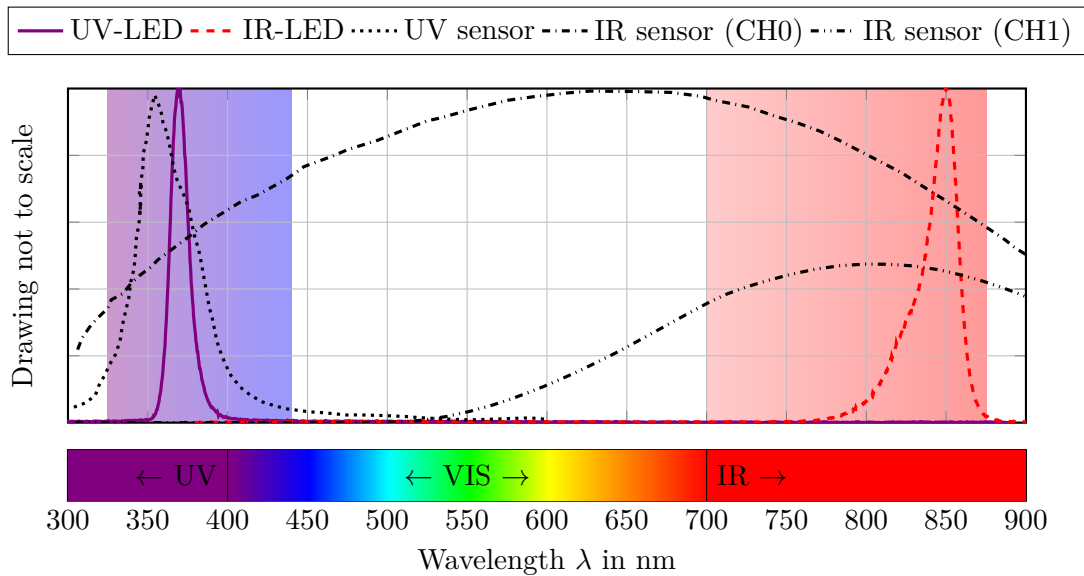


Figure 11.5.: Overview of the wavelength ranges relevant for determining turbidity and CDOM content. Shown are the wavelength ranges (colored) relevant for the optical determination of turbidity (IR range) and CDOM (UV range) using attenuation (transmission measurements), the emission spectra of the UV LED and IR LED as well as the spectral sensitivity range of the light-to-digital converters used (UV and IR sensor).

As described in Section 8.2.2, the intensity of the LED's can be changed both in terms of adjusting the forward current I_{LED} or the PWM value. In order to gain insights into these effects, the emission spectra for different forward current I_{LED} settings were measured. Here again, a spectrometer was used to gather the spectral emission of each LED.

The results of the spectral characteristics of the UV LED are given in Figure 11.6 below. Results for 5 different forward current settings in the range of $I_{LED} = 2.5 \text{ mA} \dots 12.5 \text{ mA}$ are shown for reference. For better comparability, all values were normalized to the maximum value of the highest measured intensity ($I_{LED} = 12.5 \text{ mA}$). As the diagram shows, the curves for a forward current $I_{LED} \geq 7.5 \text{ mA}$ are congruent. This corresponds to the behavior already mentioned for current-voltage characteristic analysis of the UV LED (see Figure 11.4).

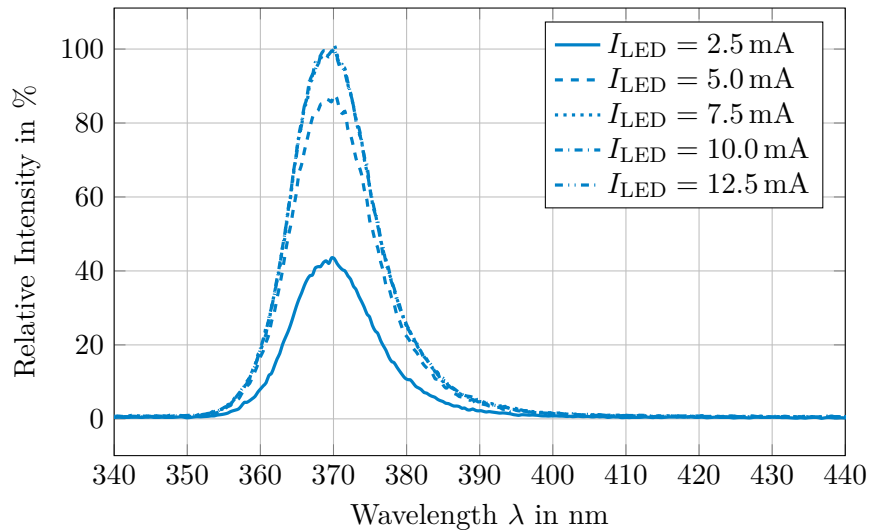


Figure 11.6.: Emission spectra of the UV LED normalized to maximum intensity due to changing forward current I_{LED} (PWM was set to 125).

Based on the same experimental setup, the IR LED was evaluated as well. The results are shown in Figure 11.7 below. As with the current-voltage characteristic analysis (see Figure 11.3), there is a very fine gradation between the constant current settings I_{LED} and the corresponding intensity. The peak wavelength is not influenced by changes in the forward current.

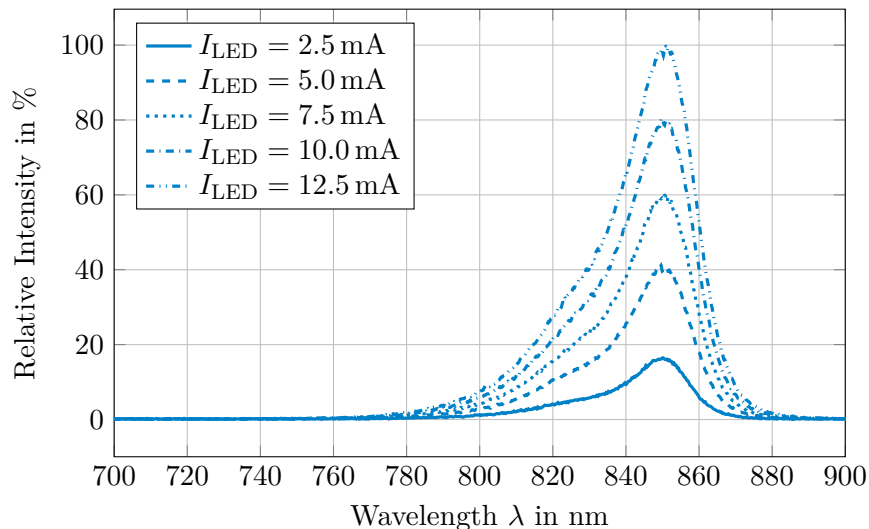


Figure 11.7.: Emission spectra of the IR LED normalized to maximum intensity due to changing forward current I_{LED} (PWM was set to 125).

In addition to adjusting the intensity of the LED by means of forward current control, it is also possible to use pulse width modulation (PWM) for this purpose. The spectral characteristics due to changes in the PWM settings were also investigated. As shown in

Figure 11.8 and Figure 11.9, 5 PWM settings were selected and the emission spectra were compared. It appears that the change of the PWM setting allows a very fine adjustment of the intensity of both the UV LED and the IR LED. The peak wavelengths are not influenced by changes in the PWM setting.

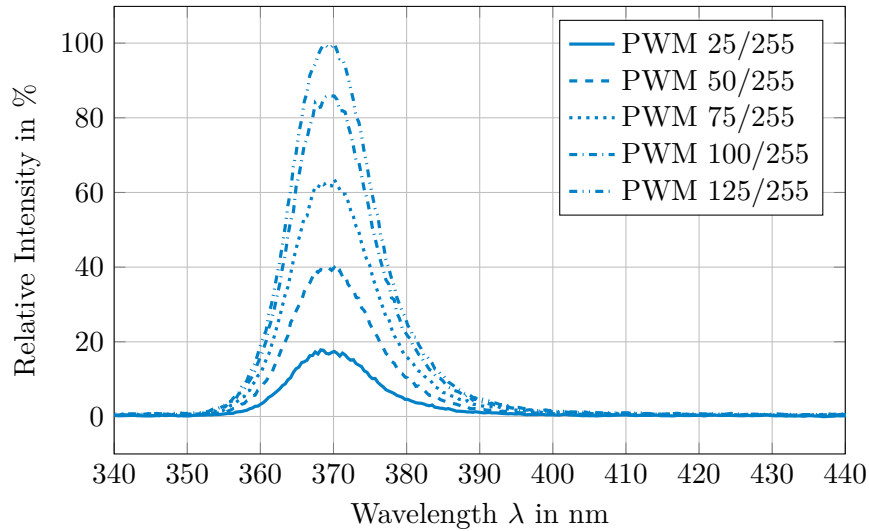


Figure 11.8.: Spectral emission of the UV LED normalized to maximum intensity due to changing PWM. For this test forward current was set to $I_{LED} = 12.5 \text{ mA}$.

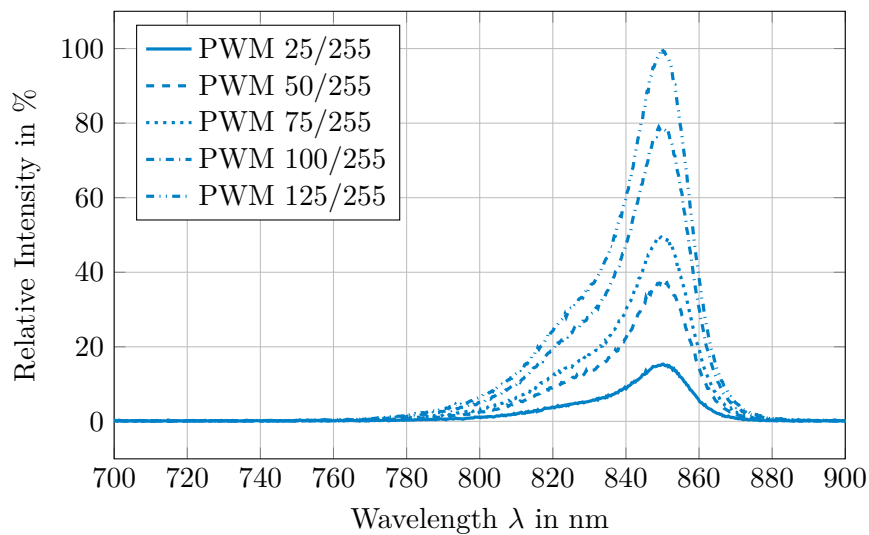


Figure 11.9.: Spectral emission of the IR LED normalized to maximum intensity due to changing PWM. For this test forward current was set to $I_{LED} = 2.5 \text{ mA}$.

11.3. Current-PWM Modulation of the Sensor Probe

Based on the optoelectronic description of the emitter unit, it is possible to examine the overall sensor system feasibility. The Beer-Lambert Law states that for attenuation determination a known amount of incident spectral radiant power $\Phi_i(\lambda)$ is compared to the spectral radiant power $\Phi_t(\lambda)$ transmitted through an aquatic sample volume (see Section 5.4). The incident spectral radiant power $\Phi_i(\lambda)$ can be influenced by changing the forward current I_{LED} drawn through the LED or the duty cycle (PWM) as shown in the previous section (see Section 11.2). Changes in temperature ϑ or ambient pressure p can also influence the spectral radiant power of the LED but regarding the laboratory tests, the temperature is assumed to be constant. Thus, the following formal description is considered as the assumption for the investigation of the emitter site under laboratory conditions:

$$\Phi_i(\lambda) = f \left(PWM, I_{LED}, \overset{const.}{\vartheta}, \overset{const.}{p} \right) \quad (11.1)$$

On the detector side, the measured value for the transmitted spectral radiant power $\Phi_t(\lambda)$ is seen as a function of the incident spectral radiant power $\Phi_i(\lambda)$ and the optical water properties. The value can be changed by modifications in gain or integration time t_I , e.g. to increase the sensor resolution. Other dependencies can be found in a changing temperature ϑ , ambient pressure p or a changing incidence angle ψ_i . For laboratory analysis, these influencing variables are assumed to be constant. Based on these considerations a formal expression can be made as follows:

$$\Phi_t(\lambda) = f \left(PWM, I_{LED}, \overset{const.}{\vartheta}, \overset{const.}{p}, \overset{const.}{\psi_i}, \overset{const.}{t_I} \right). \quad (11.2)$$

In order to examine the measuring range, the sensor probe was placed in a darkened basin with distilled water. During the experiment, the water had a temperature of $\vartheta = 16^\circ\text{C}$. The forward current was gradually changed in the range from $I_{LED} = 0\text{ mA} \dots 25.5\text{ mA}$ and the PWM setting in the range from $0\% \dots 100\%$ duty cycle. For each setting, the corresponding detector signal of the UV and IR channel were recorded.

Figure 11.10 shows the results of the current-PWM modulation of the UV channel. The experiment showed that for a forward current $I_{LED} > 12.5\text{ mA}$ no change in the system characteristics due the current-PWM modulation is achieved. Overall, the color gradient illustrates that a fine adjustment of the measuring range is possible by changing the PWM and forward current setting. Here, the measuring range is the interaction between available incident radiant power and transmitted radiation that can be registered at the detector.

In contrast to this, the investigation of the IR channel shows that a much larger dynamic range can be retrieved as given in Figure 11.11, where a clear gradation in the color gradient of the representation is shown for the entire adjustable range of the current-PWM modulation.

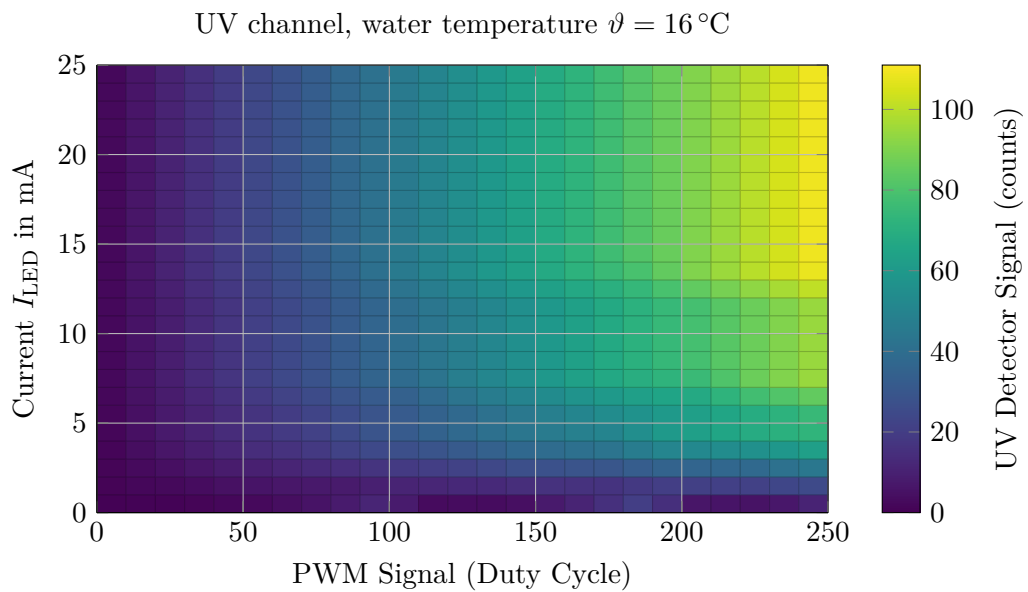


Figure 11.10.: Current-PWM modulation of the UV LED and the corresponding detector signal of the UV light sensor.

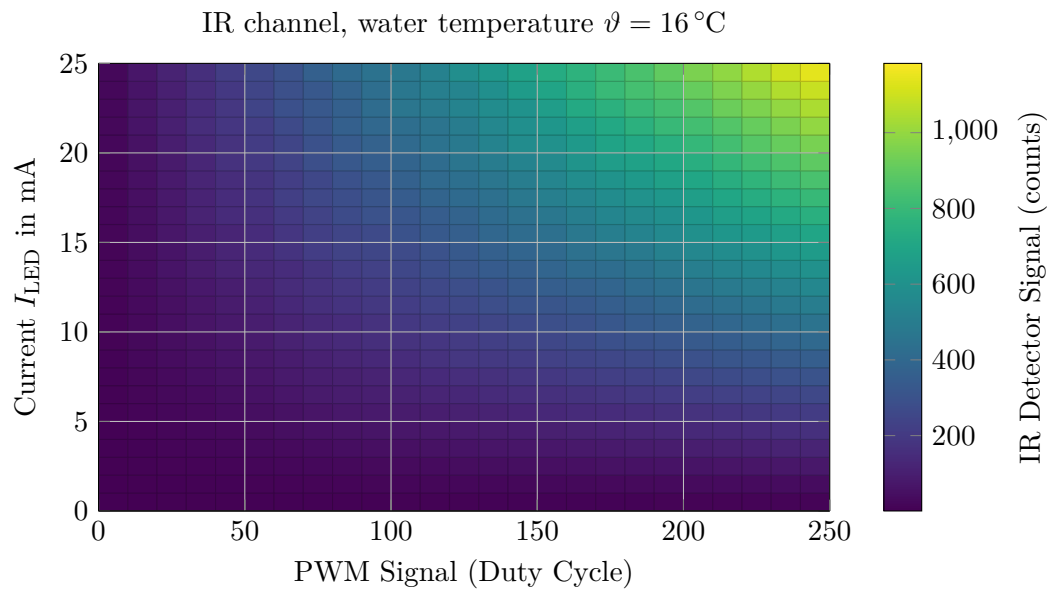


Figure 11.11.: Current-PWM modulation of the IR LED and the corresponding detector signal of the IR light sensor.

For clarification, the results of the current-PWM modulation for selected forward current settings from $I_{LED} = 5 \text{ mA}$ to $I_{LED} = 25 \text{ mA}$ are shown separately. Figure 11.12 contains the data for the UV channel. As mentioned already, currents greater than $I_{LED} > 12.5 \text{ mA}$ do not lead to any significant change in the detector signal. In the case of IR channel as shown in Figure 11.13, it becomes apparent that there is a greater dynamic range achievable, although the curves are not as strictly linear as for the UV channel.

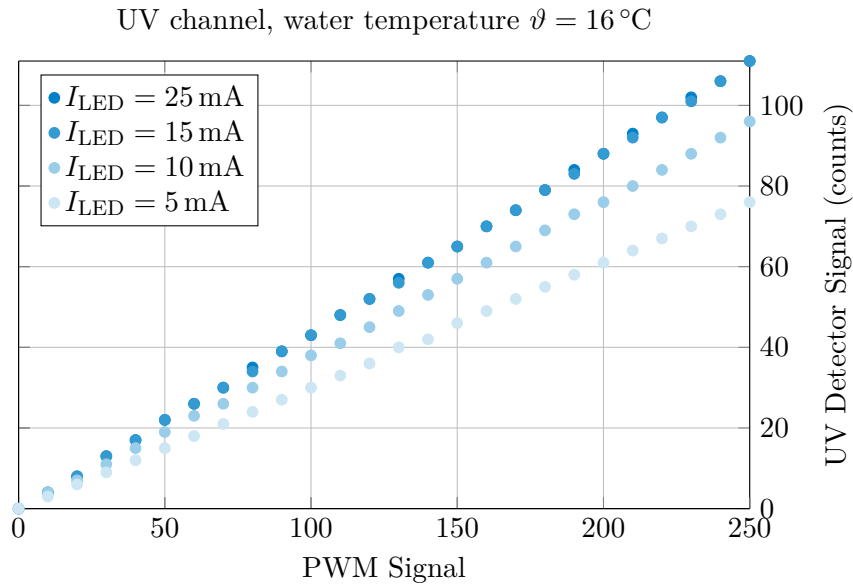


Figure 11.12.: Current-PWM modulation of the UV LED for selected forward currents I_{LED} and the corresponding detector signal of the UV light sensor.

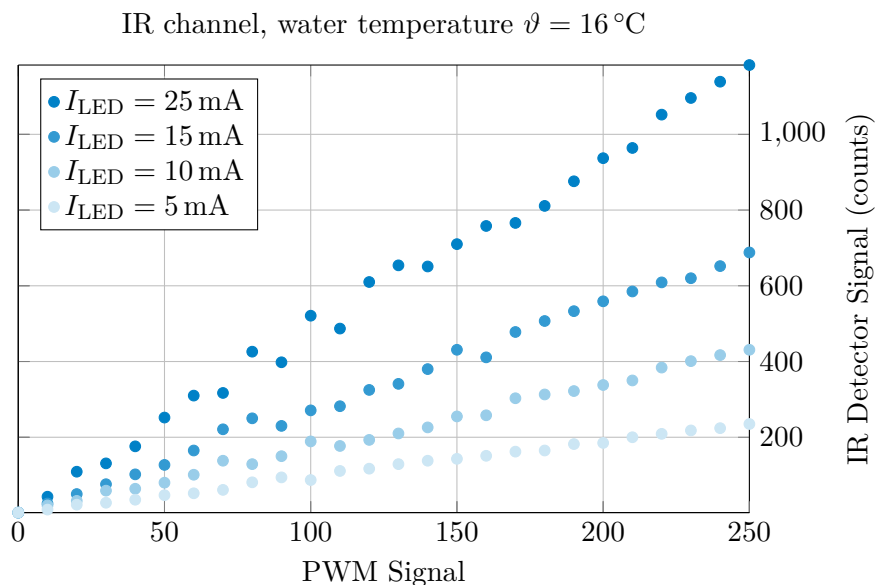


Figure 11.13.: Current-PWM modulation of the IR LED for selected forward currents I_{LED} and the corresponding detector signal of the IR light sensor.

11.4. Repeatability Assessment

In order to investigate the signal stability, the sensor probe was positioned in a closed water tank to exclude ambient light influences. The system behavior was observed for 1 h with a sampling rate of 0.1 Hz. Figure 11.14 shows the measured values of the UV and IR channels as well as the water temperature. To illustrate the distribution, a histogram and the mean average value are provided. As a result, it appears that there is a skew distribution for the UV detector signals. In contrast, the IR detector signals show a rather homogeneous distribution around the mean value. The water temperature has slightly decreased by 0.15 °C during the experiment.

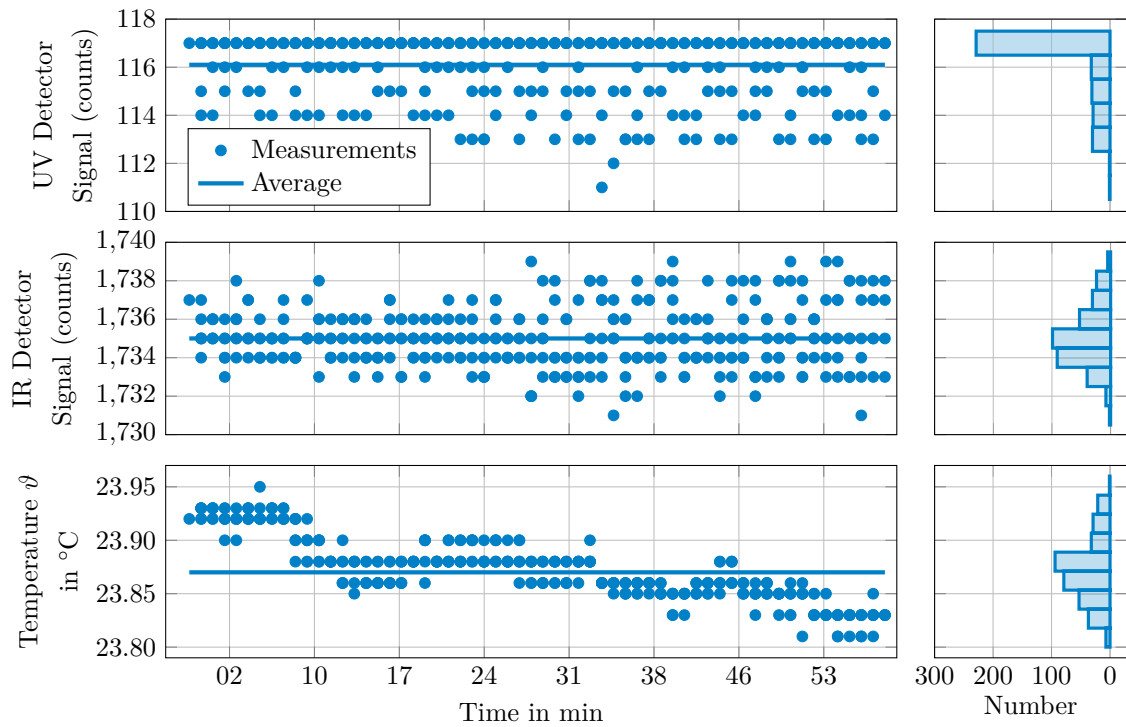


Figure 11.14.: Investigation of the system stability of the sensor system in submerged state over a period of 1 h and a set sampling rate of 0.1 Hz.

In Table 11.1 the results of the statistical analysis of the measurement stability test are listed. Despite a different distribution and a markedly larger value range, the variance and consequently the standard deviation of both variables are nevertheless comparable.

Table 11.1.: Results of the statistical evaluation of the measured values from the 1 h stability testing of the sensor system.

	UV Channel	IR Channel	Temperature ϑ
Average	116.1 counts	1735.0 counts	23.87 °C
Variance	1.94 counts ²	2.35 counts ²	-
Standard deviation	1.39 counts	1.53 counts	-

12. System Characterization Regarding the Anticipated Operating Conditions

With regard to the conditions to be expected during field application, investigations were undertaken on the pressure and temperature dependence of the sensor system.

12.1. Pressure Resistance

Important quality parameters for the investigation of the usability of the sensor system are the pressure stability as well as the analysis of possible pressure dependencies during the sampling process or data gathering. Laboratory pressure tests were carried out up to $p_{\max} = 37$ bar in a pressure tank as described in Section 10.2. The sensor probe was placed in the pressure tank for this purpose. The signal transmission and power supply through the pressure tank wall was ensured via a pressure-compensated connector box. The pressure was gradually increased with a pressure change rate of 2.56 bar/min and the corresponding measured values recorded. Figure 12.1 shows the results for the UV channel of the sensor system, normalized to the initial detector value at atmospheric ambient pressure.

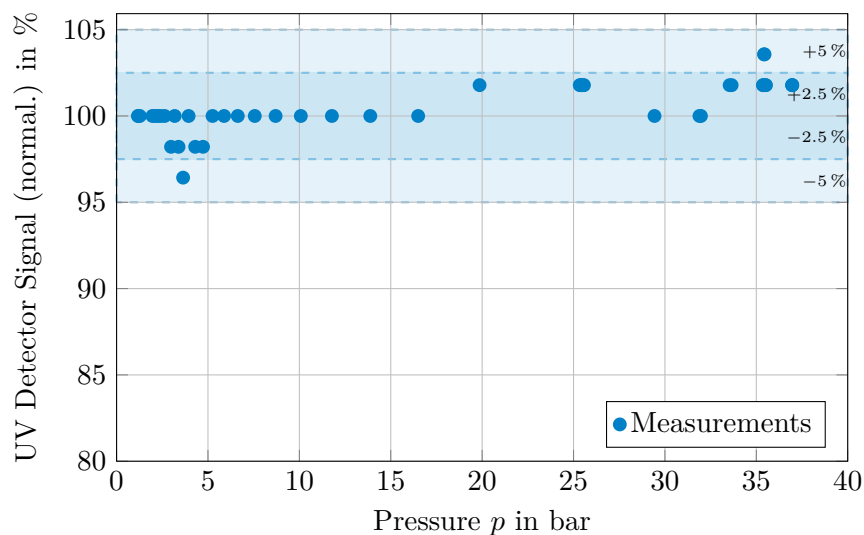


Figure 12.1.: Pressure dependency test of the sensor probe (UV channel). Detector signals are normalized to the signal under atmospheric ambient pressure. The blue colored areas mark the range of $\pm 2.5\%$ and $\pm 5\%$ deviation.

The results show that the changes in the signal of the UV channel in dependence on the ambient pressure are negligibly small. Variances of less than $\pm 2.5\%$ were observed across the entire area.

A similar result was found in the examination of the IR channel. Figure 12.2 shows the results normalized to the initial value at ambient pressure. Although the overall noise is more pronounced than compared to the UV channel, the measured value deviations are still negligible and well below 5%.

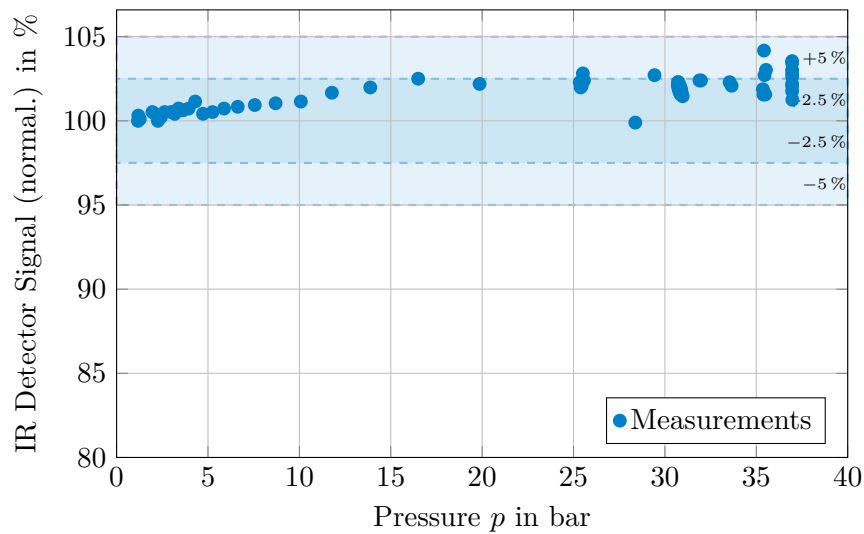


Figure 12.2.: Pressure dependency test of the sensor probe (IR channel). Detector signals are normalized to the signal under atmospheric ambient pressure. The blue colored areas mark the range of $\pm 2.5\%$ and $\pm 5\%$ deviation.

12.2. Temperature Compensation

LED's have an exponentially increasing current-voltage characteristic, which also depends on the temperature. Therefore, the luminance of an LED is a function of its temperature even though the forward current I_{LED} flowing through the LED remains constant. Since the application requires a constant luminance of the emitter (incident radiant power $\Phi_i(\lambda)$), an appropriate temperature compensation is a prerequisite to avoid luminance and color purity variations due to temperature changes and therefore inaccuracies of the measurement.

In Figure 12.3 the outcomes of the temperature dependence test for the UV channel are shown. Here, the raw sensor readings were plotted against the changing PCB temperature ϑ_{PCB} due to the changing water temperature ϑ_{H_2O} in a range of $\vartheta_{H_2O} = 8 \dots 25^\circ\text{C}$. A linear regression analysis provides a formal linear relationship of $y = 4.1x + 45.5$ with a determination of $R^2 = 0.9899$ and a linear correlation coefficient of $\rho_{X,Y} = 0.9949$.

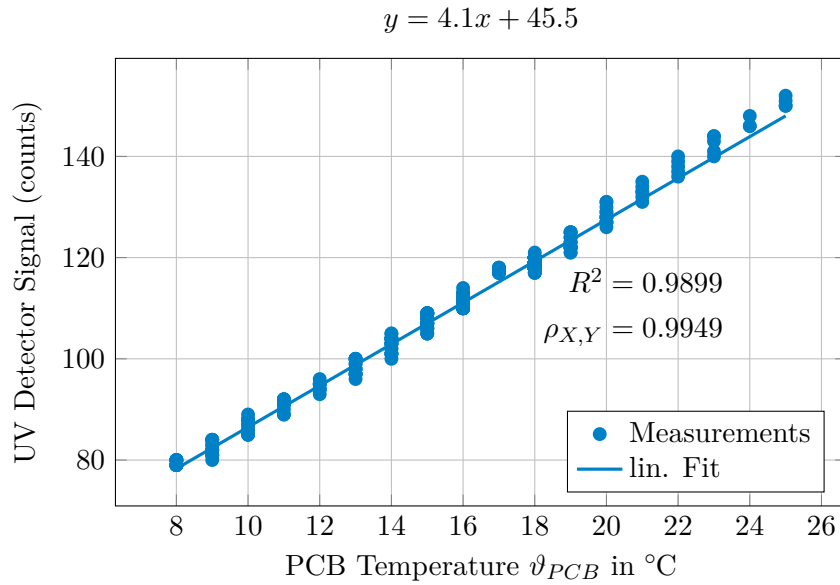


Figure 12.3.: Temperature compensation test of the UV channel ($N = 4885$).

In Figure 12.4 the outcomes of the temperature dependence test are again shown but in this case for the IR channel of the sensor probe. Once more, the raw IR light sensor readings were plotted against the changing PCB temperature ϑ_{PCB} due to the changing water temperature ϑ_{H_2O} in a range of $\vartheta_{H_2O} = 8 \dots 25^{\circ}\text{C}$. A linear regression analysis provides a formal linear relationship of $y = 6.7x + 1615.1$ with a determination of $R^2 = 0.9300$ and a linear correlation coefficient of $\rho_{X,Y} = 0.9643$.

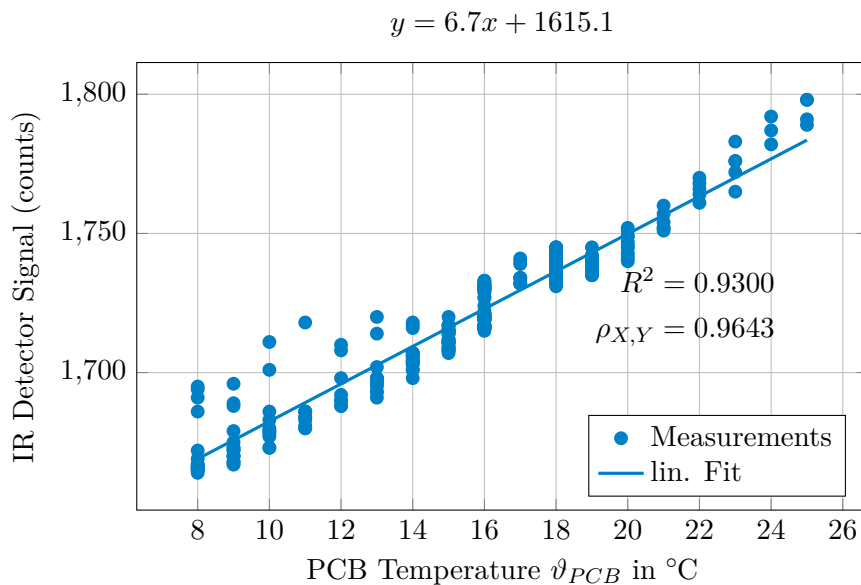


Figure 12.4.: Temperature compensation test of the IR channel ($N = 4885$).

13. Measurement Quality Assessment

To determine the quality of the turbidity and CDOM approximation, a comparison between the sensor probe and a reference method is needed. The use of a laboratory photometer to optically determine water quality represents an established standard in environmental analysis (DIN EN ISO 7027, 2000; DIN 38404-3, 2005). For this reason, the developed in-situ sensor system is compared with this method. To sufficiently compare the sensor system and the laboratory photometer over a representative measuring range, 29 samples were prepared by mixing milk and purified water with different ratio leading to a varying turbidity and different CDOM concentrations. For the comparison, plastic cuvetts¹ with an optical path length of $d = 1$ cm were used both for the analysis with the laboratory photometer and the prototype sensor system components.

13.1. Assessment of CDOM Approximation

Results of the comparison for CDOM determination are given in Figure 13.1, where the sensor readings are plotted against the laboratory photometer measurements. A linear regression analysis provides a formal relationship of $y = 2.5x + 229.0$ with a determination of $R^2 = 0.9440$ and a linear correlation coefficient of $\rho_{X,Y} = 0.9716$.

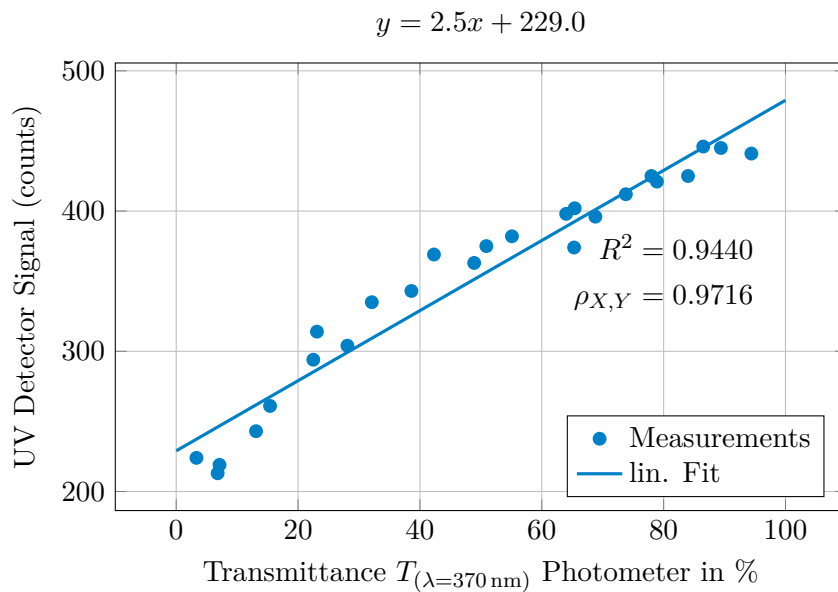


Figure 13.1.: Comparison of CDOM approximations derived by the optical sensor system and a laboratory photometer at a wavelength of $\lambda = 370$ nm.

¹ neoLab macro PS cuvet, E-1641, neoLab Migge Laborbedarf-Vertrieb GmbH, Germany

The comparative analysis reveals a strong correlation between the measured values obtained with the sensor system and those obtained with the photometer. It must be noted that the laboratory photometer provides transmission values in the range from 0 % to 100 %. Comparing these with the measured values of the sensor system, it becomes apparent that the detection limit of the measuring system has not been reached for the given case.

13.2. Assessment of Turbidity Approximation

The outcomes of the comparison for turbidity determination are shown in Figure 13.2 below. Here, the sensor readings ($\lambda = 850 \text{ nm}$) were plotted against the laboratory photometer measurements derived by the photometer. The values are represented in formazine attenuation units (FAU). A linear regression analysis provides a formal relationship of $y = -0.3x + 437.1$ with a determination of $R^2 = 0.9672$ and a linear correlation coefficient of $\rho_{X,Y} = -0.9805$.

Again, the analysis reveals a good correlation between sensor readings and the laboratory photometer measurements. It also becomes clear that for higher turbidity values a better correlation is achieved. While the measurement using the laboratory photometer is limited to a maximum of 400 FAU in the measuring range, again the sensor system is not reaching the detection limit for the given case.

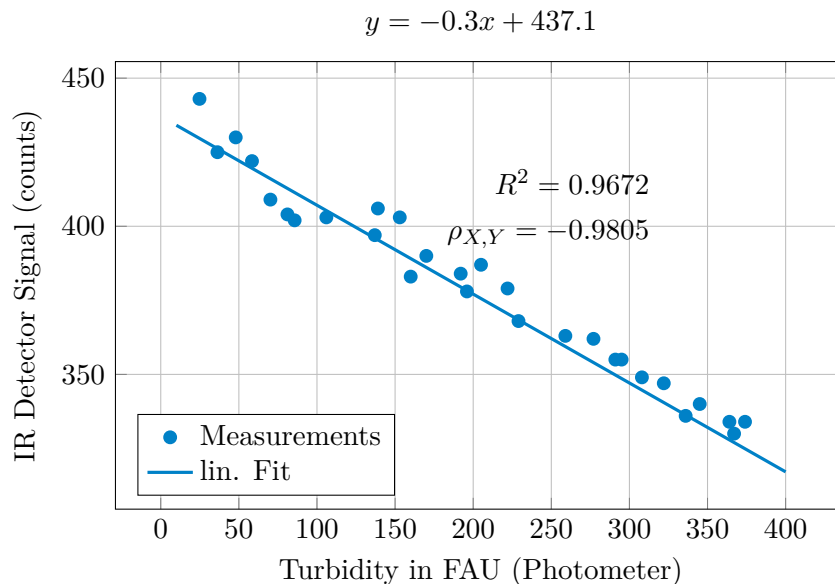


Figure 13.2.: Comparative analysis of water samples of different turbidity between a laboratory photometer and the developed sensor system. The results of the photometer measurement are given in formazine attenuation units (FAU).

Part VI.

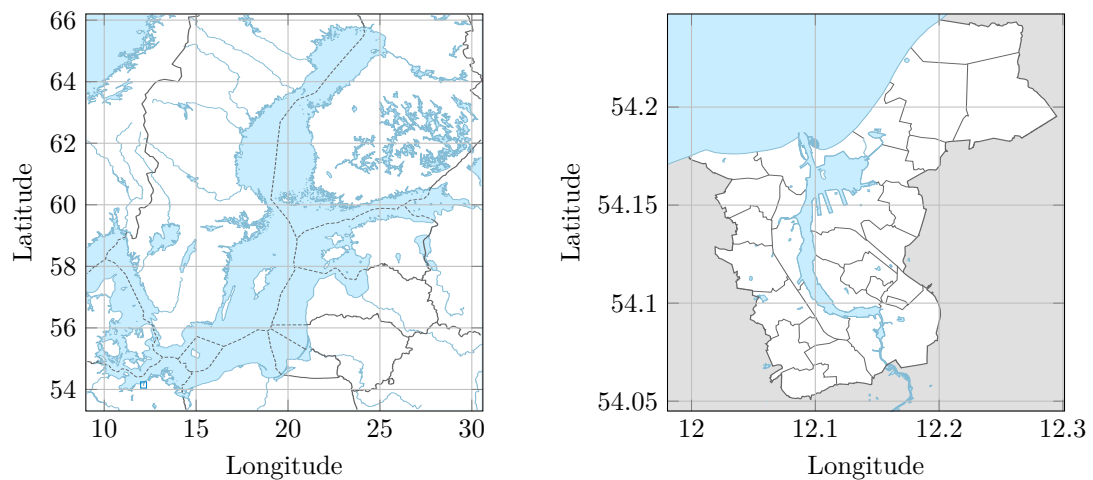
Case Study

14. Mobile Turbidity and DOM Monitoring

The overall objective of this work is to provide a tool for a service-oriented in-situ monitoring. To this end, the basic feasibility will be demonstrated by means of a field case study. Within the next section, the results of two exemplary monitoring campaigns are presented, which were carried out on the Unterwarnow along the city area of Rostock, Germany, in summer 2018.

14.1. Site description

The 155 km long Warnow is a river in Mecklenburg-Western Pomerania, Germany, which flows into the southern Baltic Sea (see Figure 14.1a). The catchment area of the Warnow covers 3324 km² and is characterized by agricultural land use, which is common throughout the Baltic Sea region. Especially the last section of the river, the Unterwarnow, as shown in Figure 14.1b, is an interesting study area in terms of water quality due to varying ecosystem conditions. Hydrologically it is a bay of the Baltic Sea, an inner coastal water. Therefore, the salt content in the northern area of the Unterwarnow is markedly increased. Anthropogenic inputs of nutrients and pollutants as well as high ship traffic such as container ships, ferries and cruise ships in this area are further influencing factors.



(a) Geographical map of the Baltic Sea region. (b) Map of the city of Rostock and the course of the Unterwarnow with the estuary area.

Figure 14.1.: Map of the Baltic Sea region as well as the city of Rostock and the course of the Unterwarnow with the area of the seaport and the estuary of the Warnow into the Baltic Sea.

Estuaries are characterized by the transition of fresh water to salt water (brackish water), where the transport of substances is normally a result of water movements. In practice, this is dependent on the flow velocity of the freshwater outflow quantity of the river in relation to the saltwater inflow quantity, which in turn is dependent on the respective weather conditions, e.g. storm tides. This results in a very differing change of the flora and fauna from the river area to the sea due to the average salinity, water temperature, amount of dissolved organic matter or nutrients.

14.2. Challenge

The challenge regarding the in-situ monitoring reflects the problem described in the introduction to this thesis (see Section 1.1). The objective is to understand ecosystems such as the Baltic Sea in their entirety. Since this also includes estuaries, river courses and the related catchments, there is a lack of suitable monitoring strategies and technologies to measure and describe these systems. To this end, one of the main aims of the case study is to reveal the potential of the developed method of being a suitable approach for a service-oriented, fast and easy to apply in-situ monitoring of optical properties in above described aquatic environments. A scale-overlapping monitoring must be based on technologies that are not dependent on large research infrastructures. Mobile sensors that can be used from small boats such as fisherboats, sailboats or canoes would make an enormous contribution not only to increase data density but also to collect data in areas where conventional environmental research has not yet advanced.

14.3. Materials and Methods

Due to the service-oriented system architecture, the methodological effort during the field measurements is moderate. As described in Section 9, the sensor system consists of the sensor probe, which is connected to the topside unit via a cable and a connector. The topside unit can be powered via a USB connection or from 12 V . . . 32 V (DC) power supply. In the present case, a USB power bank¹ with a capacity of 20 100 mA h was used. This allows the measuring system to be operated for about 48 hours. The sensor probe can be easily mounted using the metal brackets integrated into the sensor housing on the top and bottom. Since the sensor probe weighs only 0.12 kg or 0.87 kg with 30 m cable length attached, the installation for field applications is simple. The user thus has the option of simply bringing the sensor into the water at the cable, using a rope or attaching the sensor to a device carrier or frame. Conventional measuring systems are usually bigger and also heavier than the sensor system presented here (see Section 8.4). With the sensor system it is therefore possible to introduce new data collection strategies and technologies in addition to classical monitoring based on the use of research vessels.

¹ TL-PB20100, Portable Power Station, 20 100 mA h Capacity, TP-Link Technologies Co., Ltd., USA

For this purpose, two monitoring applications were tested as part of the case study. On the one hand a monitoring with a canoe was carried out, enabling data acquisition in very shallow river areas and small stream inlets of the Warnow. The sensor installation for this case is shown in Figure 14.2 below. The sensor probe is attached to a mount which allows to change the sampling depth as well as the angle and orientation of the sensor from on board.

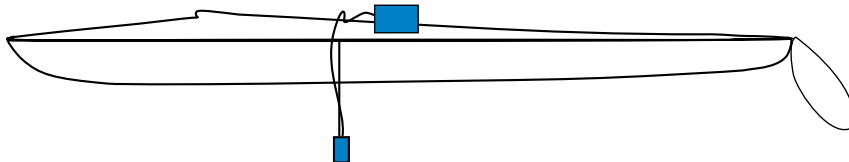


Figure 14.2.: Sensor installation on a canoe for mobile monitoring.

In the second application case the sensor system was mounted on a sailboat to sample larger areas such as the Warnow estuary into the Baltic Sea. The installation situation is shown in Figure 14.3 below. The sensor probe was attached to the stern of the sailboat on the bathing ladder. Since higher flow velocities were to be expected than in the canoe application, the cable was fixed with cable ties in order to minimize the tensile load on the cable and the cable gland as a result of the incident flow.

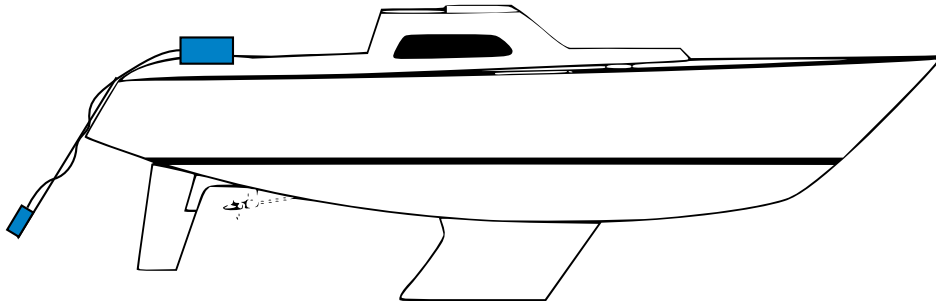


Figure 14.3.: Sensor installation on a sailboat for mobile monitoring.

Once the sensor probe is deployed, the system can be switched on without further need for additional user interactions. As long as there is a stable internet connection, e.g. via an access point provided by a mobile phone, the data gathered by the system is automatically transmitted to the server and processed to provide a data visualization close to real time using standardized web services. This is achieved with the help of the standardized JSON data format as discussed in Section 9.2.2, which allows direct post-processing with the help of corresponding libraries and plugins.

The measuring system also functions without internet connection and stores the data on an SD card. Each completed measurement is confirmed by the LED status display of the power button, which flashes twice briefly. This ensures that the measuring system is correctly configured and data loss is avoided.

14.4. Results

The results of the two monitoring campaigns are presented below. Since mobile monitoring is particularly concerned with spatial heterogeneity, the measured parameters are shown as a map view. In addition, time series are presented which provide information on whether there are superordinate dependencies or a general dynamic. Nonetheless, it is important to note that the case study serves to demonstrate the basic feasibility of the sensor system. A comprehensive monitoring of the study area would require that measurements are taken over a longer period of time, at regular intervals and that appropriate laboratory analyses are carried out. For this reason, only the raw data are shown in the result presentation.

14.4.1. In-situ Monitoring Using a Canoe

In the first application example, monitoring was carried out using the canoe. The study area was the Warnow section between Mühlendammschleuse, lock Rostock, southeast of the city centre (1) and the area of the former Neptun shipyard northwest of the city centre (5). Figure 14.4 contains a map view of the water temperature values measured during the field campaign. The temperature fluctuated between 25.0 °C...27.0 °C. The measurements reveal that the area of the Unterwarnow (from (3) to (5)) has an overall higher water temperature than the narrower river course between (1) and (3).

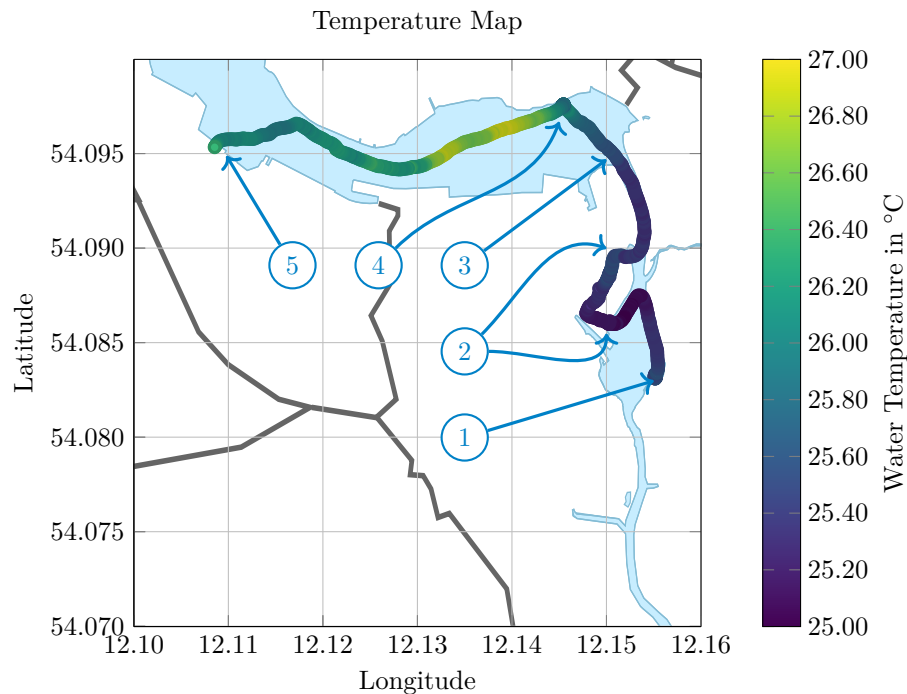


Figure 14.4.: Spatial plot of the temperature measurements of the monitoring campaign by canoe (2018-08-04). (1) Mühlendammschleuse, (2) Haargraben, (3) beginning of the Unterwarnow, (4) reed belt, (5) Neptun shipyard.

Figure 14.5 shows the course of the measured values of the UV transmission measurement ($\Phi_t(\lambda = 370 \text{ nm})$) during the monitoring campaign. The areas close to the lock (①) and along the shallow moat (Haargraben (②)) are in particular characterized by a strong decrease in the transmission signal. This could indicate an increased concentration of CDOM. In the area of the Unterwarnow very high transmission values are noticeable (see point (③) in the map). Regarding the remaining areas, the monitoring showed a comparatively homogeneous pattern. Close to point (④) a point measurement was done inside of a reed belt for about 20 min to see if the sensor reveals constant values. The monitoring was completed at a shallow pier near the former Neptun shipyard (⑤). In this area a slight decrease in the transmission signal can be observed, which could again be attributed to an increased concentration of CDOM.

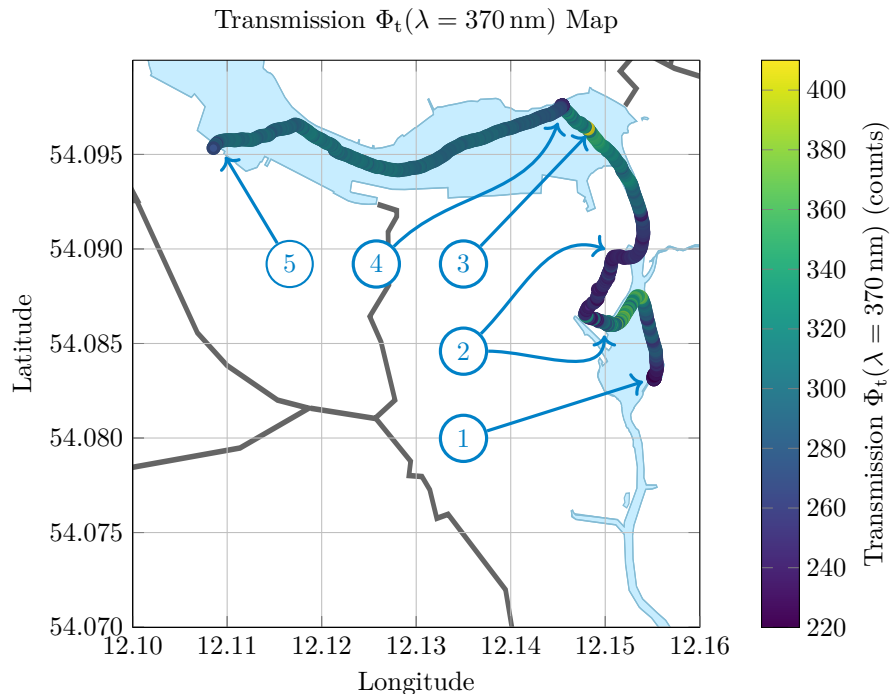


Figure 14.5.: Spatial plot of the UV transmission measurements of the monitoring campaign by canoe (2018-08-04). ① Mühlendammschleuse, ② Haargraben, ③ conspicuous value at Unterwarnow, ④ reed belt, ⑤ Neptun shipyard.

Figure 14.6 shows the results of the monitoring campaign for the IR transmission measurements ($\Phi_t(\lambda = 850 \text{ nm})$). Overall, it can be seen that the course of the measured value is very similar to the results of the UV transmission measurement. This can be interpreted as a first indication that the weakening of the transmission signal is mainly due to turbidity of the water and less to the CDOM content.

Nonetheless, the signal course provides information about the water body. In this case, differences between the areas can be detected once more. Major signal weaknesses especially occur in the area of the Mühlendammschleuse (①) and along the shallow moat,

the Haargraben ② . A similar situation can be observed in the area of stationary measurements in the reed belt of the Unterwarnow ④ . Here again, a weakening of the transmission signal can be observed in the shallow area of the pier near the former Neptunwerft ⑤ .

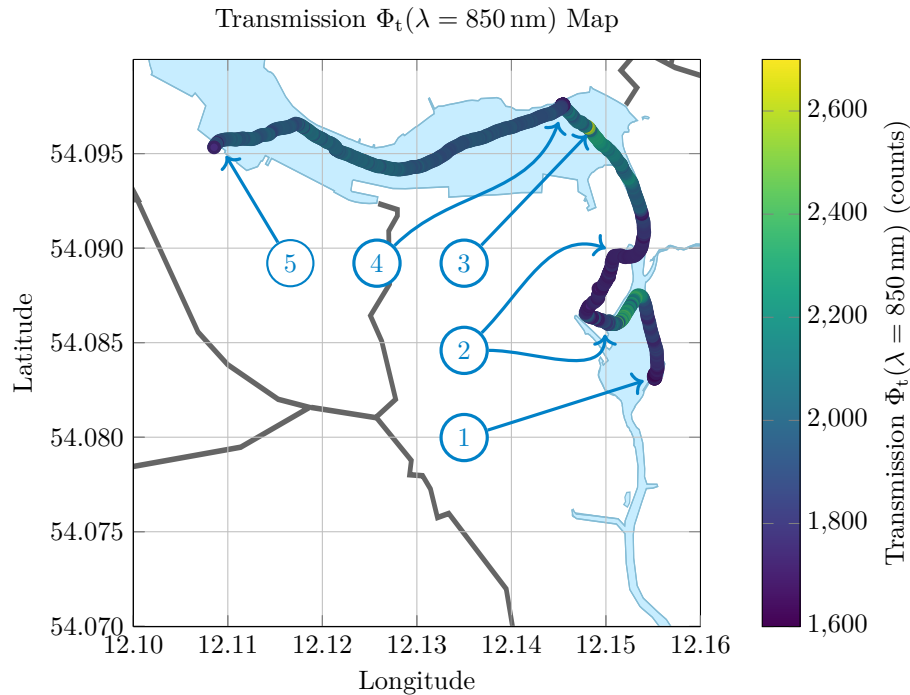


Figure 14.6.: Spatial plot of the IR transmission measurements of the monitoring campaign by canoe (2018-08-04). ① Mühlendammshleuse, ② Haargraben, ③ beginning of the Unterwarnow ④ reed belt, ⑤ Neptun shipyard.

In order to better compare the individual measurement results, a time series analysis was carried out in addition to the spatial plots of the data. Figure 14.7 shows the results of the UV and IR transmission measurement as well as the course of the water temperature ϑ_{Water} plotted over time. It becomes clear that the course of the UV and IR transmission measurements is similar but not congruent, which is especially true for the area between ① and ② . Nevertheless, the impression arises that the sensor signal of both optical channels is mainly influenced by the turbidity of the water since the values of both channels are showing a similar course over time.

At point ② , very high transmission values are recorded for both signals. These could be outliers, though the values lie in a range in which generally higher transmission values were measured. For future studies, this would be a suitable place to carry out more detailed investigations using appropriate sampling techniques and a subsequent laboratory analysis. At point ④ , within a reed belt of the Unterwarnow, a stationary measurement was carried out over a period of about 20 min. Here, a constantly low value was found over the entire period. The low transmission on both optical channels suggests that similarly

high turbidity values prevailed here like in the area of the Mühlendammschleuse ① or the Haargraben ②. Along the Unterwarnow to the former Neptunwerft ⑤ higher transmission values were observed on both optical channels. This allows at least the interpretation that the water body has a lower turbidity than in the previously described areas. In the shallow water area of the pier at the old Neptun shipyard, lower transmission values were registered again.

The course of the water temperature can also be used as a reference for the assessment of the water body. In the area between point ④ and point ⑤ there is a clear increase in water temperature. In this area of the Unterwarnow, the river bed opens considerably wider and has a mean depth of less than 2 m outside the buoyed fairway.

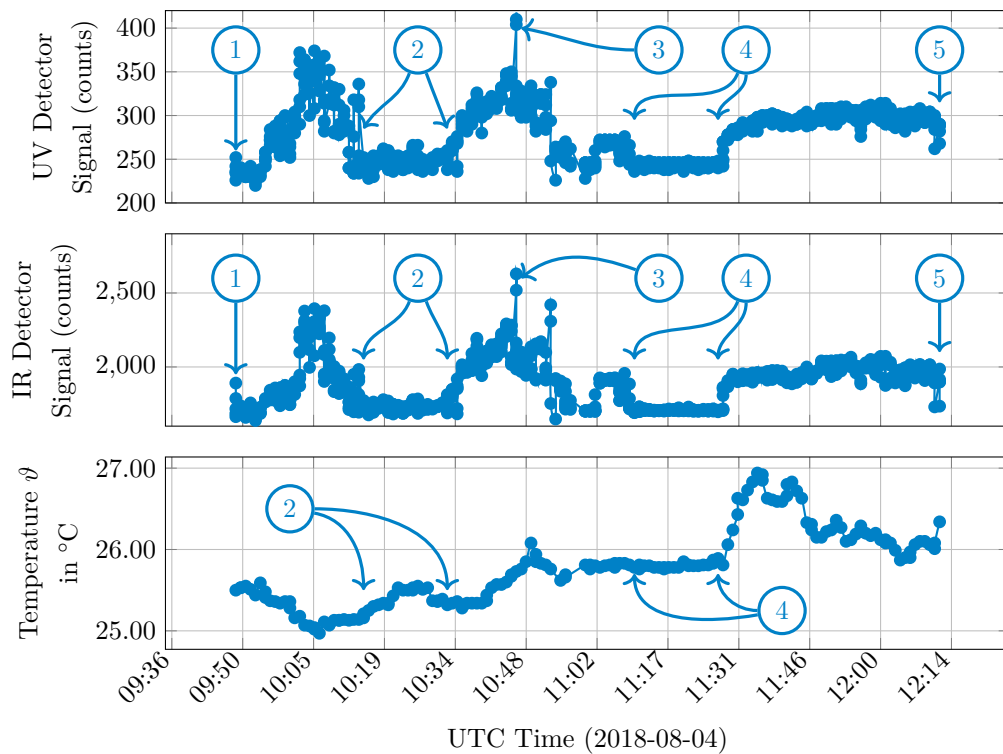


Figure 14.7.: Time series of the monitoring results of the measurement campaign by canoe. Shown are the values of the UV and IR transmission measurements as well as the water temperature, each measured with a sampling rate of $\frac{1}{10}$ Hz. ① Mühlendammschleuse, ② Haargraben, ③ beginning of the Unterwarnow ④ reed belt, ⑤ Neptun shipyard.

14.4.2. In-situ Monitoring Using a Sailboat

For the second monitoring campaign, the sensor system was mounted on a sailboat and the estuary area of the Warnow was covered by the monitoring, starting at the height

of the Warnow tunnel and ending at the mouth of the Warnow in the Baltic Sea near Warnemünde. This includes the entire fairway of the Rostock overseas port (Rostock Port), the ferry port, the cruise ship terminal and the area where the Warnow ferry crosses between the city district Warnemünde and Hohe Düne.

Figure 14.8 shows the map view of the water temperature as a result of mobile monitoring. As already mentioned, from a hydrological point of view the Unterwarnow is a bay of the Baltic Sea and therefore an inner coastal water. The temperature pattern is therefore interesting, as it shows a constantly decreasing trend towards the Baltic Sea even though the temperature difference of about 0.5 °C is low. At the beginning of the measurement the water temperature is still at a constant level. At point ① the first ferry terminal is passed and a decrease of the temperature can be observed. A further drop in temperature occurs at point ③. This is the area where the Warnow ferry operates and the cruise ship terminal is located. GPS reception was interrupted at two points, resulting in smaller data gaps.

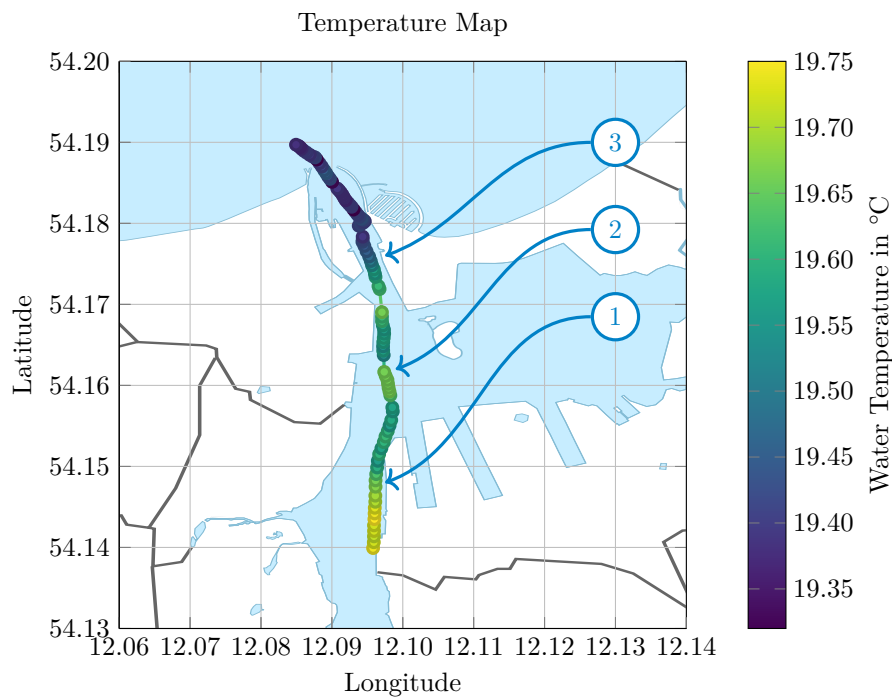


Figure 14.8.: Spatial plot of the temperature measurements of the monitoring campaign using a sailboat (2018-09-02). ① Ferry terminal Rostock Port, ② Crossing area of the fairways Überseehafen, ③ Ferry Warnemünde.

Figure 14.9 shows the results of the transmission measurements of the UV channel as a map view. At the beginning of the measurement campaign between the Warnow Tunnel and the ferry terminal of the overseas port ①, transmission values remained constant. After the first ferry terminal has been passed, the Warnow basin (the Breitling) opens. In this area the transmission values increase slightly. At point ②, where the fairways

and shipping lanes cross from the direction of the Rostock city ports and the overseas port, there are significantly lower transmission values than in the areas before. During the measuring campaign there was a lot of shipping traffic in this area, so the ferries to Scandinavia left one after the other and also a container ship crossed the course of the sailing boat during the measuring. Since the temperature measurement for this area also shows a slight change (see Figure 14.8), it can be assumed that the water column was mixed up accordingly. This would explain that the transmission values as a result of swirled sediments and organic matter from deeper layers are significantly lower than in the areas before. The depth of the sea channel is about 14.5 m at this point. Another remarkable point can be found in the area of the Warnow ferry (3). Once again, the transmission values decrease significantly. In this area two smaller car and passenger ferries cross every 20 min between both sides of the river. The passenger quay of the cruise ships mooring is also located there. Consequently, it does not appear implausible to find an increased CDOM concentration in this area due to an increased mixing of the water column and external impacts.

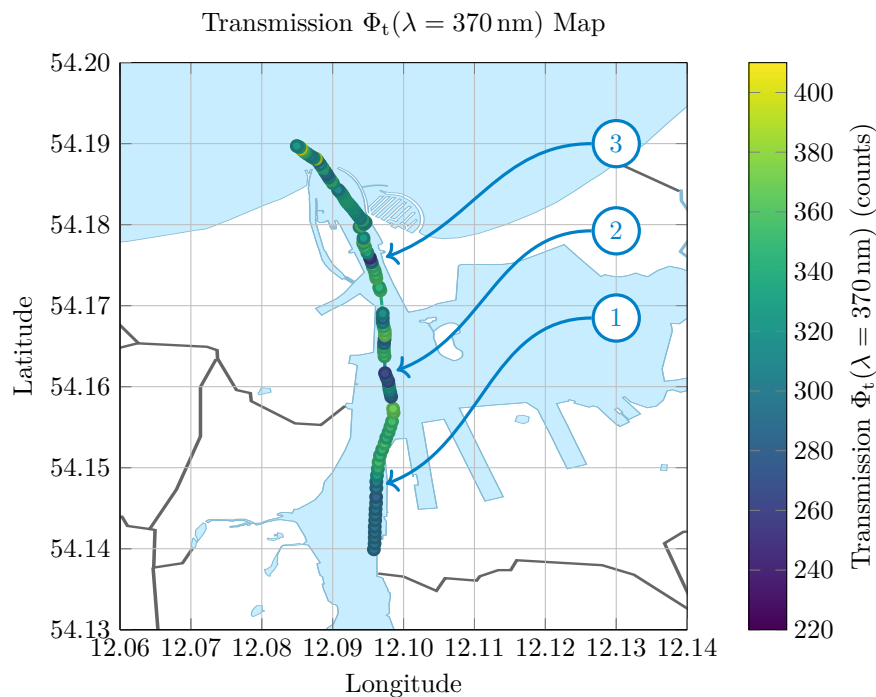


Figure 14.9.: Spatial plot of the UV transmission measurements of the monitoring campaign using a sailboat (2018-09-02). (1) Ferry terminal Rostock Port, (2) Crossing area of the fairways Überseehafen, (3) Ferry Warnemünde.

Figure 14.10 shows the spatial map representation of the transmission measurements of the IR channel. In comparison to the transmission measurements of the UV channel, a greater dynamic is shown here, but in other areas. It is interesting to see that from the beginning of the measurement from the Warnow Tunnel to the sea channel, the transmission remained

almost constant. At point (a), where the fairways are crossing, a clear weakening of the transmission signal takes place, which also occurs over a longer range. The clear change, which can be seen in the transmission signal of the UV channel in the area of the ferry terminal (1), cannot be determined here. A further deviation can be found at point (b). Here a clear reduction of the transmission signal for the IR channel can be seen, which cannot be found in the values of the UV channel. In the area of the Warnow ferry the signal strength of the IR channel also decreases. As with the UV channel, it is assumed that the generally increased ship traffic in this area causes a stronger mixing of the water body with swirling of the sediment. In addition, 2 large cruise ships were moored at the quay on the day of the measurement, which could have an additional influence on the condition of the water body.

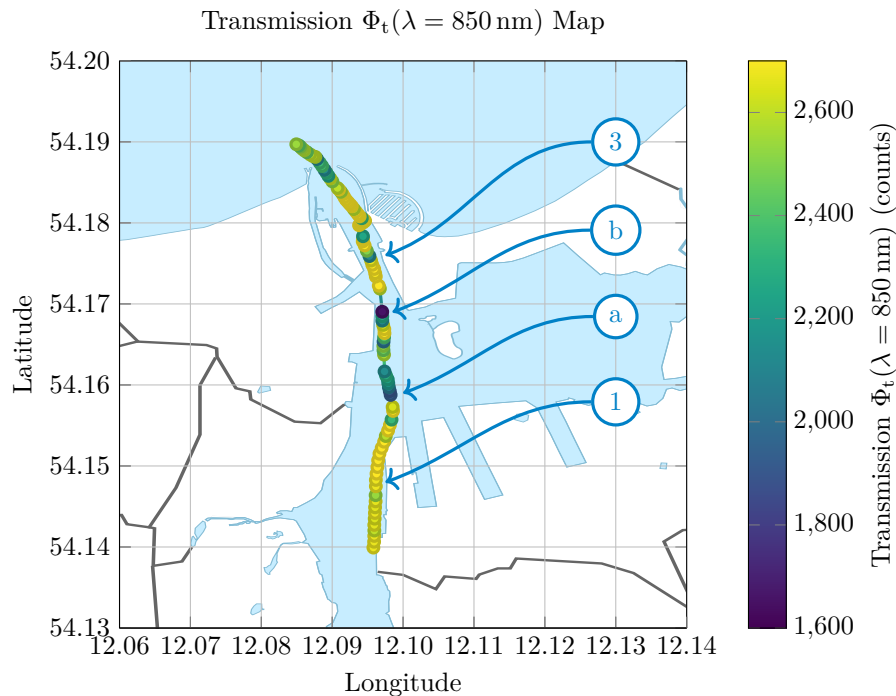


Figure 14.10.: Spatial plot of the IR transmission measurements of the monitoring campaign using a sailboat (2018-09-02). (1) Ferry terminal Rostock Port, (a) Crossing area of the fairways Überseehafen, (b) Sea channel, (3) Ferry Warnemünde.

For better comparability of the results, a time series analysis is carried out as well. Figure 14.11 shows the results of the second field campaign plotted over time. In contrast to the first measurement campaign, the signal characteristics of the two optical channels differ with regard to transmission.

As already mentioned, the transmission measurement of the UV channel shows lower intensities at the beginning of the measurement series. Until reaching the ferry terminal in point (1), the signal curve differs significantly from the transmission measurement of

the IR channel. Here the assumption is reasonable that there is a hydrological transition between the rather limnic part of the Unterwanow and the harbor area, which is rather equivalent to the conditions of the Baltic Sea. These circumstances could also explain the drop in temperature. Certainly, the changed water depth in this area is also important. With greater water depth and at the same time more ship traffic, another mixing and distribution situation prevails in the water column leading to a change in the conditions. It may therefore be plausible if the CDOM content, which previously led to low transmission values, decreases in these areas of the Warnow. The measured values in the area of point ②, the crossing area of the fairways of the Rostock city ports as well as the overseas and ferry port show a very high dynamic with partly very low transmission values for both optical channels. The water temperature also shows fluctuations in this range, but to a very small extent.

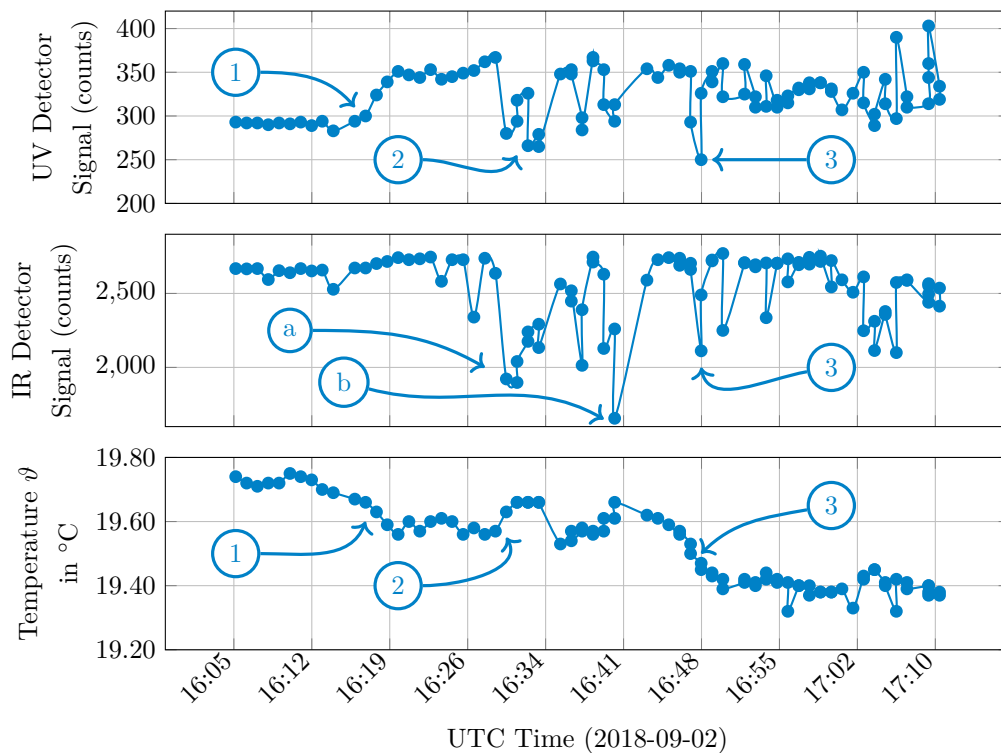


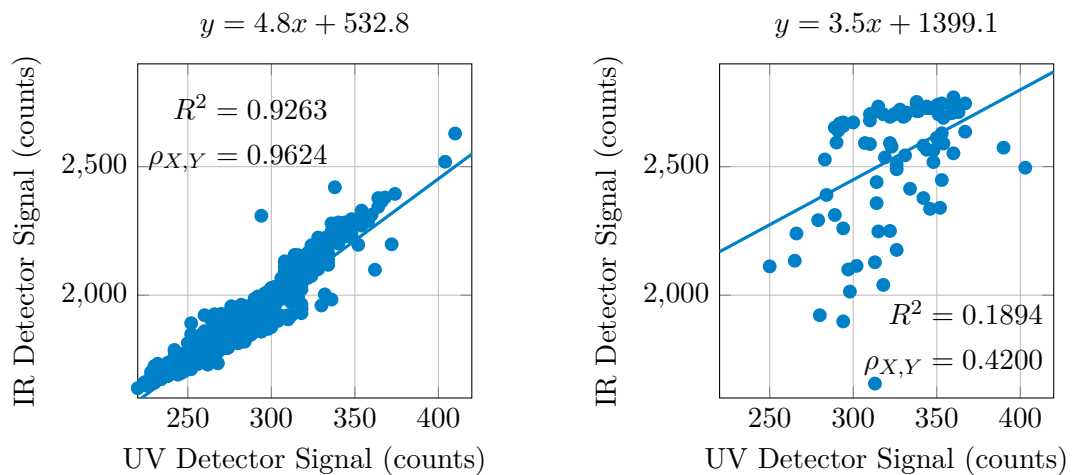
Figure 14.11.: Time series of the monitoring results of the measurement campaign using a sailboat. Shown are the values of the UV and IR transmission measurements as well as water temperature, each measured with a sampling rate of $\frac{1}{30}$ Hz. ① Ferry terminal Rostock Port, ② Crossing area of the fairways Überseehafen, ③ fairway Rostock city ports and Überseehafen, ④ Sea channel, ⑤ Ferry Warnemünde.

The area of the Warnow ferry and the cruise ship terminal at point ③ shows significantly reduced transmission values for both optical channels. The temperature curve also shows a change in the trend at this point. Again, it can be assumed that a change in the water

body will occur as a result of the increased ship traffic. Moreover, it is striking how abrupt the change in the transmission signal for the UV channel occurs. After this area, a relatively homogeneous course of the transmission signal is visible for the UV channel up to the estuary into the Baltic Sea. For the IR channel, a further decrease in the transmission signal occurs in the estuary area.

Figure 14.12 shows the comparison of the transmission measurements of both optical channels during the field campaigns. As shown in Figure 14.12a, the suspicion is confirmed that for the measurements conducted by canoe along the Warnow up to the Unterwarnow the signal component due to turbidity is dominant. This results in an almost direct dependence between the transmission signal of the UV channel and the signal of the IR channel.

In contrast, Figure 14.12b clearly shows that the signal characteristics are independent of each other. This is not least due to the fact that the turbidity during the second measurement campaign was much less pronounced. There are hardly any values below 2000 counts for the selected system setting. But then again the value range for the UV channel is comparable. Here it must be questioned how resilient the approximation actually is in the shown case. As already mentioned, an estimate of the CDOM concentration is not possible or only possible to a limited extent if the turbidity is too high.



(a) Comparison UV and IR transmission values of the campaign using a canoe. (b) Comparison UV and IR transmission values of the campaign using a sailboat.

Figure 14.12.: Comparison of the transmission measurements of both optical channels during the field campaign.

Part VII.

Discussion

15. Discussion

This dissertation investigated the dynamic monitoring of processes in complex ecosystems by using an optical sensor based measurement system.

The dissertation can be subdivided into three fields, which serve as a structure for the discussion. The OSE sampling theorem represents the theoretical basis of this thesis. Based on the OSE sampling theorem and a fundamental consideration of the measurement principle of attenuation (Beer-Lambert-Bouguer Law), a modular optical sensor system was developed and evaluated in detail in laboratory studies. Finally, two exemplary monitoring scenarios were carried out to allow a feasibility analysis of the proposed measurement method.

15.1. Sensing as a Service – The OSE Sampling Theorem

The formulation of the OSE sampling theorem is the result of a fundamental consideration of the scale problem in the context of environmental data collection. In Section 3.1, Section 3.2 and Section 3.3 of this thesis, the temporal as well as the spatial and spatio-temporal aspects are explained using detailed examples. The consequence of this analysis is that in future sensor systems will have to provide information not only in relation to the measured quantity but also with regard to the location and time of the measurement as an internal service. In addition, static monitoring with a constant sampling rate does not sufficiently take into account the temporal component of an environmental state variable. The demand for cross-scale monitoring is therefore primarily an engineering challenge. For the further work within this dissertation, the OSE sampling theorem enabled a unique and innovative approach to the development of the sensor and the sensor system. Therefore, the development of the OSE sampling theorem and its practical implementation in form of the presented measurement system is an essential finding of this dissertation. With the prototype presented in this thesis it is possible to carry out fast measurements and, more important, aggregate them to usable information close to real time, e.g. as real-time map plots or web-based dashboards. The concept of the OSE sampling theorem has already been published by the author of this thesis (Schima et al., 2017).

15.2. Sensor and System Development for an Advanced Monitoring

Due to the explanation of the optical characteristics of water and its measurement as described in Part III of this thesis, the development of every sensor component was driven

by aspects regarding the fundamentals of attenuation measurement. In this context, the requirement was formulated that the sensor system should provide a possibility to be adjustable via software commands. It was also a fact that the sensor system should be considerably smaller than conventional sensors. A further demand was to ensure that the system was watertight as well as to investigate possibilities to create a pressure-tolerant sensor system.

The final design for the sensor system was based on a modular architecture. Therefore, a communication unit, an emitter unit, a detector unit and a pressure and temperature unit form the overall system topology of the sensor probe as described in Chapter 8. Since each module of the sensor probe accommodates differing circuits, the power supply and the communication had to be ensured using a common footprint design. For this purpose, a sandwich structure was used as basic design rule. This allowed to ensure the necessary contacts using board to board connections at the smallest installation space. For the development of the final PCB layouts, the respective circuits were developed first. The circuit boards were manufactured by a service provider. Later on, the boards were assembled by hand and soldered with a reflow procedure using a heated panel in the laboratory. This seems to be sufficient for small prototypical production approaches. For larger quantities it is recommended to use professional manufacturing methods to avoid errors and malfunctioning boards due to heating or soldering failures in the laboratory.

For the construction of the sensor housing, the corresponding components were produced using a 3D printer. The parts produced in this way were very suitable for the outlined application, which represents another key finding of this work. Some studies are being carried out currently that deal with similar approaches and come to similar conclusions for use in marine technology (Phamduy et al., 2017; Mohammed, 2016). An advantage that is not to be neglected is seen in the production of optically transparent components using a 3D printer in combination with translucent filament. The optical windows installed in the sensor are printed from transparent material and represent a promising approach for the future production of optical sensor components, at least for prototyping. This is due to the fact that no additional and costly lenses made of glass are necessary as proofed by the laboratory evaluation.

The interior of the sensor was encapsulated with optical clear polyurethane. The encapsulation ensures that the electronic components are sealed watertight and could also serve to produce a pressure-tolerant system as described in Section 7.2.4. A major challenge in casting is to ensure bubble-free encapsulation. In conventional manufacturing, vacuum is used during the casting process. For the production of the prototype in the laboratory, this was not possible.

Probably the most sensitive part of the entire sensor system is the cable. In the field of marine technology, the topic of underwater cables is frequently discussed and represents a

challenging problem. This work did not explicitly address this issue. A cable was selected on the basis of good experience in limnic applications. Due to a jacket of S-PVC and a corresponding copper shielding inside the cable (see Section 8.3.3), the cable was sufficient for the tests and was used for conducting the field experiments within this thesis. Tests over several days on the artificial reef showed though, that the longitudinal tightness of the cable is not permanently given. For longer deployment times, especially in the brackish waters of the Baltic Sea, cables are recommended that withstand these conditions better. Cables for these applications generally have a more robust cable sheathing and are provided with special fillers inside. Here the disadvantages can be that those kind of cables are stiffer, which can have a negative effect on handling in field and the price is much higher compared to the used cable.

Overall, it can be stated that the developed sensor system is considerably lighter and smaller in relation to the size of the sensor probe than comparable commercially available systems as shown in the comparison in Table A.1. The functional design of the sensor probe and the topside unit has proven to be very practical both for laboratory investigations and during field measurements.

In addition to the development of the sensor hardware, special emphasis was laid on the implementation of service-oriented measuring features based on highly integrated electronics. Therefore, only components were used that allow simple integration into the overall system via the preferred I²C interface as described in Section 7.2.1.

To build an adaptive optical measurement system it was necessary to create an emitter unit that allows to adjust the light intensity, to use different LED's and to guarantee a constant operation even under field conditions. The final design uses an LED driver as described in Section 8.2.2 to precisely regulate the forward current I_{LED} through the used LED's and to modulate the pulse width (PWM) to control the brightness of the LED's. This opens up a multitude of possibilities and provides an unprecedented level of flexibility in sensor configuration in this context. The characterization in the laboratory has shown that the adjustment possibilities via the LED driver are very precise. In addition, the possibility of providing a status monitoring of the LED's is enabled. Thus, it is possible to measure the voltage drop via the LED as well as the supply voltage of the complete system. An analysis showed that both the measurement of the voltages and the constant current control correspond very well with the conducted measurements using a digital multimeter as shown in Figure 11.1 and Figure 11.2.

Given the ability to set both the forward current I_{LED} through the LED and the PWM settings as desired, an essential innovation of the measuring arrangement developed in the context of this work is the possibility to continuously control the intensity of the emitted light with unprecedented flexibility.

In Section 6 an extensive review was made to choose an appropriate wavelength range for the optical approximation of turbidity and the content of CDOM. Wavelengths used in applied research are given in Table 6.1.

For the development of the sensor probe, nominal peak wavelengths of $\lambda_{\text{peak}} = 370 \text{ nm}$ were considered for the determination of CDOM and $\lambda_{\text{peak}} = 860 \text{ nm}$ for the determination of turbidity due to the corresponding references given in Table 6.1.

Once the peak wavelengths had been determined and the corresponding LED's identified, their spectral properties could be examined. Of interest were the effects of the change in the forward current I_{LED} and pulse width modulation (PWM) on the spectral characteristics of the LED's. For this purpose, a spectrometer was used for the investigation. By successively changing the forward current I_{LED} with fixed PWM settings and vice versa, the resulting spectra for both LED's were determined. The results can be seen in Figure 11.8 and Figure 11.6 for the UV LED and for the IR in Figure 11.9 and Figure 11.7. It is conspicuous that the emission spectra of the UV LED show no increase in intensity depending on the current intensity for values greater than $I_{\text{LED}} > 7.5 \text{ mA}$. This coincides with the result of determining the current-voltage characteristic as shown in Figure 11.4. Here it can be seen that no further voltage increase occurs for forward currents greater than $I_{\text{LED}} > 7.5 \text{ mA}$, although this would be expected. The reason for this is that the LED driver is operated with 3.3 V supply voltage. As a result, only this voltage is available for the LED. Although the LED driver has a so-called charge pump, it is not sufficient for the voltage drop via the UV LED, which would be about $U_{\text{LED}(I_{\text{LED}}=25 \text{ mA})} \approx 3.6 \text{ V}$ according to the data sheet. This slightly limits the variability in the intensity control due to the adjustment of the forward current I_{LED} of the UV LED compared to the IR LED. The emission spectra of the IR LED show a significant change in intensity both for variation of the forward current I_{LED} and the PWM settings. What can be generalized is that for both optical channels neither the change of the forward current I_{LED} nor a change in the PWM settings results in a spectral change, e.g. a differing peak wavelength, which is an important finding for the planned application.

Based on these findings and the fact that different intensities can be achieved with the emitter unit, it is possible to set up an adaptive measurement system. Therefore, investigations were carried out in the laboratory to show how the measuring range can be adapted. For this purpose, the sensor was positioned in clear tap water and the forward current I_{LED} and PWM settings for both optical channels were gradually changed and the corresponding detector signals were recorded. Figure 11.10 shows the results of this investigation for the UV channel, whereas the results for the IR channel are shown in Figure 11.11. Figure 11.10 shows again that the change of the forward current I_{LED} of the UV LED leads to a lower dynamic of the intensity. Independently of this, the results confirm that an intensity range can be defined first by selecting the forward current I_{LED} ,

and then varied from 0% . . . 100% intensity by pulse width modulation. This intensity modulation and the resulting detector values can be interpreted as a calibration of the measuring range. With the present sensor system it is therefore possible to calibrate the entire measuring range, independent of further means. In order to illustrate this aspect, Figure 11.12 and Figure 11.13 show the detector signals of both optical channels for selected forward currents I_{LED} and changes of the PWM setting. Again, the limitation of the UV channel due to the low supply voltage becomes clear, since the measured values for currents greater than 10 mA cannot be distinguished from each other as it can be seen in Figure 11.12. The signal curve of the IR channel showed a higher scattering compared to the UV channel. A reason could be that due to the larger value range as a result of the higher luminous efficacy, small fluctuations in the constant current control or the PWM signal generation show stronger effects than for the comparatively small value range of the UV channel.

Nevertheless, it becomes clear that the intensity modulation series could serve as reference values for calibration purpose or for an adaptive measurement of different water conditions for example. Consequently, the intensity of the incident radiation could be increased for water samples with high absorption in order to improve the resolution of the measurement. Therefore, the added value of the developments presented in this dissertation is highlighted by the fact that the technological prerequisites were achieved to investigate the possibilities of a dynamic monitoring due to measurement range adaptation.

In order to characterize the overall system, the basic measurement noise of both optical channels at rest is important. In this connection, the analysis of the signal-to-noise ratio provides indications about the expected resolution of the sensor and also about the resulting measurement range. For this purpose, the sensor system was installed in a large water reservoir filled with clear tap water and darkened for several hours to accomplish stable conditions. To analyze the stability of the measurement signal, a time series of 60 min was recorded with a sampling rate of 0.1 Hz. The presentation of the results in Figure 11.14 shows that both channels scatter, but do not follow a global trend. Moreover, the distributions of the values were analyzed and displayed as histograms. This form of representation revealed that the detector signal of the UV channel has a right-skewed distribution. The signals of the IR channel, on the other hand, are normally distributed. The temperature can also be assumed to be approximately constant during the experiment, with a decrease of 0.15 °C. With regard to the standard deviation of the detector without considering the measuring range, both channels are comparable. Here, the UV detector shows even a lower standard deviation. Compared to the average value of the detector readings, it can be said that the signal uncertainty for the UV channel is about $\pm 1.2\%$ and for the IR channel even less $< \pm 0.09\%$. The major difference can be seen in the

varying luminous efficacy of the settings selected in the experiment, so that less light hits the UV detector. The fact that the measuring range of the UV detector is not adequately covered leads to a higher percentage of measurement uncertainty than with the IR channel.

When considering an in-situ sensor in the field of ocean engineering, the pressure stability as well as the influence of the ambient pressure on the measuring system are important factors. This concerns both the system stability with regard to mechanical loads and the influencing variables on the quality of the measurement results. For this purpose, laboratory tests were carried out in a pressure tank. In Section 12.1 the results are presented. Figure 12.1 and Figure 12.2 show the course of the UV and IR detector signals plotted over the ambient pressure up to a maximum pressure of $p_{\max} = 37$ bar. As the cable length of the system is limited to about 250 m, an investigation of the system behavior under higher ambient pressures was not carried out within the scope of this work. However, for better comparability, the values were normalized to the detector signal under atmospheric pressure. In the diagram, the ranges of $\pm 2.5\%$ and $\pm 5\%$ deviation are indicated in color. The analysis revealed that for both optical channels the deviation was below $< 5\%$ under pressure load. Since the majority of the values are also significantly below $< 2.5\%$ deviation, the pressure influence can be neglected for most applications.

The influence of a varying temperature is a particular challenge for many measurement systems, especially for measurements carried out under field conditions. For this reason, the influence of temperature on the measurement quality of the sensor was investigated in laboratory tests. Figure 12.3 shows the course of the transmission signal of the UV channel plotted against the board temperature of the detector unit. The linear fit of the data has a slope of $R^2 = 0.9899$ and a strong linear correlation coefficient of $\rho_{X,Y} = 0.9949$. The UV detector signal is therefore strongly temperature-dependent. However, the fact that the course is linear, offers the possibility to compensate the temperature by linear regression. If $\vartheta_{PCB} = 20^\circ\text{C}$ is selected as the reference point, the rate of change corresponds to a value of $3.22\% \text{K}^{-1}$. The analysis of the IR channel revealed a similar result. Figure 12.4 shows the course of the transmission signal of the IR channel plotted against the board temperature of the detector unit. In this case, the linear fit of the data has a slope of $R^2 = 0.9300$ and a linear correlation coefficient of $\rho_{X,Y} = 0.9643$. It is noticeable that the measured values show a stronger deviation than with the UV channel. Particularly in the lower temperature range $\vartheta_{PCB} < 14^\circ\text{C}$, there is an increase in deviating measured values from the linear trend. Due to the large number of measured values ($N=4885$), it can be assumed that the temperature characteristic curve of the IR channel determined in this way can be used to ensure sufficient temperature compensation. If a reference point of $\vartheta_{PCB} = 20^\circ\text{C}$ is also assumed here, a rate of change of $0.38\% \text{K}^{-1}$ results. The rate is thus considerably lower than the change rate of the UV channel. This is due to the fact

that the measuring range is larger as well as the correspondingly higher available luminous efficacy for the IR range.

The most important criterion for the later application of the in-situ measurement system is the comparability of the measurement with established laboratory standard methods. For this reason, two test series were set up to compare the quality of the measurement of both optical channels with a laboratory photometer and thus validate it as described in Chapter 13.

It is apparent from the data shown in Figure 13.1 that the transmission measurements $\Phi_t(\lambda = 370 \text{ nm})$ followed a linear trend, which validates the measurements reported by the sensor probe compared to the measured transmittance $T_{(\lambda=370 \text{ nm})}$ values derived from the laboratory photometer. The linear fit of the data has a slope of $R^2 = 0.9440$ and a linear correlation coefficient of $\rho_{X,Y} = 0.9716$. The course of the measuring points shows a stronger deviation from the linear trend line for water samples of lower CDOM concentrations (low transmission rates $< 20\%$ reported by the laboratory photometer). It is assumed that in this range the detector of the laboratory photometer shows a higher deviation leading to this perceptible difference. However, the results confirm that the measurement system is suitable for measuring transmission or attenuation in an adequate manner and with sufficient accuracy, e.g. for approximation of the CDOM concentration.

An even stronger correlation was observed by comparing the results of the transmission measurement of the IR channel of the sensor and the determination of turbidity in FAU using a laboratory photometer as shown in Figure 13.2. Again, the deviation of the measured values seems to increase with decreasing turbidity. However, the linear fit of the data has a slope of $R^2 = 0.9672$ and a linear correlation coefficient of $\rho_{X,Y} = -0.9805$. The negative sign is due to the fact that the transmission values of the sensor were plotted against the (processed) results of the turbidity measurement of the photometer. In this case, high transmission values of the sensor correspond to low turbidity values, since a higher amount of light can penetrate the water sample.

For both optical channels, the detector saturation was not reached. This shows that much larger measuring ranges are possible for both channels. For the UV channel, the measuring range under the selected conditions is two times as large as the range that can be covered by the laboratory photometer. With an approximately 1.5 larger measuring range, the IR channel behaves similarly.

In this context it should also be mentioned that by increasing the integration time on the detector side of the sensor system, the resolution can be increased. For example, if the integration time is doubled, the resolution can be increased twice. However, the time required for a measurement is limited. Table 9.1 shows the available integration times. The maximum for the UV channel is $t_i = 1000 \text{ ms}$ and for the IR channel $t_i = 402 \text{ ms}$ which leads to the conclusion that an integration time of $t_i = 1000 \text{ ms}$ would have

the disadvantage of strongly falsifying the measured value due to sensor movement or movement of the medium itself.

15.3. Case Study as Proof of Concept Analysis

The case study revealed that the presented method provides a suitable and promising approach for a fast in-situ monitoring of aquatic environments. It was shown that the measuring system can be mounted on smaller boats such as canoes or sailboats in order to allow monitoring of areas that are not covered by conventional monitoring programs or only to a limited extent (see Section 14.3). This is of particular importance for the selected use case, since the Baltic Sea as a marginal sea is strongly influenced by the surrounding catchment area (HELCOM, 2018). The input of nutrients and CDOM via the rivers as well as the limited exchange with saline, oxygen rich water from the North Sea via the Skagerrak are creating challenging and very unique conditions for the Baltic Sea (Kreus et al., 2015). This leads to an increased concentration of nutrients and CDOM in the Baltic Sea (Fleming-Lehtinen et al., 2015; Lindh et al., 2015; Seidel et al., 2017). Especially in warm summers this results in a risk of eutrophication and so called dead zones where all dissolved oxygen is consumed.

In this connection, the previously discussed OSE sampling theorem can be confirmed again since the sensor system automatically provides all the necessary data for a real time assessment of the monitoring results, e.g. as an online map view. Considering this situation, it becomes clear why future monitoring approaches have to deal with the environmental conditions in the river estuaries, river courses and finally the situation in the catchment areas in much more detail. In the use case, this challenge was addressed by a monitoring approach based on the sensor system prototype developed within this thesis.

In the first application by canoe it became clear that the area of the Warnow between Mühlendammschleuse and Unterwarwnow (former Neptun shipyard) showed a high dynamic. But a closer look at the results of the transmission measurement revealed that for both optical channels, as shown in Figure 14.5 and 14.6, a global trend can be observed. This is demonstrated by the comparison of the transmission measurements of both optical channels as shown in Figure 14.12a. It must be assumed that the prevailing turbidity value during the measurement campaign has exceeded a critical point. In any case, the optical signal attenuation due to the turbidity superimposed the absorption measurement on the CDOM approximation.

The evaluation of the results of the second measurement campaign using a sailboat revealed a different result. As it can be seen in Figure 14.9 and Figure 14.10, clear deviations between the signal characteristics of the transmission measurement of the UV and IR channels can be detected. The comparison of the signal characteristics of the transmission measurement of the optical channels as shown in Figure 14.12 illustrates this as well. It should be mentioned though, that in the second campaign the transmission

signal of the IR channel as shown in Figure 14.11 is predominantly larger than in the first campaign (see Figure 14.7). This can be interpreted as an indication that there was generally less turbidity during the second measurement campaign.

Overall, it can be stated that the measurement system is fundamentally suitable for fast monitoring of complex areas and ecosystems. Particularly noteworthy is the very low methodological effort during field measurement and the rapid provision of monitoring results as actionable information, e.g. in the form of web-based visualizations, as demonstrated with the use case.

Part VIII.

Conclusion and Outlook

16. Conclusion

This thesis describes the development, construction and the application of a sensor probe (attenuometer) as part of an adaptive measuring system for a fast in-situ monitoring of optical properties in aquatic environments. Two target wavelengths were used to optically approximate the content of chromophoric dissolved organic matter (CDOM) and turbidity ($\lambda_{\text{CDOM}} = 370 \text{ nm}$, $\lambda_{\text{Turbidity}} = 850 \text{ nm}$). All investigations and developments carried out in the context of this thesis can be transferred to other wavelengths. In addition to the detection of further water constituents, this opens up the possibility of recording entire absorption spectra in the form of a miniaturized multi-parameter probe in the future.

In addition to the sensor and system development, the introduction of a holistic sampling theorem (OSE) is an essential component of this thesis (Schima et al., 2017). Due to the combination of the monitoring paradigm and the consequent sensor development from the beginning of the design process, a unprecedented measurement system regarding its functionality was achieved. Integrated functions for controlling the emitter intensity by changing the forward current or pulse width modulation as well as the adjustable detector sensitivity due to changes in the integration time enable sophisticated features such as auto calibration routines or an adaptive system behavior. Therefore, this thesis describes the structure of a modular and adaptive optical sensor concept that opens the possibility for a fast and service-oriented environmental monitoring.

In order to verify the measuring quality, a detailed investigation of the system components with regard to the electronic and optoelectronic properties was carried out. Furthermore, the pressure and temperature dependence were examined and the repeatability of the measurement was determined in laboratory studies. In addition, a comparative investigation proved that the presented sensor system provides results that are in accordance with the laboratory analytical standard method using a laboratory photometer. Thus, the measurement quality is considered acceptable for the proposed application. On the basis of a case study of two mobile monitoring campaigns on the Warnow river along the city of Rostock, the feasibility was demonstrated and the added value of the OSE sampling theorem was proven.

The results confirm that the sensor system prototype represents a promising approach that meets the requirements and specifications outlined in the introduction of this thesis. Therefore, the sensor system provides a fast and useful method to assist and improve future environmental monitoring applications especially for the investigation of areas, which are not yet accessible by common monitoring technologies.

17. Outlook

The findings generated in the context of this thesis also serve as a basis for further studies. In the following, a brief outline will be given where links to other research topics can be found and what concrete further work is planned.

17.1. Predictive Monitoring - Towards Data-Driven Research in Environmental Sciences

Within the last decades, a new system theoretical approach in the field of environmental monitoring has evolved (Wiemann et al., 2017). Thanks to more powerful and less expensive electronic components as well as increasing digitalisation, sensors and monitoring systems will be used to a greater extent and thus monitoring will be more intensively taken into account in the development of models. The major advantage is not necessarily the fast provision of data, but the aggregation of context information into a holistic system description. Figure 17.1 shows the increase in the information value of data with regard to the processing steps in environmental research.

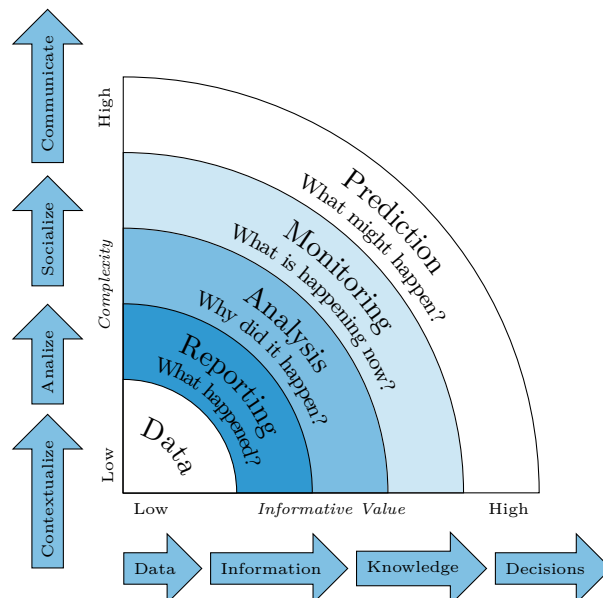


Figure 17.1.: The value of data (adapted from Eckerson (2007)). With the aggregation of descriptive information, the value of measurement data can be significantly increased. In the same way, the effort for data collection also increases.

It can be assumed, that the challenge regarding the development of sensors and monitoring systems of the future relies on the ability to react to additional information describing the context in an appropriate manner. These can be physical parameters but also situational data, e.g. the description of a certain process. In the same way, the computational effort and also the measurement complexity to derive reliable and thus useful information from a single measurement are increasing. Due to the holistic OSE sampling theorem, the method developed in the context of this thesis can provide an appropriate data basis of highly described sensor readings for this very approach.

17.2. A Fast Data Evaluation for Decision Making

The number of sensors used in environmental monitoring is increasing, but efficient strategies to generate useful information from the increasing amount of data are missing. To help accelerating decision-making processes, engineering solutions are needed to capture processes in a targeted manner as described in Section 4.1 of this thesis. In the domain of information technologies and data processing a structural approach, the lambda architecture, has become increasingly established (Kiran et al., 2015; Villari et al., 2014; Fernández et al., 2016). The lambda architecture is a data processing architecture designed to process large amounts of data using both batch and stream processing methods. Therefore, the lambda architecture can be of great benefit especially in the case of sensor-based environmental research. An adaption for the environmental monitoring use case is given in Figure 17.2 below.

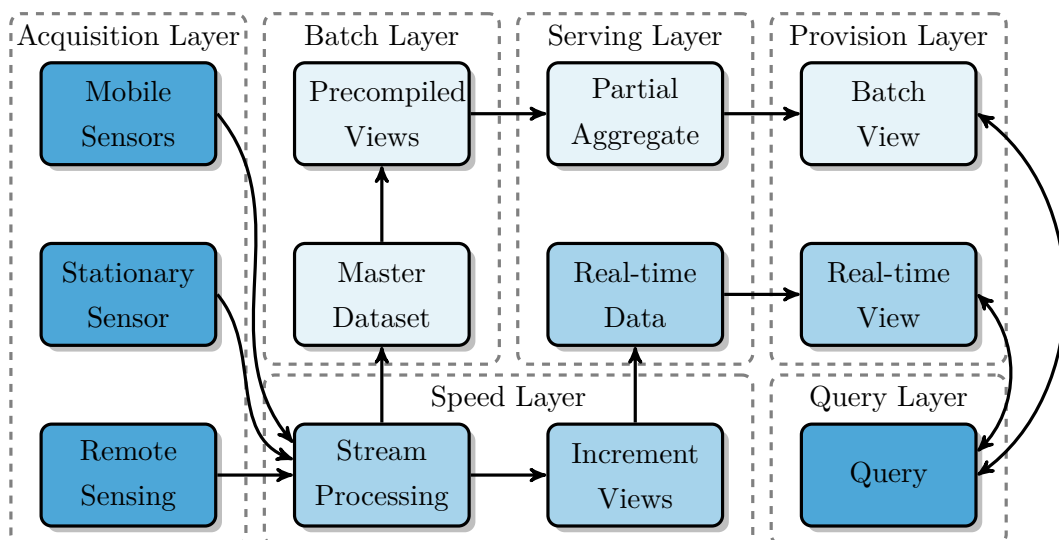


Figure 17.2.: Lambda architecture for data acquisition and data evaluation.

Starting from a data acquisition layer, sensor data are streamed to a rough but fast evaluation process (speed layer) and a computation-intensive processing (batch layer). The advantage consists in the fact that the results of both processing methods are made

available to a central query layer via a serving and provision layer. As a result, queries can be processed very quickly allowing a first approximation of even complex system states.

A significant contribution to this approach is seen in the presented OSE sampling theorem and post-processing, which allows to support, to simplify and to accelerate complex decision-making processes by providing highly specific information close to real-time. This paves the way for the increased use of artificial intelligence methods in the development and testing of monitoring strategies in the future.

17.3. Future Work

In addition to system-theoretical approaches for an advanced environmental monitoring, improvements of the presented sensor system and pending investigation are aspired as well. Therefore, future work should focus on topics that were not investigated in detail within the scope of this thesis. These include in particular studies on biofouling and methods to avoid it. First investigations at the artificial reef in Nienhagen showed promising results, but larger test series and scientific evaluation are still pending.

The influence of scattered light effects on the measurement quality should also be investigated separately in further studies. Since the optical windows of the sensor were 3D-printed with transparent filament, it is recommended to investigate the light absorption of the filament material as well as the refraction in detail. Possibilities to adjust the beam width for the measuring application should also be considered in future studies.

Another aspect regarding the sensor probe is that the light path is not colimated since no lens or particular optic was placed in front of the emitter due to the requirement of the simplification of the sensor set up. Further studies should consider to investigate suitable approaches to overcome this lack, perhaps by using 3D printed optics.

Within this thesis, the application depth of the measuring system prototype was confirmed in laboratory tests up to 37 bar ambient pressure without signal loss or damage of the system. Tests to determine the maximum possible deployment depth will therefore be the subject of future investigations. It should also be clarified whether the entire sensor can be designed as a pressure tolerant system (PTS).

For longer operating times, suitable cables with sufficient longitudinal tightness and strength need to be tested. Particular care must be taken to ensure that weight, manageability and, last but not least, costs are balanced.

Future work should also focus on the sampling strategy. This includes suitable methods which are appropriate to react to different or changing environmental conditions and to autonomously adapt the measuring range. In the context of this work the necessary tools have been developed and demonstrated. However, the implementation into an autonomous control system is the subject of further studies.

Based on the findings and developments of this thesis, a project idea was developed which was approved for funding within the framework of the PhotonicSensing Initiative of the Photonics Based Sensing ERA-NET Cofund (13N14733). The international project entitled *Development and Evaluation of Photonic Sensor Components for Coastal Environmental Monitoring and Assessment of Marine Resources* (DEEP-SEA) aims to transfer photonic sensing methods into applied fisheries science and oceanographic research. The international project consortium coordinated by the Chair of Ocean Engineering of the University of Rostock set the goal of developing a prototype of an optical sensor platform for applied research, which can be understood as a continuation of the technological approach developed within the framework of this thesis.

In cooperation with the Helmholtz Centre Geesthacht, a sensor system will be installed at a sampling site in Cuxhaven, Germany, where a stationary ferry box is located. At the sampling site, water from the Elbe river is continuously pumped and monitored by sensors inside the ferry box and additional laboratory analysis at regular intervals. This offers the possibility to test the measuring system with regard to its basic suitability and to investigate the comparability of the measurement results of the sensor system with those of the ferry box and the laboratory analysis.

Bibliography

- Barnes, H. E. and Gennari, J. J. A Review of Pressure-Tolerant Electronics (PTE). Technical Report NRL-MR-3317, Naval Research Lab Washington DC, 1976. URL: <http://www.dtic.mil/docs/citations/ADA027967>.
- Bass, M., Van Stryland, E., Williams, D. R., and Wolfe, W. L., editors. *Handbook of Optics, Volume I: Fundamentals, Techniques, and Design*. vol. 1. McGraw-Hill, Inc., New York, NY, USA, 2. edition, 1995. ISBN 0-07-047740-7.
- Chapman, D., editor. *Water Quality Assessments - A Guide to Use of Biota, Sediments and Water in Environmental Monitoring*. E & FN Spon, London, UK, 2. edition, 1996. ISBN 978-0-419-21590-5.
- Christ, R. D. and Wernli, R. L. *The ROV manual: a user guide for remotely operated vehicles*. Elsevier, Amsterdam, 2014. ISBN 978-0-08-098288-5.
- Das, S., Das, I., Giri, S., Chanda, A., Maity, S., Lotliker, A. A., Kumar, T. S., Akhand, A., and Hazra, S. Chromophoric dissolved organic matter (CDOM) variability over the continental shelf of the northern Bay of Bengal. *Oceanologia*, 59(3):271–282, 2017. ISSN 0078-3234. doi: 10.1016/j.oceano.2017.03.002. URL: <http://www.sciencedirect.com/science/article/pii/S0078323417300210>.
- DIN 38404-3. Deutsche Einheitsverfahren zur Wasser-, Abwasser- und Schlammuntersuchung - Physikalische und physikalisch-chemische Kenngrößen (Gruppe C) - Teil 3: Bestimmung der Absorption im Bereich der UV-Strahlung, Spektraler Absorptionskoeffizient (C 3), 2005. URL: <https://www.beuth.de/de/norm/din-38404-3/81046719>.
- DIN EN ISO 7027. Wasserbeschaffenheit - Bestimmung der Trübung, 2000. URL: <https://www.beuth.de/de/norm/din-en-iso-7027-1/245621388>.
- D'Sa, E. J. and Kim, H.-c. Surface Gradients in Dissolved Organic Matter Absorption and Fluorescence Properties along the New Zealand Sector of the Southern Ocean. *Frontiers in Marine Science*, 4, 2017. ISSN 2296-7745. doi: 10.3389/fmars.2017.00021. URL: <https://www.frontiersin.org/articles/10.3389/fmars.2017.00021/full>.
- Eckerson, W. W. Predictive analytics. *"Extending the Value of Your Data Warehousing Investment"*. TDWI Best Practices Report, 1:1–36, 2007.

- Fernández, P., Santana, J., Ortega, S., Trujillo, A., Suárez, J., Domínguez, C., Santana, J., Sánchez, A., Fernández, P., Santana, J. M., Ortega, S., Trujillo, A., Suárez, J. P., Domínguez, C., Santana, J., and Sánchez, A. SmartPort: A Platform for Sensor Data Monitoring in a Seaport Based on FIWARE. *Sensors*, 16(3):417, 2016. doi: 10.3390/s16030417. URL: <https://www.mdpi.com/1424-8220/16/3/417>.
- Fleming-Lehtinen, V., Räike, A., Kortelainen, P., Kauppila, P., and Thomas, D. N. Organic Carbon Concentration in the Northern Coastal Baltic Sea between 1975 and 2011. *Estuaries and Coasts*, 38(2):466–481, 2015. ISSN 1559-2723, 1559-2731. doi: 10.1007/s12237-014-9829-y. URL: <http://link.springer.com/10.1007/s12237-014-9829-y>.
- Green, S. A. and Blough, N. V. Optical absorption and fluorescence properties of chromophoric dissolved organic matter in natural waters. *Limnology and Oceanography*, 39(8):1903–1916, 1994. ISSN 00243590. doi: 10.4319/lo.1994.39.8.1903. URL: <http://doi.wiley.com/10.4319/lo.1994.39.8.1903>.
- Harvey, E. T., Kratzer, S., and Andersson, A. Relationships between colored dissolved organic matter and dissolved organic carbon in different coastal gradients of the Baltic Sea. *AMBIO*, 44(3):392–401, 2015. ISSN 0044-7447, 1654-7209. doi: 10.1007/s13280-015-0658-4. URL: <https://link.springer.com/article/10.1007/s13280-015-0658-4>.
- HELCOM. Sources and pathways of nutrients to the Baltic Sea. Technical Report 153, Baltic Marine Environment Protection Commission, Helsinki, Finland, 2018. URL: <http://www.helcom.fi/Lists/Publications/BSEP153.pdf>.
- Hoge, F. E., Vodacek, A., Swift, R. N., Yungel, J. K., and Blough, N. V. Inherent optical properties of the ocean: retrieval of the absorption coefficient of chromophoric dissolved organic matter from airborne laser spectral fluorescence measurements. *Applied optics*, 34(30):7032–7038, 1995.
- Hussain, I., Ahamad, K., and Nath, P. Water turbidity sensing using a smartphone. *RSC Advances*, 6(27):22374–22382, 2016. ISSN 2046-2069. doi: 10.1039/C6RA02483A. URL: <http://xlink.rsc.org/?DOI=C6RA02483A>.
- Isoyama, R., Taie, M., Kageyama, T., Miura, M., Maeda, A., Mori, A., and Lee, S.-S. A Feasibility Study on the Simultaneous Sensing of Turbidity and Chlorophyll a Concentration Using a Simple Optical Measurement Method. *Micromachines*, 8(4):112, 2017. doi: 10.3390/mi8040112. URL: <http://www.mdpi.com/2072-666X/8/4/112>.
- Jerri, A. J. The Shannon sampling theorem #8212; Its various extensions and applications:

- A tutorial review. *Proceedings of the IEEE*, 65(11):1565–1596, 1977. ISSN 0018-9219. doi: 10.1109/PROC.1977.10771.
- Johannessen, S. C., Miller, W.L., and Cullen, J.J. Calculation of UV attenuation and colored dissolved organic matter absorption spectra from measurements of ocean color. *Journal of Geophysical Research*, 108(C9):1–13, 2003. ISSN 0148-0227. doi: 10.1029/2000JC000514. URL: <http://doi.wiley.com/10.1029/2000JC000514>.
- Joshi, I. D., D’Sa, E. J., Osburn, C. L., Bianchi, T. S., Ko, D. S., Oviedo-Vargas, D., Arellano, A. R., and Ward, N. D. Assessing chromophoric dissolved organic matter (CDOM) distribution, stocks, and fluxes in Apalachicola Bay using combined field, VIIRS ocean color, and model observations. *Remote Sensing of Environment*, 191:359–372, 2017. ISSN 00344257. doi: 10.1016/j.rse.2017.01.039. URL: <https://linkinghub.elsevier.com/retrieve/pii/S0034425717300457>.
- Kampmann, P., Lemburg, J., Hanff, H., and Kirchner, F. Hybrid pressure-tolerant electronics. In *2012 Oceans*, pages 1–5, 2012. doi: 10.1109/OCEANS.2012.6404828.
- Kang, W., Du, R., and Liu, G. Dual-Domain Compressed Sensing Method for Oceanic Environmental Elements Collection with Underwater Sensor Networks. *Mobile Networks and Applications*, pages 1–13, 2017. ISSN 1383-469X, 1572-8153. doi: 10.1007/s11036-017-0947-1. URL: <https://link.springer.com/article/10.1007/s11036-017-0947-1>.
- Kheireddine, M., Ouhssain, M., Calleja, M. L., Morán, X. A. G., Sarma, Y. V. B., Tiwari, S. P., and Jones, B. H. Characterization of light absorption by chromophoric dissolved organic matter (CDOM) in the upper layer of the Red Sea. *Deep Sea Research Part I: Oceanographic Research Papers*, 133:72–84, 2018. ISSN 0967-0637. doi: 10.1016/j.dsr.2018.02.001. URL: <http://www.sciencedirect.com/science/article/pii/S0967063717301000>.
- Kiran, M., Murphy, P., Monga, I., Dugan, J., and Baveja, S. S. Lambda architecture for cost-effective batch and speed big data processing. In *2015 IEEE International Conference on Big Data (Big Data)*, pages 2785–2792, 2015. doi: 10.1109/BigData.2015.7364082.
- Kirk, J. T. O. *Light and Photosynthesis in Aquatic Ecosystems*. Cambridge University Press, 1994. ISBN 978-0-521-45966-2.
- Kolka, R., Weishampel, P., and Fröberg, M. Measurement and importance of dissolved organic carbon. *Field measurements for forest carbon monitoring*, pages 171–176, 2008. URL: <http://link.springer.com/content/pdf/10.1007/978-1-4020-8506-2.pdf>.

- Kreus, M., Schartau, M., Engel, A., Nausch, M., and Voss, M. Variations in the elemental ratio of organic matter in the central Baltic Sea: Part I—Linking primary production to remineralization. *Continental Shelf Research*, 100:25–45, 2015. ISSN 0278-4343. doi: 10.1016/j.csr.2014.06.015. URL: <http://www.sciencedirect.com/science/article/pii/S0278434314002313>.
- Kreuzer, E. and Solowjow, E. Learning environmental fields with micro underwater vehicles: a path integral—Gaussian Markov random field approach. *Autonomous Robots*, 42(4):761–780, 2018. ISSN 0929-5593, 1573-7527. doi: 10.1007/s10514-017-9685-2. URL: <http://link.springer.com/10.1007/s10514-017-9685-2>.
- Lindh, M. V., Lefébure, R., Degerman, R., Lundin, D., Andersson, A., and Pinhassi, J. Consequences of increased terrestrial dissolved organic matter and temperature on bacterioplankton community composition during a Baltic Sea mesocosm experiment. *AMBIO*, 44(3):402–412, 2015. ISSN 0044-7447, 1654-7209. doi: 10.1007/s13280-015-0659-3. URL: <https://link.springer.com/article/10.1007/s13280-015-0659-3>.
- Lübben, A., Dellwig, O., Koch, S., Beck, M., Badewien, T. H., Fischer, S., and Reuter, R. Distributions and characteristics of dissolved organic matter in temperate coastal waters (Southern North Sea). *Ocean Dynamics*, 59(2):263–275, 2009. ISSN 1616-7341, 1616-7228. doi: 10.1007/s10236-009-0181-x. URL: <http://link.springer.com/10.1007/s10236-009-0181-x>.
- McBride, L. R. and Scholfield, J. T. Solid-State Pressure-Tolerant Illumination for MBARI’s Underwater Low-Light Imaging System. *Journal of Display Technology*, 3(2):149–154, 2007. ISSN 1551-319X. doi: 10.1109/JDT.2007.895344.
- Meler, J., Kowalczyk, P., Ostrowska, M., Ficek, D., Zabłocka, M., and Zdun, A. Parameterization of the light absorption properties of chromophoric dissolved organic matter in the Baltic Sea and Pomeranian lakes. *Ocean Science*, 12(4):1013–1032, 2016. ISSN 1812-0792. doi: 10.5194/os-12-1013-2016. URL: <https://www.ocean-sci.net/12/1013/2016/>.
- Miller, R. L., Belz, M., Castillo, C. D., and Trzaska, R. Determining CDOM absorption spectra in diverse coastal environments using a multiple pathlength, liquid core waveguide system. *Continental Shelf Research*, 22(9):1301–1310, 2002. ISSN 0278-4343. doi: 10.1016/S0278-4343(02)00009-2. URL: <http://www.sciencedirect.com/science/article/pii/S0278434302000092>.
- Mobley, C. D. Optical Properties of Water. In Bass, M., Van Stryland, E. W., Williams, D. R., and Wolfe, W. L., editors, *Handbook of Optics, Volume I: Fundamentals, Techniques, and Design*, vol. 1, pages 43.3–43.56. McGraw-Hill, Inc., 2. edition, 1995.

- Mohammed, J. S. Applications of 3d printing technologies in oceanography. *Methods in Oceanography*, 17:97–117, 2016. ISSN 22111220. doi: 10.1016/j.mio.2016.08.001. URL: <http://linkinghub.elsevier.com/retrieve/pii/S2211122016300093>.
- Moore, C., Barnard, A., Fietzek, P., Lewis, M. R., Sosik, H. M., White, S., and Zielinski, O. Optical tools for ocean monitoring and research. *Ocean Sci.*, 5(4):661–684, 2009. ISSN 1812-0792. doi: 10.5194/os-5-661-2009. URL: <https://www.ocean-sci.net/5/661/2009/>.
- Mostofa, K. M., Yoshioka, T., Mottaleb, A., and Vione, D., editors. *Photobiogeochemistry of Organic Matter*. Environmental Science and Engineering. Springer Berlin Heidelberg, Berlin, Heidelberg, 2013. ISBN 978-3-642-32222-8 978-3-642-32223-5. URL: <http://link.springer.com/10.1007/978-3-642-32223-5>.
- Murphy, K., Heery, B., Sullivan, T., Zhang, D., Paludetti, L., Lau, K. T., Diamond, D., Costa, E., O'Connor, N., and Regan, F. A low-cost autonomous optical sensor for water quality monitoring. *Talanta*, 132:520–527, 2015a. ISSN 00399140. doi: 10.1016/j.talanta.2014.09.045. URL: <http://linkinghub.elsevier.com/retrieve/pii/S0039914014008236>.
- Murphy, K., Sullivan, T., Heery, B., and Regan, F. Data analysis from a low-cost optical sensor for continuous marine monitoring. *Sensors and Actuators B: Chemical*, 214(Supplement C):211–217, 2015b. ISSN 0925-4005. doi: 10.1016/j.snb.2015.02.023. URL: <http://www.sciencedirect.com/science/article/pii/S0925400515001859>.
- Nelson, N. B. and Siegel, D. A. Chapter 11 - Chromophoric DOM in the Open Ocean. In Hansell, D. A. and Carlson, C. A., editors, *Biogeochemistry of Marine Dissolved Organic Matter*, pages 547–578. Academic Press, San Diego, 2002. ISBN 978-0-12-323841-2. doi: 10.1016/B978-012323841-2/50013-0. URL: <http://www.sciencedirect.com/science/article/pii/B9780123238412500130>.
- Niu, C., Zhang, Y., Zhou, Y., Shi, K., Liu, X., and Qin, B. The Potential Applications of Real-Time Monitoring of Water Quality in a Large Shallow Lake (Lake Taihu, China) Using a Chromophoric Dissolved Organic Matter Fluorescence Sensor. *Sensors (Basel, Switzerland)*, 14(7):11580–11594, 2014. ISSN 1424-8220. doi: 10.3390/s140711580. URL: <https://www.ncbi.nlm.nih.gov/pmc/articles/PMC4168458/>.
- OECD. *The ocean economy in 2030*. OECD Publishing, Paris, 2016. ISBN 978-92-64-25171-7.
- Ozaki, Y. and Kawata, S., editors. *Far- and deep-ultraviolet spectroscopy*. Springer, Tokyo, 2015. ISBN 978-4-431-55548-3.

- Phamduy, P., Vazquez, M. A., Kim, C., Mwaffo, V., Rizzo, A., and Porfiri, M. Design and characterization of a miniature free-swimming robotic fish based on multi-material 3d printing. *International Journal of Intelligent Robotics and Applications*, 1(2):209–223, 2017. ISSN 2366-5971, 2366-598X. doi: 10.1007/s41315-017-0012-z. URL: <https://link.springer.com/article/10.1007/s41315-017-0012-z>.
- Preisendorfer, R. W. Hydrologic Optics. Volume 1. Introduction. Technical Report, Honolulu : U.S. Dept. of Commerce, National Oceanic and Atmospheric Administration, Environmental Research Laboratories, Pacific Marine Environmental Laboratory, 1976. URL: <http://udspace.udel.edu/handle/19716/1577>.
- Prien, R.-D. *Entwicklung und Aufbau eines lichtoptischen Kurzstrecken-Attenuationsmessgerätes mit einer In-situ-Kalibriermöglichkeit durch Veränderung der Messstreckenlänge*. Shaker, Aachen, Germany, 1999. ISBN 978-3-8265-4722-5.
- Röttgers, R. and Doerffer, R. Measurements of optical absorption by chromophoric dissolved organic matter using a point-source integrating-cavity absorption meter. *Limnology and Oceanography: Methods*, 5(5):126–135, 2007. ISSN 1541-5856. doi: 10.4319/lom.2007.5.126. URL: <http://onlinelibrary.wiley.com/doi/10.4319/lom.2007.5.126/abstract>.
- Schima, R., Goblirsch, T., Salbach, C., Franczyk, B., Aleithe, M., Bumberger, J., and Dietrich, P. Research in Progress: Implementation of an Integrated Data Model for an Improved Monitoring of Environmental Processes. In *Business Information Systems Workshops*, Lecture Notes in Business Information Processing, pages 332–339. Springer, Cham, 2017. ISBN 978-3-319-52463-4 978-3-319-52464-1. doi: 10.1007/978-3-319-52464-1_30.
- Seidel, M., Manecki, M., Herlemann, D. P. R., Deutsch, B., Schulz-Bull, D., Jürgens, K., and Dittmar, T. Composition and Transformation of Dissolved Organic Matter in the Baltic Sea. *Frontiers in Earth Science*, 5, 2017. ISSN 2296-6463. doi: 10.3389/feart.2017.00031. URL: <https://www.frontiersin.org/articles/10.3389/feart.2017.00031/full>.
- Thiede, C., Buscher, M., Luck, M., Lehr, H., Korner, G., Martin, J., Schlichting, M., Krueger, S., and Huth, H. An overall pressure tolerant underwater vehicle: DNS Pegel. In *OCEANS 2009-EUROPE*, pages 1–6, 2009. doi: 10.1109/OCEANSE.2009.5278313.
- Venkatesan, R., Tandon, A., D’Asaro, E., and Atmanand, M. A., editors. *Observing the Oceans in Real Time*. Springer Oceanography. Springer International Publishing, Cham, Switzerland, 2018. ISBN 978-3-319-66492-7 978-3-319-66493-4. doi: 10.1007/978-3-319-66493-4. URL: <http://link.springer.com/10.1007/978-3-319-66493-4>.

- Villari, M., Celesti, A., Fazio, M., and Puliafito, A. AllJoyn Lambda: An architecture for the management of smart environments in IoT. In *2014 International Conference on Smart Computing Workshops*, pages 9–14, 2014. doi: 10.1109/SMARTCOMP-W.2014.7046676.
- von Schuckmann, K., Le Traon, P.-Y., Alvarez-Fanjul, E., Axell, L., Balmaseda, M., Breivik, L.-A., Brewin, R. J. W., Bricaud, C., Drevillon, M., Drillet, Y., Dubois, C., Embury, O., Etienne, H., Sotillo, M. G., Garric, G., Gasparin, F., Gutknecht, E., Guinehut, S., Hernandez, F., Juza, M., Karlson, B., Korres, G., Legeais, J.-F., Levier, B., Lien, V. S., Morrow, R., Notarstefano, G., Parent, L., Pascual, Á., Pérez-Gómez, B., Perruche, C., Pinardi, N., Pisano, A., Poulain, P.-M., Pujol, I. M., Raj, R. P., Raudsepp, U., Roquet, H., Samuelson, A., Sathyendranath, S., She, J., Simoncelli, S., Solidoro, C., Tinker, J., Tintoré, J., Viktorsson, L., Ablain, M., Almroth-Rosell, E., Bonaduce, A., Clementi, E., Cossarini, G., Dagneaux, Q., Desportes, C., Dye, S., Fratianni, C., Good, S., Greiner, E., Gourrion, J., Hamon, M., Holt, J., Hyder, P., Kennedy, J., Manzano-Muñoz, F., Melet, A., Meyssignac, B., Mulet, S., Buongiorno Nardelli, B., O’Dea, E., Olason, E., Paulmier, A., Pérez-González, I., Reid, R., Racault, M.-F., Raitzos, D. E., Ramos, A., Sykes, P., Szekely, T., and Verbrugge, N. The Copernicus Marine Environment Monitoring Service Ocean State Report. *Journal of Operational Oceanography*, 9(2):235–320, 2016. ISSN 1755-876X, 1755-8778. doi: 10.1080/1755876X.2016.1273446. URL: <https://www.tandfonline.com/doi/full/10.1080/1755876X.2016.1273446>.
- Waldmann, C., Tamburri, M., Prien, R. D., and Fietzek, P. Assessment of sensor performance. *Ocean Sci.*, 6:11, 2010.
- Wiemann, S., Karrasch, P., and Bernard, L. Ad-hoc combination and analysis of heterogeneous and distributed spatial data for environmental monitoring – design and prototype of a web-based solution. *International Journal of Digital Earth*, pages 1–16, 2017. ISSN 1753-8947, 1753-8955. doi: 10.1080/17538947.2017.1326984. URL: <https://www.tandfonline.com/doi/full/10.1080/17538947.2017.1326984>.
- World Economic Forum. *The Global Risks Report 2016, 11th Edition*. World Economic Forum, Geneva, Switzerland, 11. edition, 2016. URL: http://www3.weforum.org/docs/GRR/WEF_GRR16.pdf.
- Zerr, B., Jaulin, L., Creuze, V., Debese, N., Quidu, I., Clement, B., and Billon-Coat, A., editors. *Quantitative Monitoring of the Underwater Environment*. vol. 6 of *Ocean Engineering & Oceanography*. Springer International Publishing, Cham, 2016. ISBN 978-3-319-32105-9 978-3-319-32107-3. doi: 10.1007/978-3-319-32107-3. URL: <http://link.springer.com/10.1007/978-3-319-32107-3>.

Zhuykov, S. Solid-state sensors monitoring parameters of water quality for the next generation of wireless sensor networks. *Sensors and Actuators B: Chemical*, 161(1): 1–20, 2012. ISSN 0925-4005. doi: 10.1016/j.snb.2011.10.078. URL: <http://www.sciencedirect.com/science/article/pii/S0925400511009968>.

Part IX.

Appendix

A. Appendix

A.1. Commercially Available Sensor Review

Table A.1.: Brief review of commercially available transmissometer (attenuometer) systems used in applied research or industrial applications.

Sensor	Manufacturer			Wavelengths in nm	Depth ratings in m	Dimensions in mm	Mass in kg
c-ROVER 2000	Sea-Bird Electronics, Inc., USA			450, 532, and 650	2000	783 x 101	4.1
C-Star	Sea-Bird Electronics, Inc., USA			370, 470, 530 or 650	600 or 6000	290 x 93	3.6
BAM	Sea-Bird Electronics, Inc., USA			650, 530 or 470	1000	124 x 63	2.1
ac-s	Sea-Bird Electronics, Inc., USA			400-730	500 or 5000	770 x 104	0.8
UVT-LED-SW UV	Sensorex, Inc., USA			254	10,20 or 30	238 x 76	0.8
Opus	TriOS Mess- und Datentechnik GmbH			200 - 360	30, 300	470 x 48	3
LISA UV	TriOS Mess- und Datentechnik GmbH			254, 520	30, 300	300 x 48	2.3
LISA color	TriOS Mess- und Datentechnik GmbH			380, 390, 410, 413, 436, 525, 620 or 740	30, 300	340 x 48	2.4
Viper	TriOS Mess- und Datentechnik GmbH			360 - 750	30, 300	495 x 48	2.4
Oscar	TriOS Mess- und Datentechnik GmbH			360 - 750	500	441 x 130	
NiCaVis IQ	705	Xylem Analytics Sales GmbH & Co. KG, WTW	Germany	200 - 390	10	802 x 59.9	4.0
NitraVis IQ	701	Xylem Analytics Sales GmbH & Co. KG, WTW	Germany	200-720	10	802 x 59.9	4.8
UV SAC	700 IQ	Xylem Analytics Sales GmbH & Co. KG, WTW	Germany	254, 550	10	802 x 59.9	4.8
CarboVis IQ	700	Xylem Analytics Sales GmbH & Co. KG, WTW	Germany	200-720	10	802 x 59.9	4.8
IQ SensorNet	YSI Inc. / Xylem Inc., USA			254		802 x 59.9	7.8

A.2. Circuit Schematics of the PCB Modules

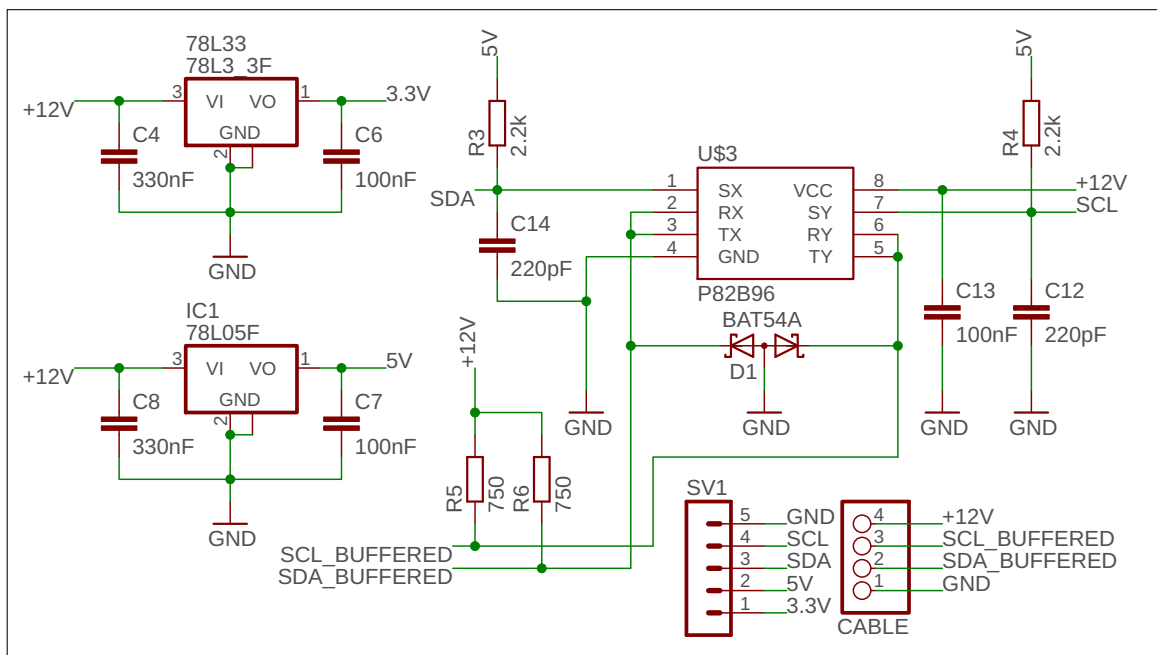


Figure A.1.: Circuit schematic of communication unit. This unit contains the voltage regulators for the sensor probe (3.3 V and 5 V) as well as the Inter-integrated circuit, serial computer bus (I²C) buffer for long distance communication. The sensor probe will be connected to the top side unit using a 4 wire cable allowing power supply and communication.

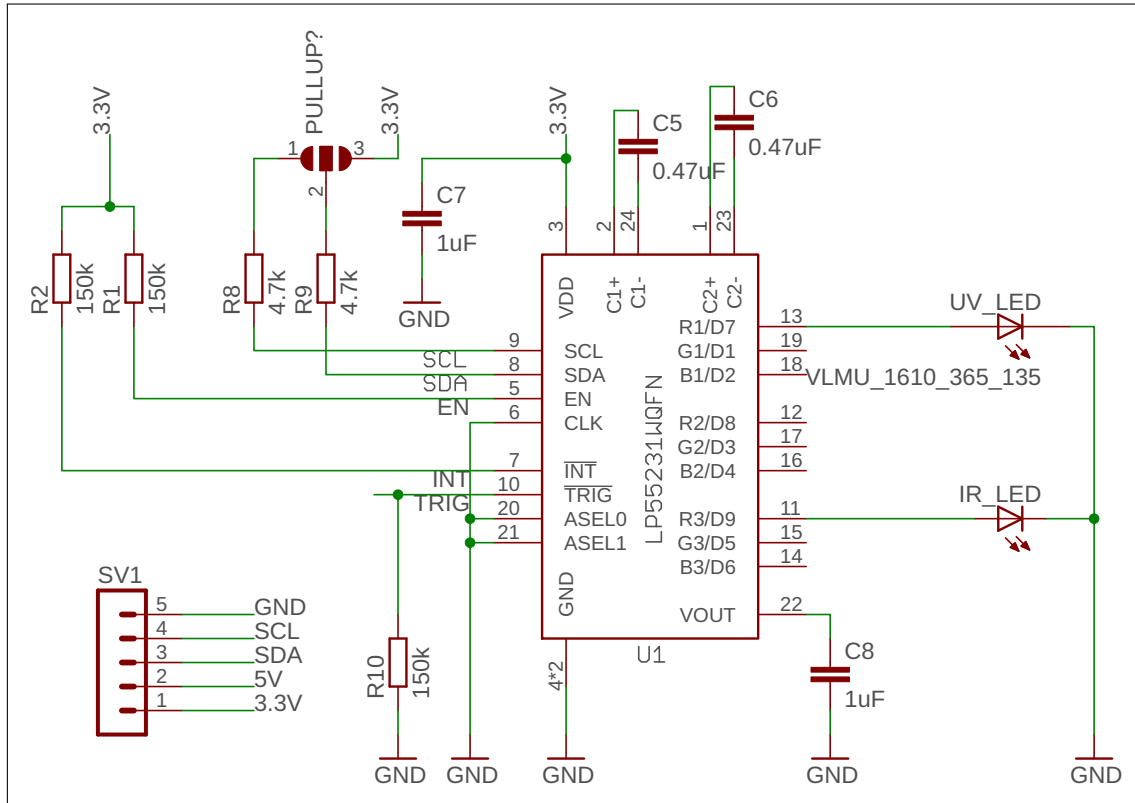


Figure A.2.: Circuit schematic of emitter unit. This units contains the Light emitting diode (LED) driver allowing the control and monitoring of the UV LED and IR LED.

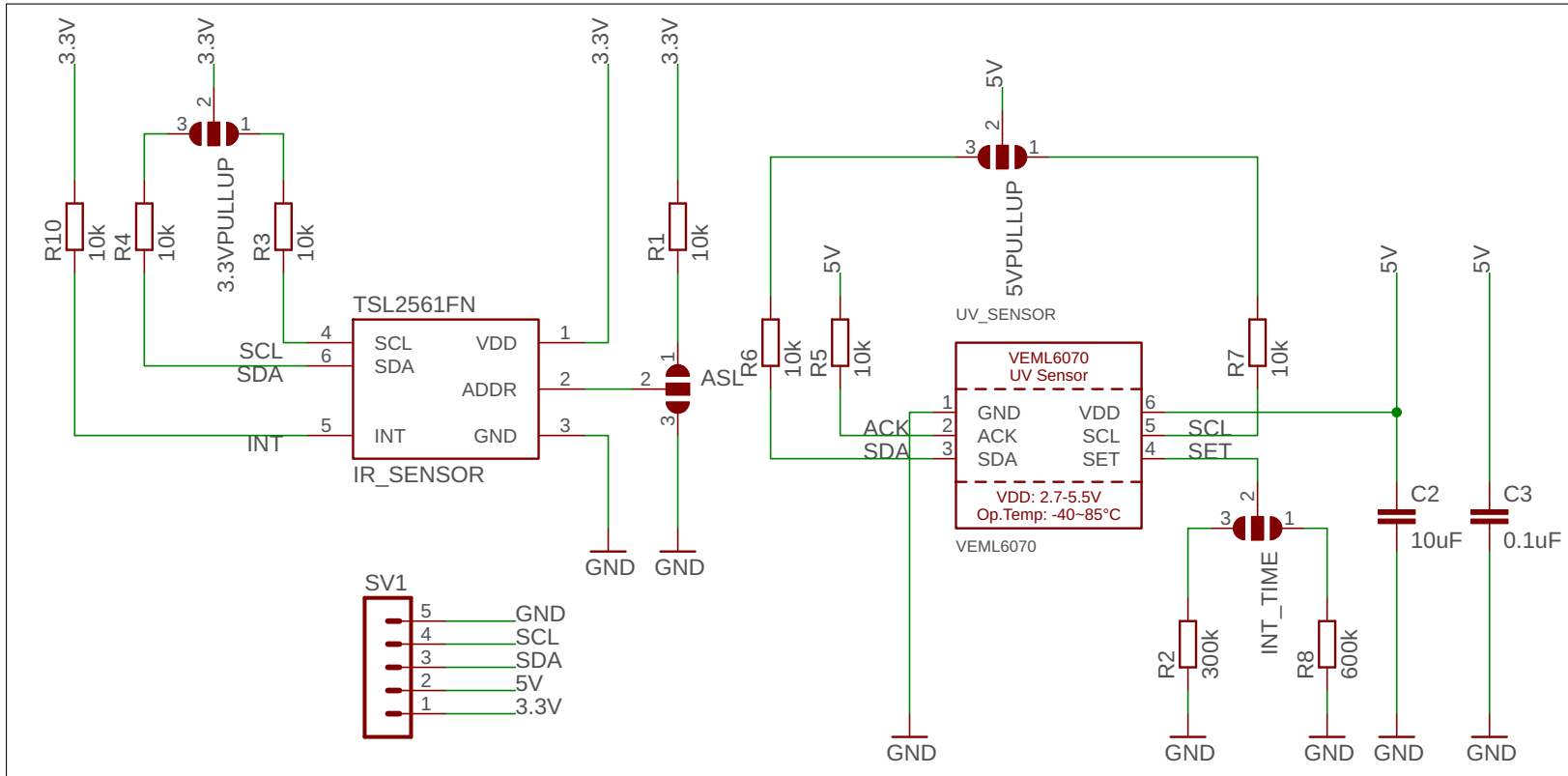


Figure A.3.: Circuit schematic of detector unit. This unit contains the UV and IR light-to-digital converters allowing the dynamic measurement of the transmitted light.

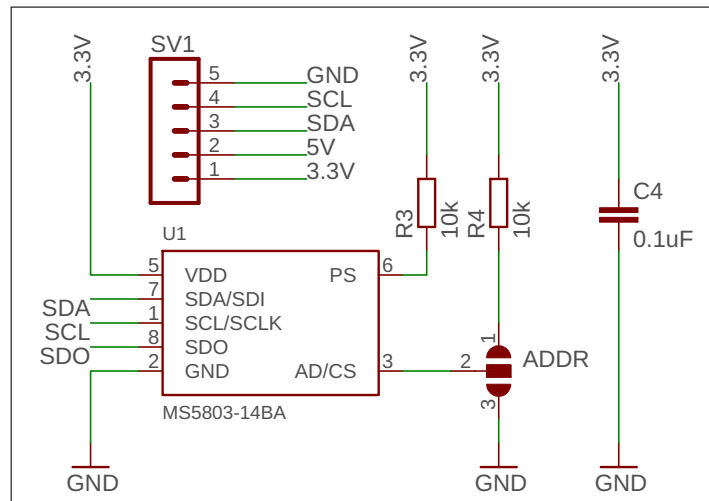


Figure A.4.: Circuit schematic of pressure unit. This unit contains the pressure and temperature sensor (water depth and water temperature).

A.3. Resin Characteristics

Table A.2.: Resin characteristics according to data sheet.

Liquid Properties	
Base material	Polyurethane
Density part A - resin	1.06 g l ⁻¹
Density part B - hardener	1.16 g l ⁻¹
Part A viscosity	900 mPa s at 23 °C
Part B viscosity	1200 mPa s at 23 °C
Mixed system viscosity	1050 mPa s at 23 °C
Mix ratio (mass)	0.92 : 1
Mix ratio (volume)	1 : 1
Usable life	~ 15 min at 20 °C
Gel time	~ 20 min at 23 °C
Cure time	24 h at 60 °C
Cure time	4 h
Colour part A - resin	Clear
Colour part B - hardener	Clear
Storage conditions	Dry Conditions: Above 15 °C Below 35 °C
Shelf life	12 months
Shrinkage	< 1 %

A.4. Cable Characteristics

Table A.3.: Cable LifYDY characteristics according to data sheet.

Ordering	
Manufacturer	Kabeltronik Arthur Volland GmbH, Germany
Cable type	Miniature control cables
Cable series	LifYDY
Order number	340401000
Construction	
Dimensions (cores)	$4 \times 0.1 \text{ mm}$
Outer cable diameter	4.0 mm
Linear mass density	0.025 kg m^{-1}
Linear copper mass density	0.0114 kg m^{-1}
Conductor	finest, bare stranded copper wire
Structure of conductor	$51 \times 0.05 \text{ mm}$
Core insulation	PVC according to VDE 0207
Color sequence	DIN 47100
Twisting	cores in layers
Shield	bare copper spiral shield
Jacket	S-PVC according to VDE 0207, black RAL 9005
Technical characteristics	
Insulation resistance	min. $200 \text{ M}\Omega \times \text{km}$ at 20°C
Operating voltage	300 V
Testing voltage	900 V
Linear resistance	$0.2 \Omega \text{ m}^{-1}$
Temperature range	static: -20°C to 70°C
	dynamic: -5°C to 70°C



Figure A.5.: LifYDY cable wire assignment.

A.5. Connector Characteristics

Table A.4.: Connector characteristics according to data sheet.

Ordering	
Manufacturer	CONEC Elektronische Bauelemente GmbH, Lippstadt, Germany
Connector type	Female connector M8 × 1
Connector series	SAL-8-RSC4-S
Order number	42-00012
Construction	
Dimension	∅14 mm × 0.1 mm
Contact	CuZn
Contact plating	Au over Ni in mating area
Contact carrier	PA6, UL 94
Cable sealing	NBR
O-Ring	Silicone / NBR
Coupling nut	CuZn, Ni
Housing	PA6 GF, UL 94
Technical characteristics	
Insulation resistance	min. 100 MΩ
Rated voltage	30 V
Current rating	4 A at 40 °C with 0.5 m ²
Degree of protection	IP 67, in mated condition
Temperature range	−30 °C to 85 °C

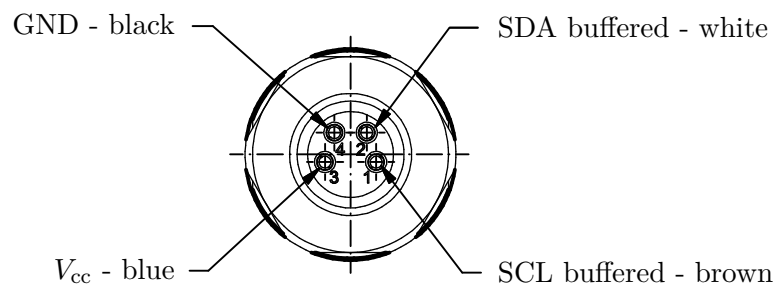


Figure A.6.: Schematic drawing of the connector pin out.

A.6. 3D Printer Raise 3D N2 Plus Specifications

Table A.5.: 3D Printer Raise 3D N2 Plus specification.

Printer Properties	
Print Technology	FFF
Build Volume (WxDxH)	305 mm × 305 mm × 610 mm
Layer Resolution	0.01 mm ~ 0.25 mm
Filament Type	PLA, PLA+, ABS, PC, PETG, R-flex, TPU, HIPS, Bronze-filled, Wood-filled
Printing Surface	Buildtak
Heated Build Platform	Yes
Enclosure	Yes
Nozzle Diameter	0.4 mm
Nozzle Working Temperature	170 °C ~ 300 °C
Number of Nozzles	2
Printing Speed	10 mm s ⁻¹ ~ 150 mm s ⁻¹
Moving Speed	150 mm s ⁻¹ ~ 300 mm s ⁻¹
Positioning Accuracy	XY-axes: 0.001 25 mm Z-axis: 0.001 25 mm

A.7. Software Development

Listing A.1: Firmware code (Arduino sketch) of the sensor system.

```

#include <I2C.h> //Copyright (c) 2011–2012 Wayne Truchsess 1
#include <EEPROM.h> 2
#include <SPI.h> 3
#include <SdFat.h> //Copyright (c) 20011–2017 Bill Greiman 4
#include <ArduinoJson.h> //Copyright Benoit Blanchon 2014–2017 5
#include <TimeLib.h> //Copyright (c) Michael Margolis 2009–2014 6
#include <TinyGPS++.h> //Copyright (C) 2008–2013 Mikal Hart 7
TinyGPSPlus gps; 8
9
#define VEML6070_READ_ADDRESS 0x39 10
#define VEML6070_WRITE_ADDRESS 0x38 11
12
#define TSL2561_ADDRESS 0x29 13
#define TSL2561_REG_CONTROL 0x00 14

```

<code>#define TSL2561_REG_TIME_GAIN</code>	<code>0x01</code>		15
<code>#define TSL2561_CHO_DATA_LOW</code>	<code>0x0C</code>		16
<code>#define TSL2561_CHO_DATA_HIGH</code>	<code>0x0D</code>		17
<code>#define TSL2561_CH1_DATA_LOW</code>	<code>0x0E</code>		18
<code>#define TSL2561_CH1_DATA_HIGH</code>	<code>0x0F</code>		19
<code>#define TSL2561_REG_ID</code>	<code>0x0A</code>		20
			21
<code>#define TSL2561_COMMAND_BIT</code>	<code>0x80</code>		22
<code>#define TSL2561_WORD_BIT</code>	<code>0x20</code>		23
			24
<code>#define TSL2561_START_CONDITION</code>	<code>0x03</code>		25
<code>#define TSL2561_SLEEP_CONDITION</code>	<code>0x00</code>		26
			27
<code>#define TSL2561_GAIN_1X</code>	<code>0x00</code>	<code>// No gain</code>	28
<code>#define TSL2561_GAIN_16X</code>	<code>0x10</code>	<code>// 16x gain</code>	29
<code>#define TSL2561_INTEGRATIONTIME_13MS</code>	<code>0x00</code>	<code>// 13.7ms</code>	30
<code>#define TSL2561_INTEGRATIONTIME_101MS</code>	<code>0x01</code>	<code>// 101ms</code>	31
<code>#define TSL2561_INTEGRATIONTIME_402MS</code>	<code>0x02</code>	<code>// 402ms</code>	32
			33
<code>#define LP55231_ADDRESS</code>	<code>0x32</code>		34
<code>#define LP55231_REG_RESET</code>	<code>0x3D</code>		35
<code>#define LP55231_REG_ENABLE</code>	<code>0x00</code>		36
<code>#define LP55231_REG_MISC</code>	<code>0x36</code>		37
<code>#define LP55231_CMD_MISC</code>	<code>0x53</code>		38
			39
<code>#define LP55231_REG_TEMP_CTRL</code>	<code>0x3E</code>		40
<code>#define LP55231_CMD_TEMP_READ</code>	<code>0x04</code>		41
<code>#define LP55231_REG_TEMP_READ</code>	<code>0x3F</code>		42
			43
<code>#define LP55231_REG_D7_UV_CTRL</code>	<code>0x0C</code>		44
<code>#define LP55231_REG_D9_IR_CTRL</code>	<code>0x0E</code>		45
			46
<code>#define LP55231_REG_D7_UV_PWM</code>	<code>0x1C</code>		47
<code>#define LP55231_REG_D9_IR_PWM</code>	<code>0x1E</code>		48
			49
<code>#define LP55231_REG_D7_UV_I_CTRL</code>	<code>0x2C</code>		50
<code>#define LP55231_REG_D9_IR_I_CTRL</code>	<code>0x2E</code>		51
			52
<code>#define LP55231_CMD_LOG_EN_TRUE</code>	<code>0x20</code>		53
			54
<code>#define LP55231_REG_TEST_CTRL</code>	<code>0x41</code>		55
<code>#define LP55231_CMD_TEST_D7_UV</code>	<code>0x86</code>		56
<code>#define LP55231_CMD_TEST_D9_IR</code>	<code>0x88</code>		57
<code>#define LP55231_CMD_TEST_VDD</code>	<code>0x90</code>		58
<code>#define LP55231_CMD_TEST_VOUT</code>	<code>0x8F</code>		59

```

#define LP55231_REG_TEST_READ          0x42          60
                                                    61
#define LP55231_CMD_RESET              0xFF          62
#define LP55231_CMD_ENABLE            0x40          63
                                                    64
#define MS5803_ADDRESS                 0x77          65
                                                    66
#define MS5803_PRESSURE                0x00          67
#define MS5803_TEMPERATURE             0x10          68
                                                    69
#define MS5803_CMD_RESET               0x1E // reset command 70
#define MS5803_CMD_ADC_READ           0x00 // ADC read command 71
#define MS5803_CMD_ADC_CONV           0x40 // ADC conversion command 72
#define MS5803_CMD_PROM                0xA0 // Coefficient location 73
#define MS5803_ADC_256                 0x00          74
#define MS5803_ADC_512                 0x02          75
#define MS5803_ADC_1024                0x04          76
#define MS5803_ADC_2048                0x06          77
#define MS5803_ADC_4096                0x08          78
                                                    79
// Some constants used in calculations below 80
const uint64_t POW_2_33 = 8589934592ULL; // 2^33 = 8589934592 81
const uint64_t POW_2_37 = 137438953472ULL; // 2^37 = 137438953472 82
uint32_t MS5803_RAW_Temperature; 83
uint32_t MS5803_RAW_Pressure; 84
uint32_t MS5803_Temperature; 85
uint32_t MS5803_Pressure; 86
static int32_t dT; 87
static int32_t TEMP; 88
static int64_t Offset; 89
static int64_t Sensitivity; 90
static int64_t T2; 91
static int64_t OFF2; 92
static int64_t Sens2; 93
byte HighByte; 94
byte MidByte; 95
byte LowByte; 96
                                                    97
long max_IR = 0; 98
long max_UV = 0; 99
                                                    100
void setup() { 101
    // put your setup code here, to run once: 102
    Serial.begin(9600); 103
    Serial1.begin(9600); 104

```



```

Serial2.begin(9600);      105
Serial3.begin(9600);      106
pinMode(5, OUTPUT);      107
I2c.begin();              108
I2c.setSpeed(0);          109 //Speed is either 0 or 1 with 0 = 100kHz and
    1 = 400kHz
I2c.setTimeout(500);      110 //Set value for i2c connection timeout in ms
LP55231_reset();          111
LP55231_enable();         112
MS5803_reset();           113
MS5803_get_constants();   114
}                            115
void loop() {              116
    updateGPS();           117
    if (gps.location.isValid() == 0) 118
    {                       119
        Serial.print("No_GPS_Signal\n"); 120
        Serial2.print("No_GPS_Signal\n"); 121
        ackn(1, 25);        122 //if there is no GPS, the LED of the switch
            on/off will indicate it 123
    }                       124
    else                   125
    {                       126
        if (               127
            second() == 00 || 128
            second() == 30 129
        ) {                 130
            //createJSON(int I_IR, int I_UV, int PWM_IR, int PWM_UV, int 131
                LOG_EN_IR, int LOG_EN_UV, int GAIN_IR, int ITIME_IR, int
                ITIME_UV) {
            createJSON(255, 255, 255, 255, 0, 0, 0, 1, 2); 132
            ackn(2, 50);     133 //when a measurement is done, the LED will
                indicate it by flashing 2x
        }                   134
    }                       135
}                            136
}                            137
void updateGPS() {         138
    while (Serial1.available()) { // check for gps data 139
        int c = Serial1.read(); 140
        if (gps.encode(c)) { // encode gps data 141
            gps.encode(Serial1.read()); 142
        }                   143
    }                       144
}

```

```

    if (gps.location.isUpdated()) 145
    { 146
        setTime(gps.time.hour(), gps.time.minute(), gps.time.second(), 147
            gps.date.day(), gps.date.month(), gps.date.year());
    } 148
} 149
150
151
String timeStamp() { 152
    char timeStamp[32]; 153
    sprintf(timeStamp, "%02d-%02d-%02dT%02d:%02d:%02d_", 154
        year(), month(), day(), hour(), minute(), second()); 155
    return timeStamp; 156
} 157
158
void ackn(int amount, int waitTime) { 159
    for (int i = 0; i < amount; i++) { 160
        digitalWrite(5, HIGH); 161
        delay(waitTime); 162
        digitalWrite(5, LOW); 163
        delay(waitTime); 164
    } 165
} 166
void createJSON(int I_IR, int I_UV, int PWM_IR, int PWM_UV, int 167
    LOG_EN_IR, int LOG_EN_UV, int GAIN_IR, int ITIME_IR, int
    ITIME_UV) {
    StaticJsonBuffer<400> jsonBuffer; 168
    JsonObject& root = jsonBuffer.createObject(); 169
    //LP55231 LED DRIVER 170
    //IR LED 171
    LP55231_IR_SET_CURRENT(I_IR); 172
    LP55231_IR_PWM(PWM_IR); 173
    LP55231_IR_SET_LOG_EN(LOG_EN_IR); 174
    //UV LED 175
    LP55231_UV_SET_CURRENT(I_UV); 176
    LP55231_UV_PWM(PWM_UV); 177
    LP55231_UV_SET_LOG_EN(LOG_EN_UV); 178
    //WAIT FOR EQUILIBRIUM – DELAY 179
    delay(250); 180
    //IR CHANNEL 181
    TSL2561_ENABLE(); 182
    TSL2561_SET_CONV(GAIN_IR, ITIME_IR); 183
    root["id"] = "boat001"; 184
    root["timeStamp"] = timeStamp(); 185
    root["latitude"] = String(gps.location.lat(), 6); 186

```



```

void LP55231_reset() {
    I2C_WRITE(LP55231_ADDRESS, LP55231_REG_RESET, LP55231_CMD_RESET,
        10);
    wait4sensor(10);
}

void LP55231_enable() {
    I2C_WRITE(LP55231_ADDRESS, LP55231_REG_ENABLE, LP55231_CMD_ENABLE
        , 10);
}

void LP55231_IR_PWM(int brightness) {
    I2C_WRITE(LP55231_ADDRESS, LP55231_REG_MISC, LP55231_CMD_MISC,
        10);
    I2C_WRITE(LP55231_ADDRESS, LP55231_REG_D9_IR_PWM, brightness , 10)
        ;
}

void LP55231_IR_OFF() {
    I2C_WRITE(LP55231_ADDRESS, LP55231_REG_MISC, LP55231_CMD_MISC,
        10);
    I2C_WRITE(LP55231_ADDRESS, LP55231_REG_D9_IR_PWM, 0x00 , 10);
}

void LP55231_UV_PWM(int brightness) {
    I2C_WRITE(LP55231_ADDRESS, LP55231_REG_MISC, LP55231_CMD_MISC,
        10);
    I2C_WRITE(LP55231_ADDRESS, LP55231_REG_D7_UV_PWM, brightness , 10)
        ;
}

void LP55231_UV_OFF() {
    I2C_WRITE(LP55231_ADDRESS, LP55231_REG_MISC, LP55231_CMD_MISC,
        10);
    I2C_WRITE(LP55231_ADDRESS, LP55231_REG_D7_UV_PWM, 0x00 , 10);
}

void LP55231_IR_SET_CURRENT(int current) {
    I2C_WRITE(LP55231_ADDRESS, LP55231_REG_D9_IR_I_CTRL, current , 10)
        ;
}

void LP55231_UV_SET_CURRENT(int current) {
    I2C_WRITE(LP55231_ADDRESS, LP55231_REG_D7_UV_I_CTRL, current , 10)
        ;
}

```

```
} 267
268
void LP55231_IR_SET_LOG_EN(int LOG_EN) { 269
    switch (LOG_EN) { 270
        case 1: 271
            I2C_WRITE(LP55231_ADDRESS, LP55231_REG_D9_IR_CTRL, 272
                LP55231_CMD_LOG_EN_TRUE, 10);
            break; 273
        case 0: 274
            I2C_WRITE(LP55231_ADDRESS, LP55231_REG_D9_IR_CTRL, 0x00, 10); 275
            break; 276
    } 277
} 278
279
void LP55231_UV_SET_LOG_EN(int LOG_EN) { 280
    switch (LOG_EN) { 281
        case 1: 282
            I2C_WRITE(LP55231_ADDRESS, LP55231_REG_D7_UV_CTRL, 283
                LP55231_CMD_LOG_EN_TRUE, 10);
            break; 284
        case 0: 285
            I2C_WRITE(LP55231_ADDRESS, LP55231_REG_D7_UV_CTRL, 0x00, 10); 286
            break; 287
    } 288
} 289
290
int8_t LP55231_GET_TEMPERATURE() { 291
    I2C_WRITE(LP55231_ADDRESS, LP55231_REG_TEMP_CTRL, 292
        LP55231_CMD_TEMP_READ, 25);
    return I2C_READ8(LP55231_ADDRESS, LP55231_REG_TEMP_READ, 10); 293
} 294
295
long LP55231_IR_READ_CURRENT() { 296
    return I2C_READ8(LP55231_ADDRESS, LP55231_REG_D9_IR_I_CTRL, 10); 297
} 298
299
long LP55231_UV_READ_CURRENT() { 300
    return I2C_READ8(LP55231_ADDRESS, LP55231_REG_D7_UV_I_CTRL, 10); 301
} 302
303
long LP55231_IR_READ_VOLTAGE() { 304
    I2C_WRITE(LP55231_ADDRESS, LP55231_REG_TEST_CTRL, 305
        LP55231_CMD_TEST_D9_IR, 3);
    return (I2C_READ8(LP55231_ADDRESS, LP55231_REG_TEST_READ, 1)); 306
} 307
```

```

long LP55231_UV_READ_VOLTAGE() {
    I2C_WRITE(LP55231_ADDRESS, LP55231_REG_TEST_CTRL,
              LP55231_CMD_TEST_D7_UV, 3);
    return (I2C_READ8(LP55231_ADDRESS, LP55231_REG_TEST_READ, 1));
}

long LP55231_VDD_READ_VOLTAGE() {
    I2C_WRITE(LP55231_ADDRESS, LP55231_REG_TEST_CTRL,
              LP55231_CMD_TEST_VDD, 3);
    return (I2C_READ8(LP55231_ADDRESS, LP55231_REG_TEST_READ, 1));
}

long LP55231_VOUT_READ_VOLTAGE() {
    I2C_WRITE(LP55231_ADDRESS, LP55231_REG_TEST_CTRL,
              LP55231_CMD_TEST_VOUT, 3);
    return (I2C_READ8(LP55231_ADDRESS, LP55231_REG_TEST_READ, 1));
}

float VEML6070_Read_VALUE(int itime) {
    int ms = 450;
    switch (itime) {
        case 0:
            ms = ms / 2;
            I2C_WRITE_VEML(VEML6070_WRITE_ADDRESS, (itime << 2) | 0x02,
                           ms);
            break;
        case 1:
            ms = ms;
            I2C_WRITE_VEML(VEML6070_WRITE_ADDRESS, (itime << 2) | 0x02,
                           ms);
            break;
        case 2:
            ms = ms * 2;
            I2C_WRITE_VEML(VEML6070_WRITE_ADDRESS, (itime << 2) | 0x02,
                           ms);
            break;
        case 3:
            ms = ms * 4;
            I2C_WRITE_VEML(VEML6070_WRITE_ADDRESS, (itime << 2) | 0x02,
                           ms);
            break;
        default:
            break;
    }
}

```

```

    return I2C_READ_VEML();
}

uint8_t TSL2561_READ_REGISTER_ID() {
    return I2C_READ8(TSL2561_ADDRESS, TSL2561_REG_ID, 10);
}

void TSL2561_SET_CONV(int gain, int itime) {
    char command = 0x00;
    int ms;
    switch (gain) {
        case 0:
            command |= TSL2561_GAIN_1X;
            break;
        case 1:
            command |= TSL2561_GAIN_16X;
            break;
        default:
            command |= TSL2561_GAIN_1X;
            break;
    }
    switch (itime) {
        case 0:
            ms = 14;
            command |= TSL2561_INTEGRATIONTIME_13MS;
            break;
        case 1:
            ms = 102;
            command |= TSL2561_INTEGRATIONTIME_101MS;
            break;
        case 2:
            ms = 403;
            command |= TSL2561_INTEGRATIONTIME_402MS;
            break;
        default:
            command |= 0x00;
            break;
    }
    I2C_WRITE(TSL2561_ADDRESS, TSL2561_COMMAND_BIT |
              TSL2561_REG_TIME_GAIN, command, ms);
}

uint16_t TSL2561_READ_VALUE(int channel) {
    char DataLow;
    char DataHigh;

```

```

uint8_t CHDataLow; 390
uint8_t CHDataHigh; 391
switch (channel) { 392
    case 0: 393
        DataLow = TSL2561_CHO_DATA_LOW; 394
        DataHigh = TSL2561_CHO_DATA_HIGH; 395
        break; 396
    case 1: 397
        DataLow = TSL2561_CH1_DATA_LOW; 398
        DataHigh = TSL2561_CH1_DATA_HIGH; 399
        break; 400
    default: 401
        break; 402
} 403
CHDataLow = I2C_READ8(TSL2561_ADDRESS, TSL2561_COMMAND_BIT | 404
    DataLow, 1);
CHDataHigh = I2C_READ8(TSL2561_ADDRESS, TSL2561_COMMAND_BIT | 405
    DataHigh, 1);
uint16_t result = 256 * CHDataHigh + CHDataLow; 406
return result; 407
} 408
409
void TSL2561_ENABLE() { 410
    I2C_WRITE(TSL2561_ADDRESS, TSL2561_COMMAND_BIT | 411
        TSL2561_REG_CONTROL, TSL2561_START_CONDITION, 50);
} 412
413
void TSL2561_DISABLE() { 414
    I2C_WRITE(TSL2561_ADDRESS, TSL2561_COMMAND_BIT | 415
        TSL2561_REG_CONTROL, TSL2561_SLEEP_CONDITION, 10);
} 416
417
void MS5803_reset() { 418
    I2c.write(MS5803_ADDRESS, MS5803_CMD_RESET); 419
    wait4sensor(10); 420
} 421
422
void MS5803_get_constants() { 423
    int z = 0; 424
    for (int i = 0; i < 8; i++) { 425
        I2c.read(MS5803_ADDRESS, MS5803_CMD_PROM + (i * 2), 2); 426
        HighByte = I2c.receive(); 427
        EEPROM.write(z, HighByte); 428
        LowByte = I2c.receive(); 429
        z++; 430
    }
}

```



```

EEPROM.write(z, LowByte);           431
z++;                                 432
//sensorCoeffs[i] = ((HighByte << 8) + LowByte); 433
//Serial.println(sensorCoeffs[i]);  434
}                                     435
}                                     436
}                                     437
unsigned int MS5803_use_constants(int value) { 438
    HighByte = EEPROM.read(value * 2); 439
    LowByte = EEPROM.read(value * 2 + 1); 440
    return ((HighByte << 8) + LowByte); 441
}                                     442
                                     443
void MS5803_get_values(int accuracy) { 444
    switch ( accuracy ) 445
    { 446
        case 0 : //MS5803_ADC_256 447
            MS5803_RAW_Temperature = MS5803_get_raw_values( 448
                MS5803_CMD_ADC_CONV + MS5803_TEMPERATURE + MS5803_ADC_256,
                1);
            MS5803_RAW_Pressure = MS5803_get_raw_values( 449
                MS5803_CMD_ADC_CONV + MS5803_PRESSURE + MS5803_ADC_256,
                1);
            break; 450
        case 1 : //MS5803_ADC_512 451
            MS5803_RAW_Temperature = MS5803_get_raw_values( 452
                MS5803_CMD_ADC_CONV + MS5803_TEMPERATURE + MS5803_ADC_512,
                3);
            MS5803_RAW_Pressure = MS5803_get_raw_values( 453
                MS5803_CMD_ADC_CONV + MS5803_PRESSURE + MS5803_ADC_512, 3)
            ;
            break; 454
        case 2 : //MS5803_ADC_1024 455
            MS5803_RAW_Temperature = MS5803_get_raw_values( 456
                MS5803_CMD_ADC_CONV + MS5803_TEMPERATURE + MS5803_ADC_1024
                , 4);
            MS5803_RAW_Pressure = MS5803_get_raw_values( 457
                MS5803_CMD_ADC_CONV + MS5803_PRESSURE + MS5803_ADC_1024,
                4);
            break; 458
        case 3 : //MS5803_ADC_2048 459
            MS5803_RAW_Temperature = MS5803_get_raw_values( 460
                MS5803_CMD_ADC_CONV + MS5803_TEMPERATURE + MS5803_ADC_2048
                , 6);

```

```

MS5803_RAW_Pressure = MS5803_get_raw_values(
    MS5803_CMD_ADC_CONV + MS5803_PRESSURE + MS5803_ADC_2048,
    6);
break;
case 4 : //MS5803_ADC_4096
MS5803_RAW_Temperature = MS5803_get_raw_values(
    MS5803_CMD_ADC_CONV + MS5803_TEMPERATURE + MS5803_ADC_4096
    , 10);
MS5803_RAW_Pressure = MS5803_get_raw_values(
    MS5803_CMD_ADC_CONV + MS5803_PRESSURE + MS5803_ADC_4096,
    10);
break;
}
dT = (uint32_t)MS5803_RAW_Temperature - ((uint32_t)
    MS5803_use_constants(5) * 256);
TEMP = 2000 + ((int64_t)dT * MS5803_use_constants(6) >> 23);
TEMP = (uint32_t)TEMP;
if (TEMP < 2000) {
    T2 = 3 * ((int64_t)dT * dT) >> 33;
    T2 = (int32_t)T2;
    OFF2 = 3 * ((TEMP - 2000) * (TEMP - 2000)) / 2 ;
    Sens2 = 5 * ((TEMP - 2000) * (TEMP - 2000)) / 8 ;
    if (TEMP < -1500) {
        OFF2 = OFF2 + 7 * ((TEMP + 1500) * (TEMP + 1500));
        Sens2 = Sens2 + 4 * ((TEMP + 1500) * (TEMP + 1500));
    }
} else { // if TEMP is > 2000 (20.0C)
    T2 = 7 * ((int64_t)dT * dT) / pow(2, 37);
    T2 = (int32_t)T2;
    OFF2 = ((TEMP - 2000) * (TEMP - 2000)) / 16;
    Sens2 = 0;
}

Offset = ((int64_t)MS5803_use_constants(2) << 16) + ((
    MS5803_use_constants(4) * (int64_t)dT >> 7);
Sensitivity = ((int64_t)MS5803_use_constants(1) << 15) + ((
    MS5803_use_constants(3) * (int64_t)dT >> 8);
TEMP = TEMP - T2;
MS5803_Temperature = TEMP;
Offset = Offset - OFF2;
Sensitivity = Sensitivity - Sens2;
MS5803_Pressure = ((MS5803_RAW_Pressure * Sensitivity) / 2097152
    - Offset) / 32768;
}

```

```

unsigned long MS5803_get_raw_values(char MS5803_CMD, int ms) { 496
    I2c.write(MS5803_ADDRESS, MS5803_CMD); 497
    wait4sensor(ms); 498
    I2c.read(MS5803_ADDRESS, MS5803_CMD_ADC_READ, 3); 499
    //wait4sensor(10); 500
    while (I2c.available()) { 501
        HighByte = I2c.receive(); 502
        MidByte = I2c.receive(); 503
        LowByte = I2c.receive(); 504
    } 505
    long result = ((long)HighByte << 16) + ((long)MidByte << 8) + ( 506
        long)LowByte;
    return result; 507
} 508
509
void I2C_WRITE_VEML(char address, char val, int ms) { 510
    I2c.write(VEML6070_WRITE_ADDRESS, val); 511
    wait4sensor(ms); 512
} 513
514
void I2C_WRITE(char address, char reg, char val, int ms) { 515
    I2c.write(address, reg, val); 516
    wait4sensor(ms); 517
} 518
519
uint16_t I2C_READ_VEML() { 520
    I2c.read(VEML6070_READ_ADDRESS, 2); 521
    uint16_t result = I2c.receive(); 522
    result <<= 8; 523
    I2c.read(VEML6070_WRITE_ADDRESS, 2); 524
    result |= I2c.receive(); 525
    return result; 526
} 527
528
long I2C_READ8(char address, char reg, int ms) { 529
    I2c.read(address, reg, 1); 530
    wait4sensor(ms); 531
    while (I2c.available()) { 532
        LowByte = I2c.receive(); 533
    } 534
    long result = (long)LowByte; 535
    return result; 536
} 537
538
long I2C_READ16(char address, char reg) { 539

```

```
I2c.read(address, reg, 2); 540
wait4sensor(10); 541
while (I2c.available()) { 542
    HighByte = I2c.receive(); 543
    LowByte = I2c.receive(); 544
} 545
long result = ((long)HighByte << 8) + (long)LowByte; 546
return result; 547
} 548
549
long I2C_READ24(char address, char reg) { 550
    I2c.read(address, reg, 3); 551
    wait4sensor(10); 552
    while (I2c.available()) { 553
        HighByte = I2c.receive(); 554
        MidByte = I2c.receive(); 555
        LowByte = I2c.receive(); 556
    } 557
    long result = ((long)HighByte << 16) + ((long)MidByte << 8) + ( 558
        long)LowByte;
    return result; 559
} 560
561
void wait4sensor(int ms) { 562
    delay(ms); 563
} 564
565
long average (long * array, long len) // assuming array is int. 566
{ 567
    long sum = 0L ; // sum will be larger than an item, long for 568
        safety.
    for (int i = 0 ; i < len ; i++) 569
        sum += array [i] ; 570
    return ((long) sum) / len ; // average will be fractional, so 571
        float may be appropriate.
} 572
```

A.8. Multimeter Specifications

Accuracy in \pm (% of reading + display error in counts (= number of smallest digits)). The accuracy is valid at a temperature of $+23\text{ }^\circ\text{C}$ ($\pm 5\text{ }^\circ\text{C}$), at a relative humidity of less than 75 %, non-condensing. Temperature coefficient: $+0.1 \cdot (\text{specified accuracy})/23\text{ }^\circ\text{C}$

Table A.6.: Voltcraft VC 830 multimeter specifications

Measurement	Range	Resolution	Accuracy
DCV	600 mV	0.1 mV	$\pm(0.5\% + 3)$
	6 V/60 V	1 mV/10 mV	$\pm(0.5\% + 2)$
DCA	600 μA /6 mA/60 mA	0.1 μA /1 μA /10 μA	$\pm(0.8\% + 3)$
Ω	600 Ω	0.1 Ω	$\pm(0.8\% + 3)$
	6 k Ω /60 k Ω /600 k Ω	1 Ω /10 Ω /100 Ω	$\pm(0.8\% + 2)$
	6 M Ω	1 k Ω	$\pm(1.2\% + 2)$

A.9. Photometer Specification

Table A.7.: Hach Lange Cadas 200 photometer specifications

Wavelength range	190 nm – 1100 nm
Lightsources	Deuterium lamp: 190 nm – 340 nm Halogen lamp: 340 nm – 1100 nm
Monochromator	Flat grid with 1200 lines/mm
Wavelength accuracy	± 1 nm (holmium oxide filter at 361 nm)
Wavelength repeatability	< 0.01 nm
Scanning velocity	20 nm s ⁻¹
Photometric accuracy	0.2 % at $E_\lambda = 1$ (NBS filter 1-1140)
Photometric repeatability	0.001 E_λ at $E_\lambda = 1$
Zero stability scattered light	$\frac{0.001 E_\lambda}{12h}$, $< 0.1\%$ (10 g l ⁻¹ KJ solution at 200 nm)
Linearity range	$\pm 3 E_\lambda$
Spectral bandwidth	2 nm, 5 nm
Dimensions	46 cm \times 19.5 cm \times 41.5 cm
Weight	21 kg

A.10. Spectrometer Specification

Table A.8.: USB2000+ UV-VIS spectrometer specifications

UV-VIS Spectrometer Properties	
Dimensions	89.1 mm × 63.3 mm × 34.4 mm
Weight	190 g
Detector	Sony ILX511B (2048-element linear silicon CCD array)
Wavelength range	200 nm – 850 nm
Integration time	1 ms – 65 s (20 s typical)
Dynamic range	8.5×10^7 (system); 13001 for a single acquisition
Signal-to-noise ratio	2501 (full signal)
Dark noise	50 RMS counts
Grating	600 lines/mm, set to 200 nm – 850 nm (blazed at 300 nm)
Slit	25 μ m
Detector collection lens	No
Order-sorting	OFLV-200-850
Optical resolution	1.5 nm FWHM
Stray light	< 0.05 % at 600 nm; < 0.10 % at 435 nm
Fiber optic connector	SMA 905 to 0.22 numerical aperture single-strand fiber

Table A.9.: USB2000+ VIS-NIR spectrometer specifications

VIS-NIR Spectrometer Properties	
Dimensions	89.1 mm × 63.3 mm × 34.4 mm
Weight	190 g
Detector	Sony ILX511B (2048-element linear silicon CCD array)
Wavelength range	350 nm – 1000 nm
Integration time	1 ms – 65 s (20 s typical)
Dynamic range	8.5×10^7 (system); 13001 for a single acquisition
Signal-to-noise ratio	2501 (full signal)
Dark noise	50 RMS counts
Grating	600 lines/mm, set to 350 nm – 1000 nm (blazed at 500 nm)
Slit	25 μ m
Detector collection lens	No
Order-sorting	OFLV-350-1000
Optical resolution	1.5 nm FWHM
Stray light	< 0.05 % at 600 nm; < 0.10 % at 435 nm
Fiber optic connector	SMA 905 to 0.22 numerical aperture single-strand fiber

Declaration

I hereby declare under oath that I have completed the work submitted here independently and have composed it without outside assistance. Furthermore, I have not used anything other than the resources and sources stated and where I have taken sections from these works in terms of content or text, I have identified this appropriately.

Rostock, November 14, 2018

Robert Schima

Scientific Curriculum Vitae

Robert Schima, born on 25.02.1988 in Dessau

Scientific career

since 11/2018	Department Monitoring and Exploration Technologies, UFZ - Helmholtz Centre for Environmental Research Leipzig, guest scientist
since 10/2016	University of Rostock, Chair of Ocean Engineering, research associate
08/2016 - 10/2016	University of California, Berkeley, USA, Visiting Scientist
01/2015 - 10/2016	Department Monitoring and Exploration Technologies, UFZ - Helmholtz Centre for Environmental Research Leipzig, research associate
10/2011 - 03/2012	Department Monitoring and Exploration Technologies, UFZ - Helmholtz Centre for Environmental Research Leipzig, development engineer

Studies

04/2012 - 12/2014	University of Rostock, Master of Science, Environmental Engineering
Thesis 12/2014	<i>Comparative analysis of two different imaging techniques for the determination of crop growth and plant population</i>
08/2013 - 12/2013	Luleå University of Technology, Sweden, Environmental Engineering, semester abroad (Erasmus)
09/2008 - 09/2011	HTWK Leipzig, Bachelor of Engineering Energy and Environmental Technology
Thesis 09/2011	<i>Development of a monitoring system for emission monitoring of volatile organic compounds during near-natural groundwater remediation</i>

School education

2007	Abitur, Grammar School Philanthropinum Dessau
------	---